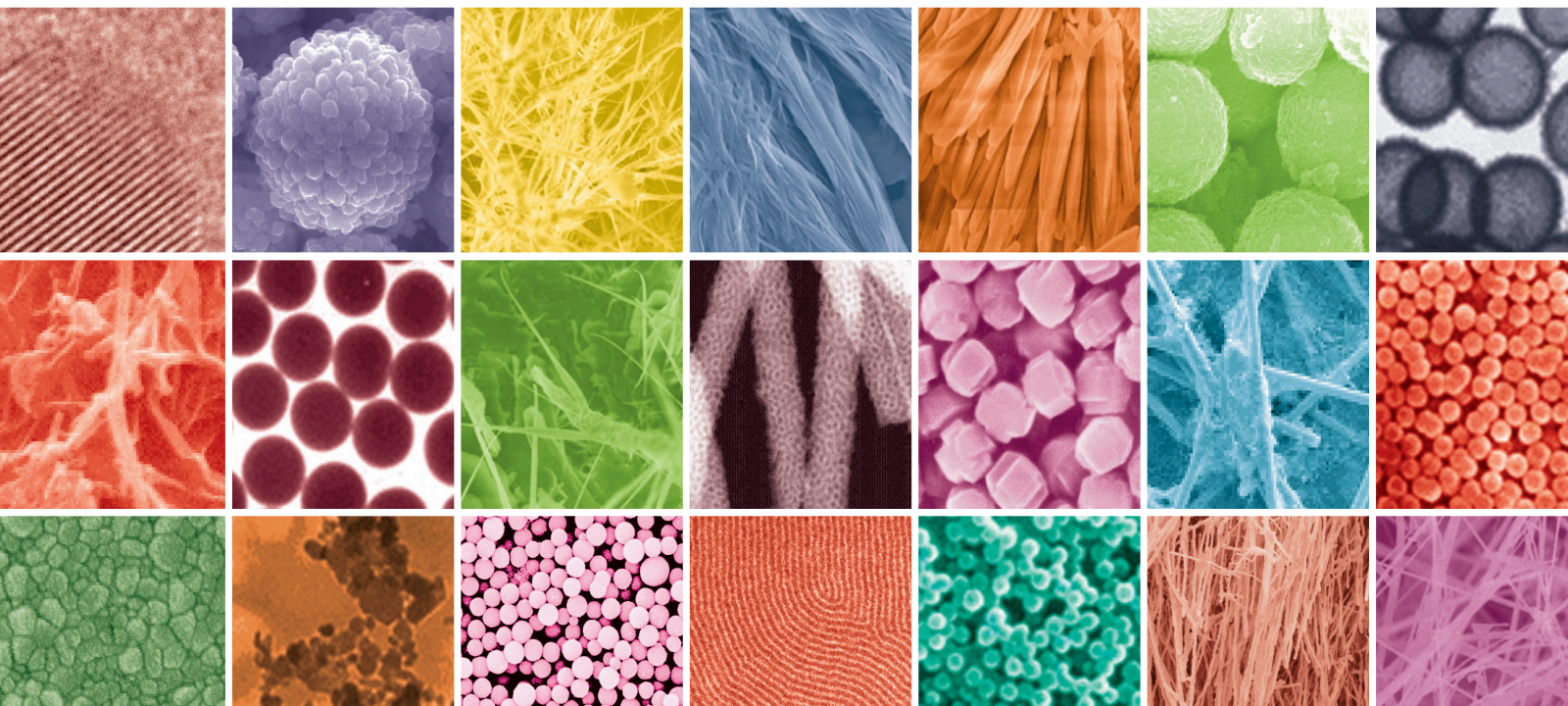


Micro and Nano Sensors from Additive Manufacturing

Lead Guest Editor: Sezgin Ersoy

Guest Editors: Pooyan Makvandi and Ehsan Nazarzadeh Zare





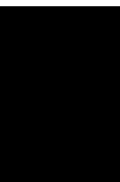
Micro and Nano Sensors from Additive Manufacturing

Journal of Nanomaterials

Micro and Nano Sensors from Additive Manufacturing

Lead Guest Editor: Sezgin Ersoy

Guest Editors: Pooyan Makvandi and Ehsan
Nazarzadeh Zare



Copyright © 2022 Hindawi Limited. All rights reserved.

This is a special issue published in "Journal of Nanomaterials." All articles are open access articles distributed under the Creative Commons Attribution License, which permits unrestricted use, distribution, and reproduction in any medium, provided the original work is properly cited.

Chief Editor

Stefano Bellucci, Italy

Editorial Board



Nagamalai, India
Buzuayehu Abebe, Ethiopia
Domenico Acierno, Italy
Ümit Ağbulut, Turkey
Katerina Aifantis, USA
Ibrahim Alarifi, Saudi Arabia
Nageh K. Allam, USA
Martin Andersson, Sweden
Raul Arenal, Spain
Hassan Azzazy, Egypt
Vincenzo Baglio, Italy
Lavinia Balan, France
Thierry Baron, France
Andrew R. Barron, USA
Enrico Bergamaschi, Italy
Debes Bhattacharyya, New Zealand
Sergio Bietti, Italy
Raghvendra A. Bohara, India
Mohamed Bououdina, Saudi Arabia
Victor M. Castaño, Mexico
Albano Cavaleiro, Portugal
Bhanu P. S. Chauhan, USA
Shafiqul Chowdhury, USA
Yu-Lun Chueh, Taiwan
Elisabetta Comini, Italy
Giuseppe Compagnini, Italy
David Cornu, France
Miguel A. Correa-Duarte, Spain
P. Davide Cozzoli, Italy
Anuja Datta, USA
Loretta L. Del Mercato, Italy
Yong Ding, USA
Yu Dong, Australia
Zehra Durmus, Germany
Ovidiu Ersen, France
Ana Espinosa, France
Claude Estournès, France
liyuxing@xaut.edu.cn Eswaramoorthy, India
Giuliana Faggio, Italy
Andrea Falqui, Saudi Arabia
Matteo Ferroni, Italy
Ilaria Fratoddi, Italy
Chong Leong Gan, Taiwan
Siddhartha Ghosh, Singapore
Filippo Giubileo, Italy
Iaroslav Gnilitskiy, Ukraine
Fabien Grasset, Japan
Jean M. Greneche, France
Kimberly Hamad-Schifferli, USA
Simo-Pekka Hannula, Finland
Michael Harris, USA
Yasuhiko Hayashi, Japan
Michael Z. Hu, USA
Zafar Iqbal, USA
Balachandran Jeyadevan, Japan
Xin Ju, China
Hassan Karimi-Maleh, Iran
Antonios Kelarakis, United Kingdom
Ali Khorsand Zak, Iran
Philippe Knauth, France
Prashant Kumar, United Kingdom
Eric Le Bourhis, France
Shijun Liao, China
Meiyong Liao, Japan
Silvia Licoccia, Italy
Nathan C. Lindquist, USA
Zainovia Lockman, Malaysia
Jim Low, Australia
Gaurav Mago, USA
Muhamamd A. Malik, United Kingdom
Ivan Marri, Italy
Laura Martinez Maestro, United Kingdom
Sanjay R. Mathur, Germany
Tony McNally, United Kingdom
Yogendra Mishra, Denmark
Paulo Cesar Morais, Brazil
Paul Munroe, Australia
Jae-Min Myoung, Republic of Korea
Rajesh R. Naik, USA
Albert Nasibulin, Russia
Toshiaki Natsuki, Japan
MU NAUSHAD, Saudi Arabia
Hiromasa Nishikiori, Japan
Sherine Obare, USA
Won-Chun Oh, Republic of Korea
Abdelwahab Omri, Canada
Ungyu Paik, Republic of Korea
Dillip K. Panda, USA

Mazeyar Parvinzadeh Gashti, Canada
Edward A. Payzant, USA
Alessandro Pegoretti, Italy
Oscar Perales-Pérez, Puerto Rico
Jorge Pérez-Juste, Spain
Suresh Perumal, India
Alexey P. Popov, Finland
Ram Prasad, India
Thathan Premkumar, Republic of Korea
Helena Prima-García, Spain
Alexander Pyatenko, Japan
Haisheng Qian, China
You Qiang, USA
Philip D. Rack, USA
Mohammad Rahimi-Gorji, Belgium
Baskaran Rangasamy, Zambia
Ilker S. Bayer, Italy
Lucien Saviot, France
Shu Seki, Japan
SENTHIL KUMARAN SELVARAJ, India
Gaurav Sharma, India
Donglu Shi, USA
Jagpreet Singh, India
Surinder Singh, USA
Bhanu P. Singh, India
Vladimir Sivakov, Germany
Pingan Song, Australia
Adolfo Speghini, Italy
Kishore Sridharan, India
Marinella Striccoli, Italy
Andreas Stylianou, Cyprus
Fengqiang Sun, China
Ashok K. Sundramoorthy, India
Angelo Taglietti, Italy
Bo Tan, Canada
Leander Tapfer, Italy
Valeri P. Tolstoy, Russia
Muhammet S. Toprak, Sweden
Sri Ramulu Torati, Republic of Korea
R. Torrecillas, Spain
Achim Trampert, Germany
Adriana Trapani, Italy
Takuya Tsuzuki, Australia
Tamer Uyar, USA
Cristian Vacacela Gomez, Ecuador
Luca Valentini, Italy
Viet Van Pham, Vietnam

Antonio Vassallo, Italy
Ester Vazquez, Spain
Ajayan Vinu, Australia
Ruibing Wang, Macau
Magnus Willander, Sweden
Zhi Li Xiao, USA
Ping Xiao, United Kingdom
Yingchao Yang, USA
Hui Yao, China
Yoke K. Yap, USA
Dong Kee Yi, Republic of Korea
Jianbo Yin, China
William Yu, USA
Michele Zappalorto, Italy
Wenhui Zeng, USA
Renyun Zhang, Sweden



Contents

Micro and Nano Sensors from Additive Manufacturing

Ehsan Nazarzadeh Zare , Pooyan Makvandi , and Sezgin Ersoy 

Editorial (2 pages), Article ID 9835910, Volume 2022 (2022)

Manufacturing of Microfluidic Sensors Utilizing 3D Printing Technologies: A Production System

Danial Khorsandi, Mehrab Nodehi, Tayyab Waqar , Majid Shabani, Behnam Kamare, Ehsan Nazarzadeh Zare, Sezgin Ersoy , Mohsen Annabestani, Mehmet Fatih Çelebi, and Abdullah Kafadenk




Review Article (16 pages), Article ID 5537074, Volume 2021 (2021)

Design and Analysis Comparison of Surface Acoustic Wave-Based Sensors for Fabrication Using Additive Manufacturing

Tayyab Waqar  and Sezgin Ersoy 




Research Article (12 pages), Article ID 5598347, Volume 2021 (2021)

Lifetime Prediction for a Cell-on-Board (COB) Light Source Based on the Adaptive Neuro-Fuzzy Inference System (ANFIS)

İsmail Kıyak , Gökhan Gökmen , and Gökhan Koçyiğit 



Research Article (10 pages), Article ID 6681335, Volume 2021 (2021)

Design and Analysis of a Laminar Diffusion-Based Micromixer with Microfluidic Chip

Osman Ulkir , Oguz Girit , and Ishak Ertugrul 


Research Article (10 pages), Article ID 6684068, Volume 2021 (2021)

A Review Study on Mechanical Properties of Obtained Products by FDM Method and Metal/Polymer Composite Filament Production

Ümit Çevik  and Menderes Kam 

Review Article (9 pages), Article ID 6187149, Volume 2020 (2020)

A Novel Label-Free Biosensor for Detection of HE4 in Urine Based on Localized Surface Plasmon Resonance and Protein G Directional Fixed

Ruiqi Duan and Mingrong Xi 

Research Article (7 pages), Article ID 8613240, Volume 2020 (2020)

Editorial

Micro and Nano Sensors from Additive Manufacturing

Ehsan Nazarzadeh Zare ¹, **Pooyan Makvandi** ² and **Sezgin Ersoy** ³

¹College Damghan University, Damghan, Iran

²Istituto Italiano di Tecnologia, Centre for Materials Interfaces, Pontedera, 56025 Pisa, Italy

³Marmara University, Technology Faculty Mechatronic Engineering, Istanbul, Turkey

Correspondence should be addressed to Sezgin Ersoy; ersoy@marmara.edu.tr

Received 9 March 2022; Accepted 9 March 2022; Published 8 April 2022

Copyright © 2022 Ehsan Nazarzadeh Zare et al. This is an open access article distributed under the Creative Commons Attribution License, which permits unrestricted use, distribution, and reproduction in any medium, provided the original work is properly cited.

Developments in the field of fabrication technologies have positively affected, besides many other fields, the sensor technologies too. Researches are being done for utilizing those newly developed technologies for the fabrication of sensors [1].

Additive manufacturing technologies have greatly expanded their potential thanks to many processing technologies from nanoparticles to dielectric multiproduction methods and sub-micro processing technologies.

The microelectromechanical system, called MEMS, is a technology used to create integrated devices or systems from basic components such as mechanics and electricity, and the nanoelectromechanical system (NEMS) can be formed by performing this process in nanodimensions. [2–4].

Surface [5] and body [6] micromachining and traditional methods such as Lithography, Galvanoformung, and Abformung [7] are frequently used in MEMS production. By using this traditional method, products with a more precise, small, and measurable working principle can be produced. However, this is a factor that increases costs. Additive manufacturing technologies and traditional methods can eliminate these costly disadvantages. With small-scale laboratories, time, space, and cost-intensive processes such as sourcing, storage, transportation, and storage can be avoided. These small laboratories can operate like a factory, producing 3D products such as microfluidics [8–10], micro-mechanical systems [11, 12], optical systems [13], cell structures [14], and biomedical devices [14–18].

Integrated circuits (ICs) can be produced on scales ranging from a few micrometers to millimeters using batch pro-

cessing techniques. These devices or systems are capable of sensing, controlling, activating, and generating macroscale effects [19, 20]. Mechanical microstructures, microsensors, microconductors, and microelectronics integrated into silicon chip devices form MEMS technology. The components of MEMS devices are generally microscopic. Lifts, gears, pistons, engines, and steam engines are manufactured by MEMS [21, 22]. However, this technology is not just about miniaturizing mechanical components or making something out of silicone. It is a fabrication technology developed to design and build integrated electronics using mass production techniques as well as complex mechanical devices, and systems [23]. The MEMS is the latest technology in mechanical, electrical, electronic, and chemical engineering. The MEMS consist of mechanical, electrical systems with a size in microns. It is a technology used to minimize systems. Electrical components such as inductors and capacitors can be significantly improved compared to their integrated counterparts when manufactured using MEMS and nanotechnology [24, 25]. With the use of MEMS technology, great attention was paid to expanding new production processes, semiconductor devices, and microscale resistors to be used in various optoelectronic devices [26]. Additive manufacturing, which is generally called three-dimensional (3D), will continue to change the way of design, production, and service in MEMS and NEMS technologies. With this production technology, we can meet the demands of many product ranges from the medical field to space technologies, from microfluidics to optical devices [27]. In addition, the complex geometries of micro/nanosized products can be

produced with high precision and production can be carried out at much lower costs. Keeping these two parameters together can be defined as superior production capability. It will be able to respond to the required mass production or special production. In the near future, it is possible to produce products that meet special engineering demands such as micro-nano composites and magnetic structures. The special issue of micro- and nanosensors from additive manufacturing opens to present advances in additive manufacturing and micro- and nanosensor.

Conflicts of Interest

The authors declare that there is no conflict of interest regarding the publication of this Editorial.

Ehsan Nazarzadeh Zare
Pooyan Makvandi
Sezgin Ersoy

References

- [1] T. Waqar and S. Ersoy, "Direction-action research for design, analysis, and fabrication of temperature sensor using micro-streolitography technique," in *The International Aluminum-Themed Engineering and Natural Sciences Conference in Seydişehir/TURKEY (IATENS'19)*, Konya, Turkey, October 4 -6 2019.
- [2] R. Crescenzi, M. Balucani, and N. P. Belfiore, "Operational characterization of CSFH MEMS technology based hinges," *Journal of Micromechanics and Microengineering*, vol. 28, no. 5, pp. 055012–055021, 2018.
- [3] V. A. Lifton, G. Lifton, and S. Simon, "Options for additive rapid prototyping methods (3-D printing) in MEMS technology," *Rapid Prototyping Journal*, vol. 20, no. 5, pp. 403–412, 2014.
- [4] O. Ulkir, I. Ertugrul, O. Girit, and S. Ersoy, "Modeling and thermal analysis of micro beam using COMSOL multiphysics," *Thermal Science*, vol. 25, no. Spec. issue 1, pp. 41–49, 2021.
- [5] J. M. Bustillo, R. T. Howe, and R. S. Muller, "Surface micromachining for microelectromechanical systems," *Proceedings of the IEEE*, vol. 86, no. 8, pp. 1552–1574, 1998.
- [6] M. Hoffmann and E. Voges, "Bulk silicon micromachining for MEMS in optical communication systems," *Journal of Micromechanics and Microengineering*, vol. 12, no. 4, pp. 349–360, 2002.
- [7] J. Hormes, J. Göttert, K. Lian, Y. Desta, and L. Jian, "Materials for LiGA and LiGA-based microsystems," *Nuclear Instruments and Methods in Physics Research Section B: Beam Interactions with Materials and Atoms*, vol. 199, pp. 332–341, 2003.
- [8] S. Keçili, *Fabrication of microfluidic devices via 3D printer*, Mühendislik ve Fen Bilimleri Enstitüsü, 2019.
- [9] Y. Li, Y. Fang, J. Wang et al., "Integrative optofluidic microcavity with tubular channels and coupled waveguides via two-photon polymerization," *Lab on a Chip*, vol. 16, no. 22, pp. 4406–4414, 2016.
- [10] I. Unalli, S. Ersoy, and I. Ertugrul, "Microfluidics chip design analysis and control," *Journal of Mechatronics and Artificial Intelligence in Engineering*, vol. 1, no. 1, pp. 2–7, 2020.
- [11] G. Nelson, R. A. Kirian, U. Weierstall et al., "Three-dimensional-printed gas dynamic virtual nozzles for x-ray laser sample delivery," *Optics Express*, vol. 24, no. 11, pp. 11515–11530, 2016.
- [12] I. Ertugrul and T. Waqar, "Withdrawal notice: fabrication of bidirectional electrothermal microactuator by two-photon polymerization," *Current Nanoscience*, vol. 16, 2020.
- [13] C. Peters, M. Hoop, S. Pané, B. J. Nelson, and C. Hierold, "Degradable magnetic composites for minimally invasive interventions: device fabrication, targeted drug delivery, and cytotoxicity tests," *Advanced Materials*, vol. 28, no. 3, pp. 533–538, 2016.
- [14] U. T. Sanli, H. Ceylan, I. Bykova et al., "3D nanoprinted plastic kinoform X-ray optics," *Advanced Materials*, vol. 30, no. 36, 2018.
- [15] K. S. Worthington, L. A. Wiley, E. E. Kaalberg et al., "Two-photon polymerization for production of human iPSC-derived retinal cell grafts," *Acta Biomaterialia*, vol. 55, pp. 385–395, 2017.
- [16] C. A. Lissandrello, W. F. Gillis, J. Shen et al., "A micro-scale printable nanoclip for electrical stimulation and recording in small nerves," *Journal of Neural Engineering*, vol. 14, no. 3, article 036006, 2017.
- [17] M. Suzuki, T. Takahashi, and S. Aoyagi, "3D laser lithographic fabrication of hollow microneedle mimicking mosquitos and its characterisation," *International Journal of Nanotechnology*, vol. 15, no. 1/2/3, p. 157, 2018.
- [18] R. Amin, S. Knowlton, A. Hart et al., "3D-printed microfluidic devices," *Biofabrication*, vol. 8, no. 2, 2016.
- [19] A. Morris, "Monolithic integration of RF-MEMS within CMOS," in *2015 International Symposium on VLSI Technology, Systems and Applications*, Hsinchu, Taiwan, 2015.
- [20] A. Fischer, F. Forsberg, M. Lapisa et al., "Integrating MEMS and ICs," *Microsystems & Nanoengineering*, vol. 1, no. 1, p. 15005, 2015.
- [21] M. Tilli, M. Paulasto-Krockel, M. Petzold, H. Theuss, T. Motooka, and V. Lindroos, *Handbook of Silicon Based MEMS Materials and Technologies*, Elsevier, 2015.
- [22] O. Z. Olszewski, R. Houlihan, R. O'Keeffe et al., "A MEMS silicon-based piezoelectric AC current sensor," *Procedia Engineering*, vol. 8, pp. 1457–1460, 2014.
- [23] J. Philippe, *Technology development and analysis of a multi-physic system based on NEMS co-integrated with CMOS for mass detection application (doctoral dissertation)*, Université de Grenoble, 2014.
- [24] P. Pirouznia and B. A. Ganji, "Analytical optimization of high performance and high quality factor MEMS spiral inductor," *Progress In Electromagnetics Research*, vol. 34, pp. 171–179, 2014.
- [25] O. F. Hikmat and M. S. M. Ali, "RF MEMS inductors and their applications—a review," *Journal of Microelectromechanical Systems*, vol. 26, pp. 17–44, 2016.
- [26] J. Marek, "MEMS for automotive and consumer electronics," in *2010 IEEE International Solid-State Circuits Conference - (ISSCC)*, vol. 10, pp. 9–17, San Francisco, CA, USA, 2010.
- [27] D. Khorsandi, M. Nodehi, T. Waqar et al., "Manufacturing of microfluidic sensors utilizing 3D printing technologies: a production system," *Journal of Nanomaterials*, vol. 2021, Article ID 5537074, 16 pages, 2021.

Review Article

Manufacturing of Microfluidic Sensors Utilizing 3D Printing Technologies: A Production System

Danial Khorsandi,¹ Mehrab Nodehi,² Tayyab Waqar ,^{3,4,5} Majid Shabani,^{6,7} Behnam Kamare,^{6,7} Ehsan Nazarzadeh Zare,⁸ Sezgin Ersoy ,^{3,4} Mohsen Annabestani,⁶ Mehmet Fatih Çelebi,⁴ and Abdullah Kafadenk⁹

¹Department of Biotechnology-Biomedicine, University of Barcelona, Barcelona 08028, Spain

²Ingram School of Engineering, Texas State University, San Marcos, TX 78666, USA

³The Institute of Pure and Applied Sciences, Marmara University, Istanbul 34722, Turkey

⁴Department of Mechatronic Engineering, Technology Faculty, Marmara University, Istanbul 34722, Turkey

⁵Arcelik A.S., 34950 Istanbul, Turkey

⁶Istituto Italiano di Tecnologia, Centre for Materials Interfaces, Viale Rinaldo Piaggio 34, 56025 Pontedera, Pisa, Italy

⁷The BioRobotics Institute, Scuola Superiore Sant'Anna, Viale Rinaldo Piaggio 34, 56025 Pontedera, Pisa, Italy

⁸School of Chemistry, Damghan University, Damghan 36716-41167, Iran

⁹UNAM—National Nanotechnology Research Center and Institute of Materials Science and Nanotechnology, Bilkent University, Turkey

Correspondence should be addressed to Sezgin Ersoy; ersoy@marmara.edu.tr

Received 20 January 2021; Accepted 25 July 2021; Published 11 August 2021

Academic Editor: Jianbo Yin

Copyright © 2021 Danial Khorsandi et al. This is an open access article distributed under the Creative Commons Attribution License, which permits unrestricted use, distribution, and reproduction in any medium, provided the original work is properly cited.

3D integrated microfluid devices are a group of engineered microelectromechanical systems (MEMS) whereby the feature size and operating range of the components are on a microscale. These devices or systems have the ability to detect, control, activate, and create macroscale effects. On this basis, microfluidic chips are systems that enable microliters and smaller volumes of fluids to be controlled and moved within microscale-sized (one-millionth of a meter) channels. While this small scale can be compared to microfluid chips of larger applications, such as pipes or plumbing practices, their small size is commonly useful in controlling and monitoring the flow of fluid. Through such applications, microfluidic chip technology has become a popular tool for analysis in biochemistry and bioengineering with their most recent uses for artificial organ production. For this purpose, microfluidic chips can be instantly controlled by the human body, such as pulse, blood flow, blood pressure, and transmitting data such as location and the programmed agents. Despite its vast uses, the production of microfluidic chips has been mostly dependent upon conventional practices that are costly and often time consuming. More recently, however, 3D printing technology has been incorporated in rapidly prototyping microfluid chips at microscale for major uses. This state-of-the-art review highlights the recent advancements in the field of 3D printing technology for the rapid fabrication, and therefore mass production, of the microfluid chips.

1. Introduction

3D integrated microfluidic systems are engineered devices that actualize the precise routing of micro-sized fluidic streams for specific physicochemical and biological applications [1, 2]. Due to such precision, the use of microfluidic devices is commonly known to be able to reduce the con-

sumption of materials and regulate fluid flow in essential microscale environments [3]. The development of microfluid systems took place during the 1970s and has found numerous applications in automobile industry [4–7], medical technology [8–10], printing [11, 12], and sensor systems [13–15], as well as optical devices [16–18]. Despite such vast applications, in general, MEMS products are most commonly

manufactured using traditional methods which include surface microprocessing [19], body microprocessing [20], and LIGA (Lithographie, Galvanoformung, Abformung (Lithography, Electroplating, and Molding)) [21]. These methods provide MEMS products to be more detailed and clearer by increasing the number of manufacturing steps and processing units that, in turn, increases the overall costs associated with the production of MEMS. In the same way, for small lab-scale research, this process generally results in a long and costly cycle which is not favoured. To address this, most recently, additive manufacturing (3D printing) techniques have been introduced which can potentially eliminate the disadvantages of conventional production methods used in microfluidic fabrication. Such 3D products can be used as microfluidics [22–24], micromechanical systems [25, 26], optical systems [27], cell structures [28], and biomedical devices [28–31].

With the term 3D printing being commonly defined as “a process of joining materials to make objects from 3D model data, usually layer upon layer, as opposed to subtractive manufacturing methodologies” [32], 3D printing, in that respect, can potentially actualize rapid and easy prototyping and increase the quality of the produced microfluidic devices using different fabricating techniques. Such techniques to produce microfluidic chips include but are not limited to inject 3D printing, stereolithography (SL), fused deposition modeling (FDM), material jetting, binder jetting, directed energy deposition, and vat photopolymerization [32, 33].

In addition to the type of printing technique used, the possibility of printing materials with high details using different printing filaments is another feature of 3D-printed microfluidic devices. The high transparency, as a result of utilizing transparent filament, can effectively allow careful monitoring of the fluid flow [1, 32, 34]. As a result, depending upon the designated uses, resolution, colour, printing dimensions, and proper filament can, therefore, be utilized.

This review presents the wide range of 3D printing technology and their application towards the fabrication of microfluidic sensors and systems. Introduction regarding the microfluidic chip technology, along with clean room, is provided at the beginning which is followed by the implementation of the state-of-the-art 3D printing technology and their applications for the fabrications of such systems.

2. Microfluidic-Chip Technology

Microfluidic chips can be defined as a collection of microchannels fabricated or constructed into a material, such as silicon, glass, and polymer. They contain a mixture of interconnected microchannels, which forms the microfluidic chip, to perform the target operation or detection. These microchannels are interfaced to the outside world through the chip, and it is via these holes that gases or fluids are introduced and removed from the microchip. Figure 1 shows the technological advancements that have been achieved right from the invention of photolithography to the lab on chip [35].

From Figure 1, it can be deduced that the developments that have been made in the field of microfluidic technology are derived from the advancements in integrated circuits

(IC) and photolithography [36]. The development of micro-flow sensors, micropumps, and microvalves dominates the early phase of microfluidics [37–39].

An example of such implementation of microfluidic chip has been presented in the form of a T-junction which is used to measure pressure [40]. It has been found that for filtration purposes, the “T” connections on microfluidics become blocked over time by fluids in droplet form thus causing numerous application issues such as unwanted pressure increase and variation in fluid velocity and acceleration, producing undesirable results. As viscosity of the given fluid varies, viscosity retention conditions in microfluidic channels take place. For this reason, clogging may be inevitable for microlevel channels. Figure 2 shows details regarding the increase in blockage situation in a microfluidic chip according to time. Based on the figure, the output over “T” suddenly drops to $8\ \mu\text{m}$ level. At 0.4 ms, it starts to block in the form of droplets in the channel it comes from. Therefore, other devices or methods should be incorporated in order to resolve this issue. One way to address this tendency, for instance, is the use of Laplace sensors to solve the problem of droplet blocking at such return or connection points. As shown in Figure 2, a turn in the “w” radius is put and thus, although the area used is upstream, no narrowing has occurred in the channels.

Although microfluidic chip technology is still in its infancy, viscosity and laminar flow are the most common issues associated with its applications. According to Sanli et al. [28], viscosity can be divided into Newtonian- and non-Newtonian-type fluids. With the former referring to a fluid whose viscosity does not change when a force is applied (e.g., water, gasoline, and alcohol), the latter refers to a varying viscosity state of fluid when the applied force is a determinant of the materials’ viscosity (e.g., starch-water or ketchup). In the same way, the flow motion of this process can be classified as laminar and turbulent flow which refers to the regularity of flow of a fluid in a given medium.

Extending on the above application, a lab-on-a-chip microfluidic device has been presented by Chien and Parce [41]. An algorithm has been developed, to address the clogging issue, which works by calculating the pressures in the multiport flow control study for lab-on-a-chip microfluidic device. For this purpose, additional devices with an external pressure increasing multiport input have been incorporated. Through this process, a pressurized fluid such as the dye mixture and enzyme assay is often used along with a computer-controlled multichamber pressure/vacuum control unit with voltage and current input which has been built using the syringes used in the system (see Figure 3).

In this experiment, it has been revealed that the external pressure control and the predicted expectations are very close to each other. In this way, it was emphasized that a new way can be incorporated for biochemical experiments with the lab on a chip. It was further noted that the ability to control fluids flowing in microfluidics is always a leading feature. In addition, it was shown in that it is possible to direct many fluids within channels using a multiport system.

Many similar terms such as “Micro-fluids,” “MEMS-fluids” or “Bio-MEMS,” and “microfluidics” have also emerged over time as the name of a new research discipline

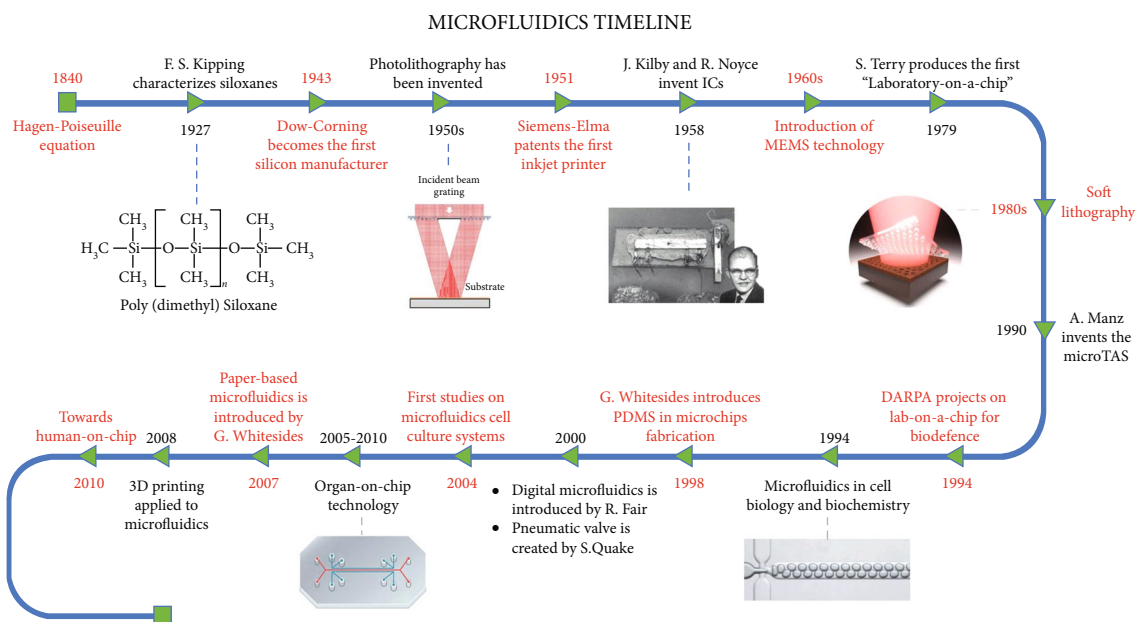


FIGURE 1: Timeline indicating advancements in the microfluidic technology [35].

dealing with transport paths and liquid-based devices at microscopic length scales. Figure 4 shows a scale to better distinguish microfluids or roughly MEMS and nanofluids. These devices can be completely distinguished from each other by size or volume [43–51].

Microfluidic devices have microchannels, having one dimension of at least 1 to 100 μm , that deal with the manipulation of liquids or gases [53, 54]. The fabrication of these microchannels having such dimensions is due to the silicon microprocessing-enabled channels that allow the features to be produced with a precision of 1 μm . This technological achievement has enabled the reduction of micro- (10^{-6}) litres to atto- (10^{-18}) litres of liquid volume. For further illustration, the analytical and economic advantages of microfluidics are listed in Table 1.

2.1. Microelectromechanical Systems (MEMS). The term MEMS nowadays is used to refer to almost all types of miniaturised devices, such as 3D microstructures, mostly fabricated from silicon semiconductor while utilizing techniques that are the derivative of the recent developments in microfabrication industry [55]. With the development of semiconductor technologies, different MEMS production techniques have also started to develop. MEMS manufacturing technique procedures are somewhat similar as compared with ICs. With microfabrication, a large number of cheaper-cost products have been produced. Special microprocessing techniques have been developed for MEMS devices that cannot potentially be produced with traditional manufacturing techniques. These production techniques have advanced with the development of technology and can be classified as follows [56]:

- (i) Bulk micromachining
- (ii) Surface micromachining

- (iii) Wafer bonding
- (iv) Lithographie, Galvanoformung, Abformung (LIGA)
- (v) Other microprocessing techniques

The bulk micromachining technique is the oldest microprocessing technique. It is also highly preferred in MEMS technology. In this process, the material is fabricated within the desired limit via a number of steps. Bulk microprocessing is generally done in 2 different ways as wet and dry etching [57]. In wet etching, an acid-based liquid is applied on the specified material and is used which is widely used in MEMS production due to its fast and high selectivity. Nonetheless, the rate of etching can vary depending on many factors. Crystal structure of the material, residence time in the solution, type of doping, etc. are commonly known factors that affect this process [58]. A process which relies on the removal of the masked semiconductor material via the exposure to ion bombardment and reactive gases resulting in removing the masked portion of that material is known as dry etching [59]. These processes are further developed to make the final product, i.e., microfluidic chips, much smaller in size.

In addition, there are two types of wet chemical etching in the body microprocessing. These are classified as isotropic and anisotropic. In isotropic wet etching, since the rate of etching does not depend on the crystal structure of the material, the etching is distributed equally in all directions. It is made with chemicals such as hydrofluoric acid (HF) and hydrochloric acid (HCl). Illustrated in Figure 5, abrasion proceeds at the same speed in all directions and circular-shaped structures are obtained on the material. The anisotropic etching, however, does not spread equally in all directions since the rate of etching depends on the crystal structure of the material. It is made using solutions such as potassium hydroxide (KOH) and tetramethylammonium hydroxide (TMAH). As can be seen in Figure 5, it carries

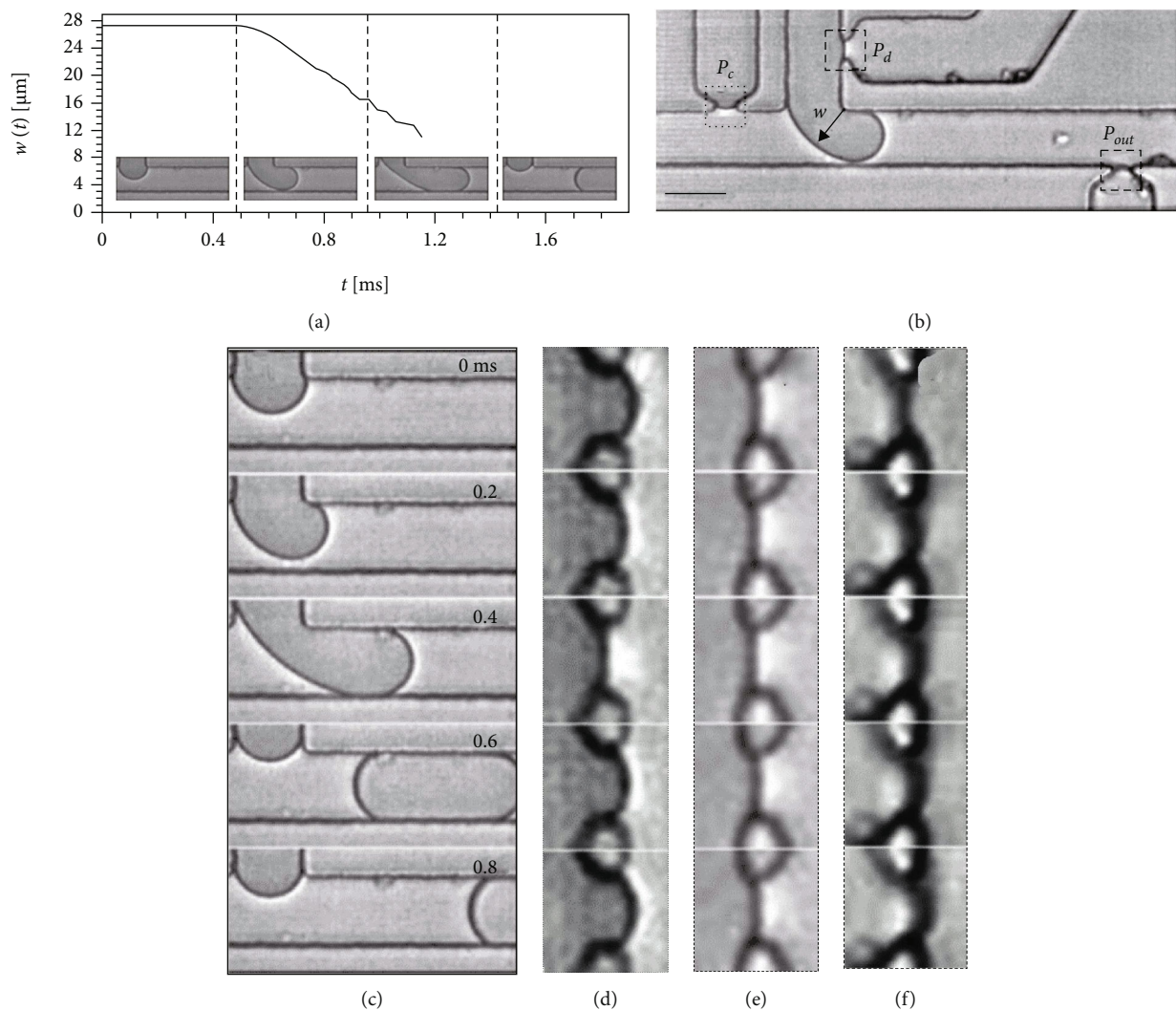


FIGURE 2: Microfluidic droplet: (a) time-dependent measurements of the emerging drop contour width at its narrowest point; (b) T-junction drop maker with three Laplace sensors used to measure the pressures in the continuous fluid upstream of the drop maker P_c , downstream of the drop maker P_{out} , and in the dispersed fluid P_d ; (c) image sequence showing the evolution of the formation of a drop; (d–f) simultaneous snapshots of the interfaces at the Laplace sensors at high magnification. Reprinted by permission from [40].

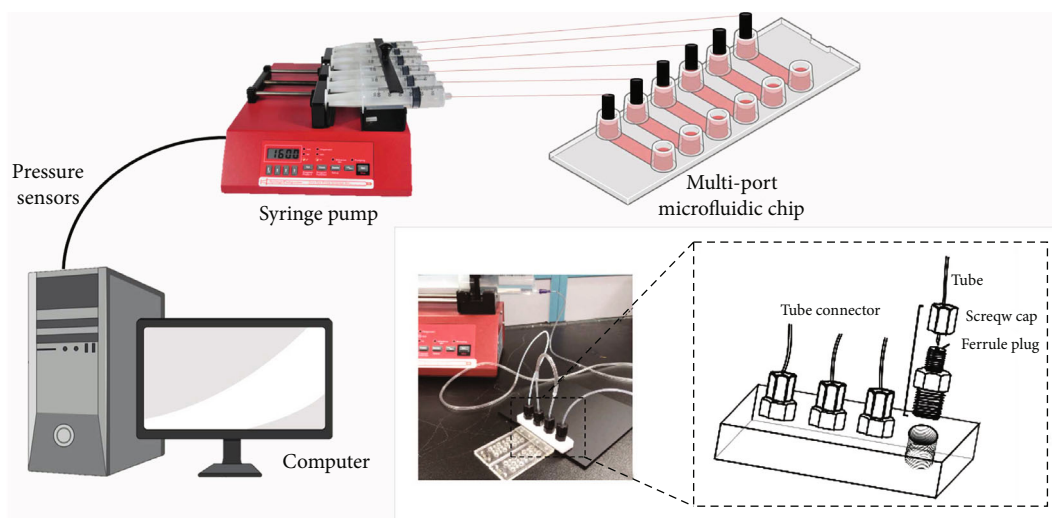


FIGURE 3: Multiport microfluidic connection diagram. Modified from [42].

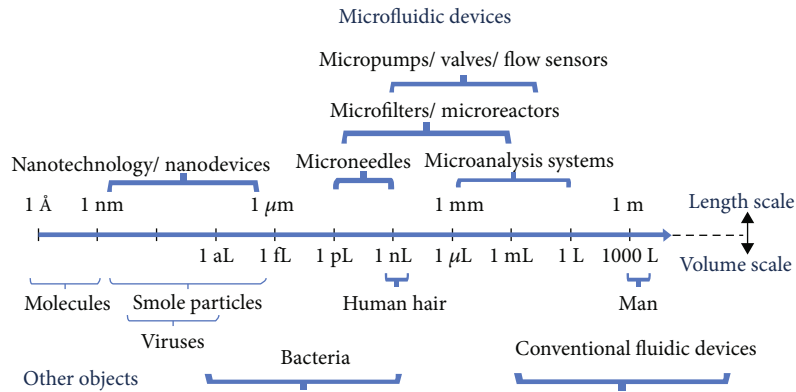


FIGURE 4: Some sample scales for comparison of microfluidic and nanofluidic device sizes [52].

TABLE 1: Advantages of microfluidics.

Microfluid advantages	Description
Less sample and reagent consumption	Microfluidic devices require less sample volume for traditional methods or analyses.
Improved heat transfer	The higher surface area/volume ratio of microfluidic channels increases the effective thermal dispersion.
Faster separations	Stronger electric fields cause faster sample throughput.
Electrokinetic orientation	Electroosmotic flow allows fluids to be pumped with a flat “plug-like” velocity profile applied only over electric fields.
Low power consumption	Fewer components and improved heat dissipation require less power input.
Paralleling	Several assays can be mixed or analysed in parallel on a single chip.
Portability	Thanks to system integration and low power consumption, it can perform portable conductive analysis.
Improved separation efficiency	Efficiency in electrophoretic and chromatographic separations is proportional to L/d .

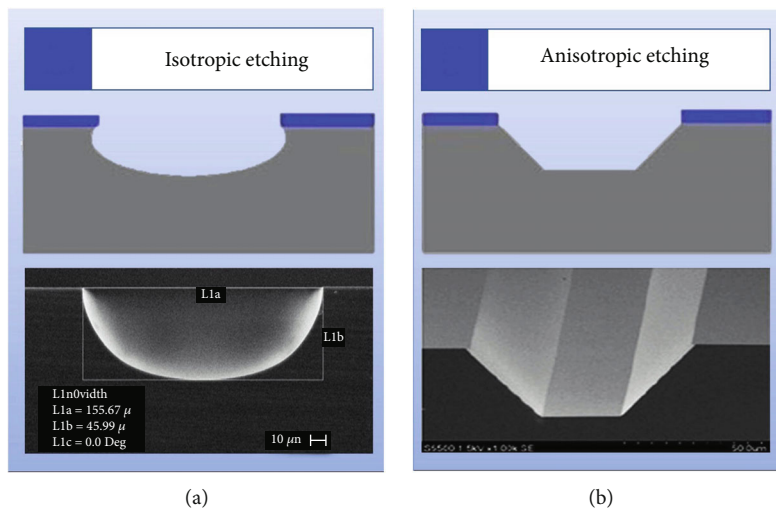


FIGURE 5: Isotropic (a) and anisotropic (b) etching. Reproduced with permission from [60, 61].

out different etchings in different crystal directions. The speed of erosion is also a variable with direct relation with the atomic density.

In general, however, any etching process requires a masking material that has a high selectivity with respect to the substrate material. Common masking materials for isotropic wet etching include silicon dioxide and silicon nitride. Silicon nitride has a lower wear rate compared to silicon dioxide and is therefore used more frequently [62].

The most commonly used method in the body microprocessing technique is deep reactive-ion etching (DRIE) with dry etching. DRIE is one of the new technologies of MEMS device manufacturing. With this technology, very high abrasion depth and height can be achieved. Assuming that the substrate plate used is silicon, the etching depth with this method can be in size of a thousand of microns [62].

Surface microprocessing is created by coating thin layers on the silicon plate. In body microprocessing, this is the

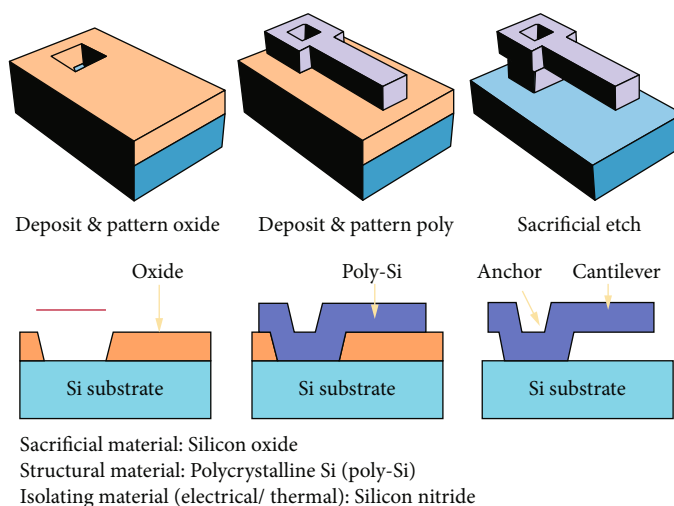


FIGURE 6: Microfluidic surface microprocessing, reprinted with permission from [63].

opposite, and structures are created by material removal. As shown in Figure 5, a temporary coating (for example silicon dioxide) is first made on a plate. Then, the material of the final MEMS device to be produced is coated on this structure using a thin film. With the completion of these processes, the temporary material is removed with some solutions and the real material remains.

Examining the steps for the surface microprocessing, presented in Figure 6, it can be observed that the process is a bit complicated and likely to cause problems. Whether the properties of all materials and solutions to be used in this technique are suitable or not for this method should be compared in detail. One of the most important issues in this technique is that the solution to be applied to remove the temporary layer should be very careful against damage to the permanent material. It should be noted that etching processes cannot be too fast and effective at the same time.

The method of forming multiple layers at microlevels is commonly called the plate joining microprocessing technique (i.e., wafer bonding). There are three different types of microprocessing techniques used in this regard that include direct bonding, anodic bonding, and bonding using interlayer. In order for these layers to be combined, the layers must be smooth and clean [62].

Anodic coating, which is a special surface coating for aluminium, is applied as a sodium glass or silicone coating. This relationship is established by applying certain temperatures and tension. Metal, polymer, or glass plate is used for these intermediate plates. The direct joining method is usually achieved by adhering to the silicone layers [64, 65].

Lithography, Galvanoformung (electroplating), Abformung (also press molding) is a microprocessing technique consisting of words such as LIGA [66]. It is another technique that has emerged to respond to the demands and needs of the developing MEMS devices. It is the method that enables MEMS devices that cannot be produced with silicon processing techniques to be produced in 3D-printed plastic structures, metal ceramics, etc. where LIGA technique is employed to reveal the structures.

Another micromachining technique, laser micromachining, works by applying energy to the required area by sending very short light through factors such as wavelength, energy, and power, depending on the laser type. Electrodischarge micromachining is another widely preferred microprocessing technique for materials with electrical conductivity. It is especially preferred in complex systems. Microprocessing with a focused ion beam is preferred for very small sizes (nanolevels). The main element of microprocessing, in this technique, is the voltage rise and fall. Voltages can range from a few kiloelectron volts (keV) to a hundred times kiloelectron volts [62].

In general, microfluidic chips are devices that work on the principle of liquid transport, which significantly reduces the complexity and power consumption of mechanical tests. For example, electroosmosis is a process in which bulk electrolytic fluid in a channel is entrained through viscosity by moving ions near a naturally charged channel wall by the application of an electric field [67].

Several analytical performance measures can be improved through miniaturization. One of the most obvious advantages of the smaller channel sizes is reduced reagent consumption, resulting in less waste and more efficient testing. Reduced reagent consumption becomes particularly advantageous for many biological applications where reagents can be very expensive and sample volumes are often limited. In addition, the separation efficiency of chromatographic and electrophoretic systems is proportional to L/d (the length of the separation channel over its diameter). Therefore, long and narrow channels provide improved peak-to-peak resolution.

Because they are very narrow, microfluidic channels also have flowed with very low Reynolds numbers; i.e., $Re < 1$ flow is laminar. Such laminar flows prevent additional dispersion from affecting the bandwidth of a separate plug. However, diffusion is more pronounced on smaller scales and is advantageous for mixing applications where mixing can only be done by diffusion, despite very laminar flow. Additionally, narrow channels dissipate heat more efficiently and allow

stronger electric fields in electrophoretic systems without adverse heating effects on separation efficiency. As a result, tests will take less time as higher electric fields lead to faster separations.

2.2. Cleanroom System. The cleanroom system is a system used in production or scientific research and does not contain high levels of environmental pollutants. Some special measures should be taken in order to provide the desired level of cleanliness in the cleanroom system. Clean rooms are used in many sectors such as for the manufacturing of semiconductor devices, which is a key ingredient of MEMS [68].

The modern cleanroom system was invented by the American physicist Willis Whitfield. This work was conducted at the Sandia National Laboratory. Whitfield developed the cleanroom system in a modern way by using the filter system effectively in his study. Earlier cleanroom systems had many problems with unpredictable airflows [66, 68, 69].

Clean rooms can be used in any industrial area where small levels of particles can adversely affect the production process and can differ in size and complexity. Cleanroom systems are mainly used in the fields of biotechnology, semiconductor production, life sciences, pharmaceutical industry, and medical device production [66, 68, 70].

Since cleanroom systems are used in many applications, there are many cleanroom classes according to their usage areas. The HVAC (Heating, Ventilating, and Air Conditioning) design that the cleanroom will use is also made accordingly. HVAC ventilation concerns many related areas.

Cleanroom systems are classified for ease of use. There are many classification standards available today. The most commonly used of these classification types is Federal Standard 209E and ISO 14644 Clean Room Standard that has been prepared for cleanroom systems and cleanroom environments [71].

As given in Table 2, for example, the habitable ambient air corresponding to the ISO 9 class contains a maximum of 35 200 000 particles with a diameter of $0.5\ \mu\text{m}$ and larger per cubic meter. An ISO 4 class cleanroom allows a maximum of only 352 particles per cubic meter of $0.5\ \mu\text{m}$ or greater. The actuator in this study was also produced in class 4 of ISO.

To control the fabrication processes, generally, validation procedures are carried out. Validation processes, in that sense, can be defined as control of systems and documentation. The main purpose of the validation process is to control every part of the fabrication process [71].

Cleanroom systems can withstand air, humidity, heat, and temperature controls and contain certain particles according to class types. Many tests are carried out in the cleanroom. The purpose of these tests is to understand that the system is working correctly. Otherwise, problems may arise according to the application to be made. The main tests performed are as follows:

- (i) Measurements regarding the number of particles
- (ii) Measurements related to pressure gauge operations

- (iii) Humidity and temperature treatments

- (iv) Control tests

- (v) Air control tests

- (vi) Filter (Hepa) control tests [71]

2.3. MEMS Manufacturing Techniques with 3D Printer. Recently, with the development of MEMS production methods, 3D printers, which can manufacture materials through the additive manufacturing technique, have been a novel way for the production of these devices due to both cost-effectiveness and the ease in manufacturing. The ongoing requirements such as the basic workflow and clean room used in the production of MEMS make production processes difficult from time to time. However, by using 3D printing, MEMS can be produced in any potential environment with the additive manufacturing method (Figure 7).

Due to their rapid design iteration and because of their low production, infrastructure, and maintenance costs, 3D printing continues to be an encouraging alternative compared to traditional techniques such as lithography. The recent development in the technology allows the fabrication of complex microfluidic devices (Figure 8), makes procedures faster, and is cheaper, therefore, making it attractive to more users.

With the recent advancements in 3D printing technologies, highly complex microfluidic devices can be fabricated via single-step, rapid, and cost-effective protocols, making microfluidics more accessible to users.

2.4. Photopolymerization 3D Printing (Also Stereolithography). Stereolithography refers to one of the earliest additive manufacturing technologies that emerged in the early 1980s, commonly used for creating models and prototypes through a selective curing of a photopolymer by a UV using laser. As a result, the word stereolithography, a combination of the words “stereo = solid” and “lithography = printing by light” is used for this process. After its introduction by 3D systems, other institutions produced microstereolithography system and were able to produce devices capable of 3D production at microlevels. At a microlevel, microstereolithography fabrication techniques used for MEMS fabrication are commonly examined in 3 groups:

- (i) *Projection microstereolithography (mask projection):* projection microstereolithography (P μ SL) is a multifunctional and low-cost process that enables rapid production of ceramic products by 3D microfabrication using complex microsized polymer structures, electrolysis, or resin additives [69]. P μ SL enables the rapid production of complex 3D microsized structures, on a layer-by-layer basis (see Figure 9(a)). In addition, P μ SL uses the most advanced digital microdisplay technology with patterns that are both digital and dynamic. This method combines the prominent features of common stereolithography and projection lithography, creating rapid photopolymerization of all structures with a microlevel layer resolution of UV light. The materials used during the manufacturing

TABLE 2: Cleanroom standards (reproduced from ISO/DIS 14644-1) [72].

ISO classification number (N)	Maximum allowable concentrations (particles/m ³) for particles equal to and greater than the considered sizes shown below ^a					
	0.1 μm	0.2 μm	0.3 μm	0.5 μm	1 μm	5 μm
ISO class 1	10 ^b	d	d	d	d	e
ISO class 2	100	24 ^b	10 ^b	d	d	e
ISO class 3	1 000	237	102	35 ^b	d	e
ISO class 4	10 000	2 370	1 020	352	83 ^b	e
ISO class 5	100 000	23 700	10 200	3 520	832	d, e, f
ISO class 6	1 000 000	237 000	102 000	35 200	8 320	293
ISO class 7	c	c	c	352 000	83 200	2 930
ISO class 8	c	c	c	3 520 000	832 000	29 300
ISO class 9 ^g	c	c	c	35 200 000	8 320 000	293 000

^aAll concentrations in the table are cumulative; e.g., for ISO class 5, the 10 200 particles shown at 0.3 μm include all particles equal to and greater than this size.

^bThese concentrations will lead to large air sample volumes for classification. Sequential sampling procedure may be applied. ^cConcentration limits are not applicable in this region of the table due to very high particle concentration. ^dSampling and statistical limitations for particles in low concentrations make classification inappropriate. ^eSample collection limitations for both particles in low concentrations and sizes greater than 1 μm make classification at this particle size inappropriate, due to potential particle losses in the sampling system. ^fIn order to specify this particle size in association with ISO class 5, the macroparticle descriptor M may be adapted and used in conjunction with at least one other particle size. ^gThis class is only applicable for the in-operation state.

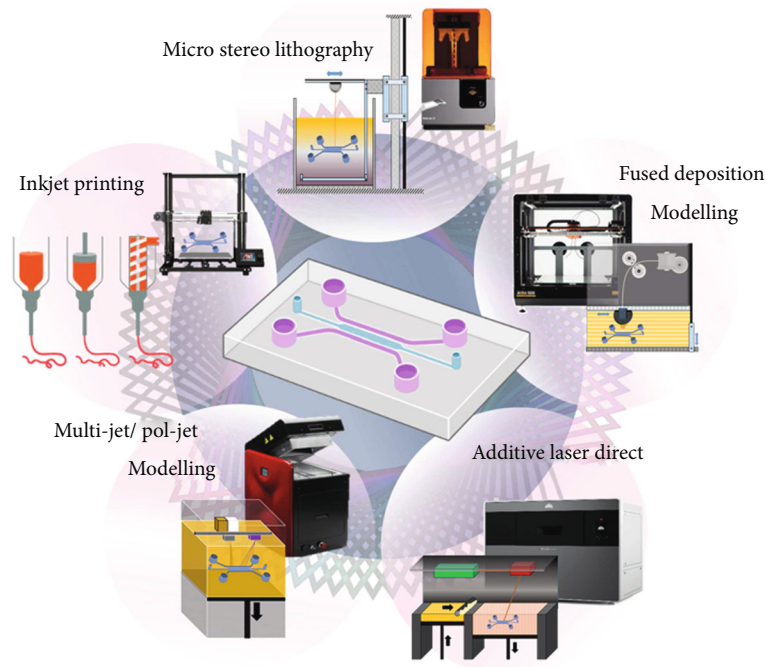


FIGURE 7: Additive manufacturing methods [73–75].

process can be changed easily [81]. The user can control the printing speed, UV light's intensity, and depth/height of the structure, letting them fabricate a variety of complex structures, such as spiral domes, pyramids, and microwells [82, 83] (Figure 9(b))

(ii) *Two-photon polymerization*: another 3D printing technique used is two-photon polymerization

(2PP) method which makes it possible to print out many complex products by making the fabrication production quickly and simply. Also, the high resolution in the printouts allows this technique to stand out [85]. In the 2PP method, it is the reactions that make it possible for the light-sensitive material to polymerize with a resolution of up to 100 nm. Under these conditions, the material is only exposed to the laser beam for femtoseconds (10^{-15} seconds) [86]

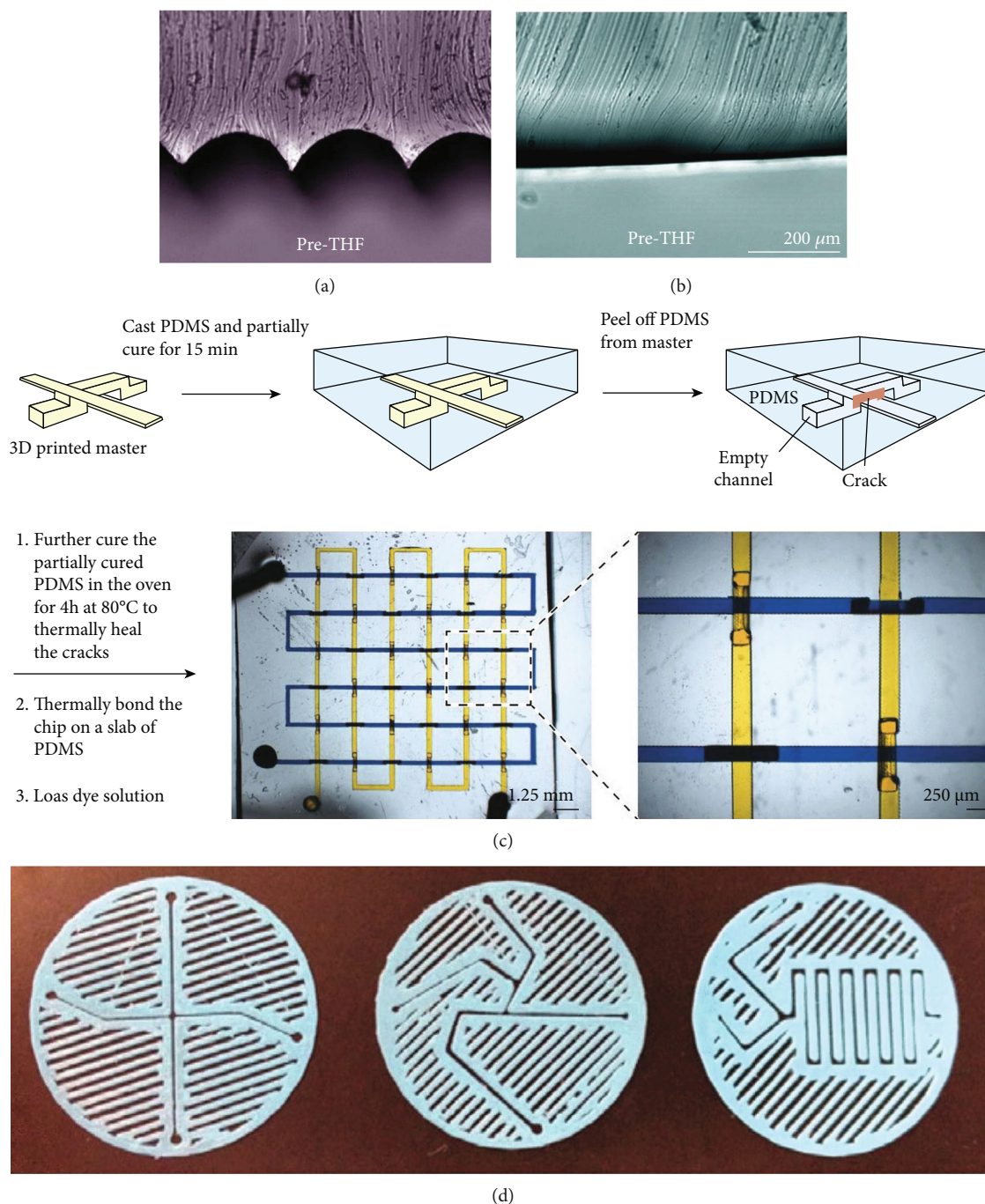


FIGURE 8: Template and surface of 3D-printed microfluidic devices. (a, b) Images showing the surface roughness of a polylactic acid fused deposition modeling (FDM) template before and after smoothing with tetrahydrofuran (THF) solvent. Panels adapted with permission from references [76, 77] (copyright 2016, Royal Society of Chemistry). (c) A method of casting a fully 3D device. Polydimethylsiloxane (PDMS) is cast over a 3D-printed template and allowed to partially cure. The PDMS is cracked and peeled off the template and then allowed to fully cure before filling with fluid for experiments. Adapted with permission from reference [78] (copyright 2015, Springer Nature). (d) Sandwich-style planar mixers are printed with FDM and then sandwiched between two surfaces with interface connections to form fluidic devices. Adapted with permission from reference [79] (copyright 2015, IOP Publishing) [80].

(iii) *Continuous liquid phase production*: in the continuous liquid phase production (CLIP) technique, product output can be obtained only with photopolymers in the material with microstereolithography. However, in μSL , there is a long production

time and a gradual interface between each printing layer. However, with the developing technology, the “continuous liquid phase production” defined as “CLIP” has completely eliminated the problems mentioned earlier. In this technique, microsized 3D

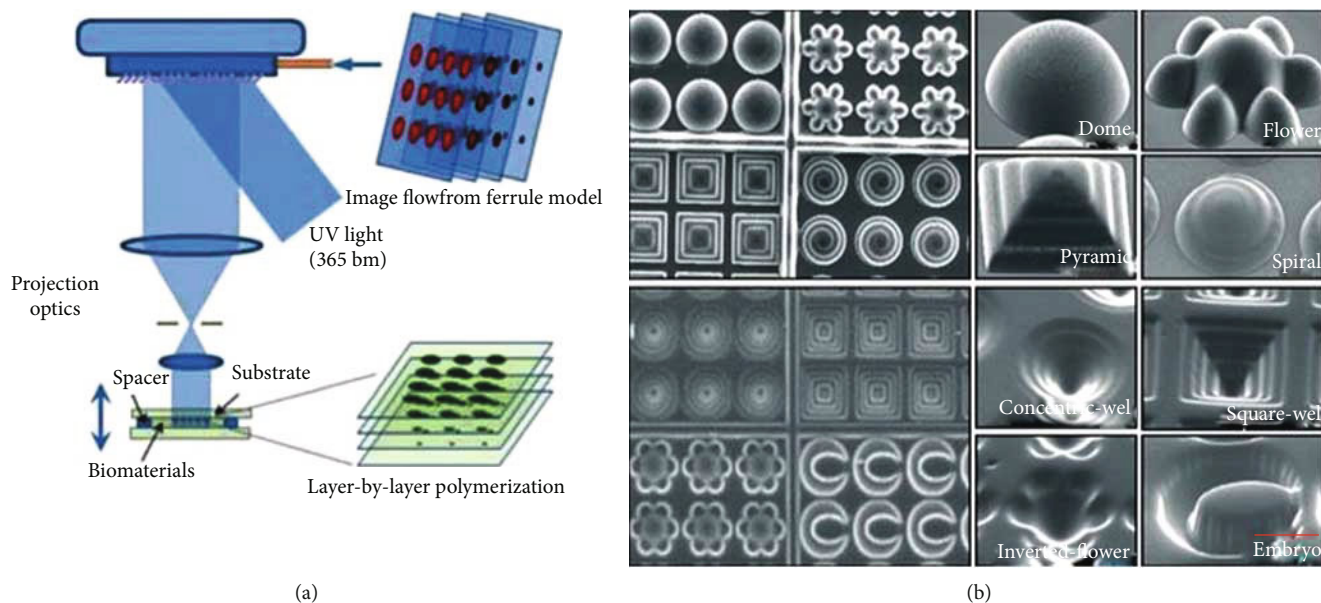


FIGURE 9: (a) Projection microstereolithography ($P\mu$ SL) setup: UV-light projects to the DMD mirror, which produces an optical pattern. The optical pattern projects across an optical lens to the photosensitive biomaterial to construct a 3D scaffold in a layer-by-layer method. (b) SEM images of the variety of printed microwells [83, 84].

mesoshapes without layers can be used at high speed and with vertical extrusion. The most striking feature of this technique is the provision of abundant oxygen permeability in terms of oxygen, which prevents photopolymerization. That is, in this technique, there is a continuous homogeneous production [68, 87]. In addition, product outputs of elastic ceramics and biological materials can be obtained with this technology. Prototyping and mass production may also be preferred in large-width MEMS devices [68]

In general, 3D printing techniques are implemented to fabricate microfluidic channels that are designed in different shapes and sizes [22]. The designs are fabricated to analyse the performance of the 3D printer which was then found to be able to print structures with at least $50\ \mu\text{m}$ dimensions [22]. In this study, two different production methods were developed to optically improve the produced 3D structures. Those are the 3D structures being bonded to glass surfaces with polydimethylsiloxane (PDMS) and clear resin interlayers. The adhesion between the glass surface and the 3D structures was achieved with UV application for the resin and through the use of elevated temperature for PDMS. For different thicknesses of PDMS and resin interlayers, the bonding strength of the produced channels is commonly examined. Bright-field and fluorescence imaging properties of these channels are also usually analysed. As a result, twice the bond strength and comparable viewing capacity, compared to the PDMS-glass surface adhesion and compared to conventional plasma, can be achieved. In addition, using the presented production method, 3D structures are able to integrate protein-coated glass surfaces without disrupting the protein's functionality.

2.5. Powder Bed Fusion (Additive Laser Technique). Powder bed fusion refers to an additive manufacturing process in which a laser (thermal energy) selectively fuses regions of a powder bed. In this process, generally no support is required for the creation of the section. To produce microfluidic chips, different types of powder bed fusion are currently being used. Laser microsintering (LMS), for instance, is a powder metallurgy technique developed by Deckard and Beaman to make cast models from plastic powder. Its origin dates back to the 1980s, and it is called selective laser sintering (SLS) [88, 89]. In the working system, powder groups consisting of metal powders in a bed are melted or sintered by a laser beam. This process is a powder welding process to make a solid part or attachment to a previously determined computer-generated 3D model [90]. Most of the powders used in this technique are metals (Ag, Al, Cu, and stainless steels) or polymers in addition to some ceramics which can be processed using this technique [88].

Bohandy et al. [91] developed a matrix-assisted pulsed laser evaporation technique, which is a derivative of laser-containing advanced transfer (LIFT), in 1986. This technique is used to create layers in one plane directly using the laser. It consists of a receiver and a transmitter. The donor material is transparent, and a thin-film method such as coating and spraying is used. In the data layer, it has two important features that can absorb the preferred wavelength and ensure a rapid supply of sufficient material in the case of continuous pressure [92, 93]. Metals such as chromium, tungsten, gold, nickel, aluminium, copper, and vanadium, which are found in many different types, can be plated [94–96].

Laser chemical vapor coating (LCVD) is used in the production of complex parts, which can coat many different types of materials. The LCVD process is generally created in a vacuum chamber with the separation of the by-product

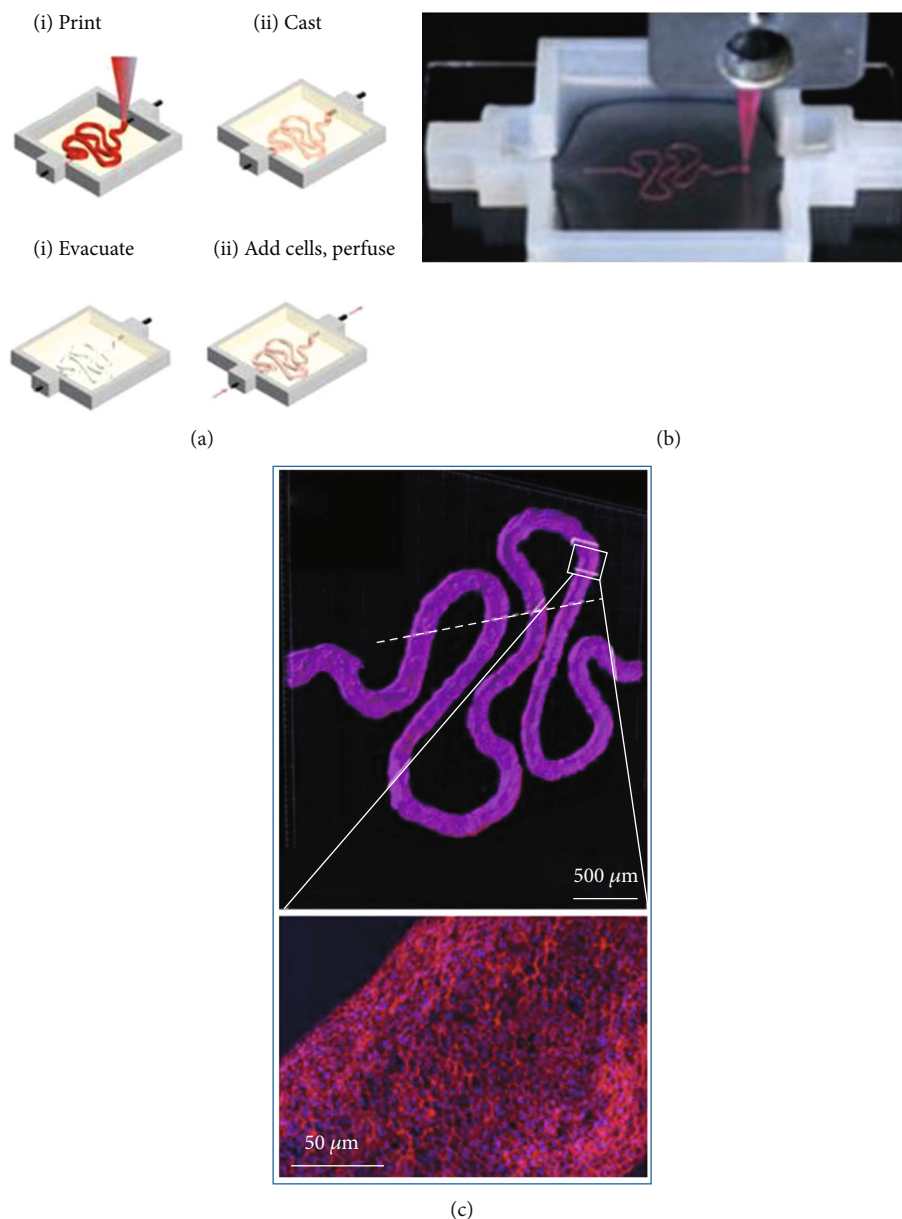


FIGURE 10: 3D-printed organs on chips in an ink-based printer technique: (a) illustration and (b) photograph of the extrusion-printing process of a kidney proximal tubule on a chip. (c) An immunofluorescent stained image of the inkjet-printed tubule [84].

that a precursor gas accumulates on the structure by laser beam during scanning. There are two laser-assisted groups that are divided into pyrolytic LCVD and photolytic LCVD. The process in which the precursor gas is thermally decomposed by laser heat on the layer is called the pyrolytic LCVD process while the process by which photon energy is absorbed by the precursor gas is called the photolytic LCVD process [97] which is commonly used for the metal deposition process, carbonyl, alkyl, halogen, oxyhalite, etc. while precursor gases are preferred; alkyls or alkyl halogens are generally preferred for semiconductors [98–102].

2.6. Material Jetting (Ink-Based 3D Printing and Extrusion). Extrusion-based and material jetting 3D printing refers to a

series of 3D printers that utilize a nozzle to directly print molten materials from a constant cross-sectional diameter nozzle. In this process, the molten material is liquified and bonds with the previously printed layers and sections. In this process, photomonomers, in solution with nanoparticles in colloidal suspension, and inks, which can be found in several different types in organic or inorganic solvents, containing metallic and nonmetallic components are selectively deposited. This process can further be divided into the following [103]:

- (i) Direct part printing: this includes printing sections with photopolymers and waxes by directly printing the parts

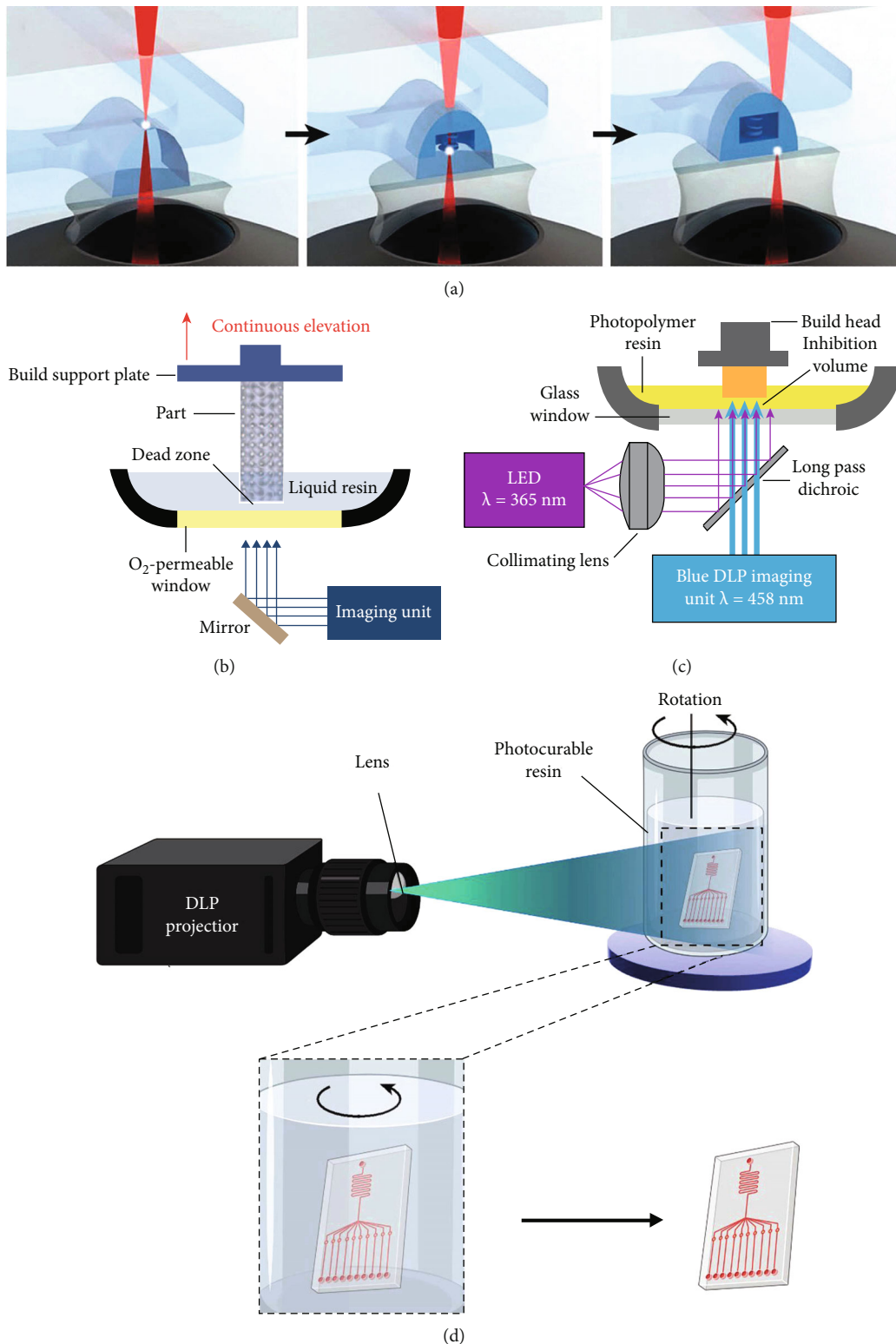


FIGURE 11: New approaches for 3D printing of microfluidic devices and structures. (a) Two-photon polymerization of a spring diode inside a microfluidic channel. Adapted with permission from reference [107]. (b) Instrumentation setup for CLIP. The build platform is continuously raised out of a resin vat, and polymerization is enabled by an oxygen-inhibited dead zone above a permeable window. Adapted from reference [76] (copyright 2015, AAAS). (c) Instrumental setup for an alternate approach to CLIP. Polymerization is initiated by blue light and inhibited by UV light. Adapted with permission from reference [77]. (d) Image angle breakdown and instrumental setup for CAL 3D printing. Abbreviations: CAL: computed axial lithography; CLIP: continuous liquid interface printing; DLP: digital light processing [79, 80].

- (ii) Binder printing: this technique refers to a rather broad class of processes whereby the binder is printed onto powder bed

To manufacture microfluidic chips and devices by using this technique, generally the direct part printing is utilized.

An application of the ink-based printer technique is shown in Figures 10 and 11.

In this process, a thermal actuator or piezoelectric actuator is commonly used to allow ink droplets to contact a surface. In this section, ink droplets can be used as separate droplets from time to time (the drop-and-demand (DoD) method) or as a continuous inkjet (CIJ) method by recycling unused ink fluid. Since the control area for the material distributed in the DoD is larger, it is more suitable for microfabrication [104].

2.7. Other 3D Printing Techniques. Other 3D printing techniques include Multi Jet technology which combines inkjet and stereolithography 3D printing methods. A multi-ink-based model is created by spraying photopolymer resins on a layered structure. PolyJet materials harden as a result of being exposed to UV rays for a short time, and the product is formed after stratification. Multi-Jet technology enables the production of especially smoother, more precise, and higher resolution products.

In addition, hybrid products can be produced by mixing plastic, flexible, and transparent material derivatives in 3D printing [105, 106].

Nowadays, it is easy to print 3D products between 70 and 200 microns with Multi Jet and FDM technologies. This scale is not very suitable for MEMS devices.

3. Conclusions and Future Perspective

Microfluidic chips and devices are able to downscale biochemical and biomedical processes to a portable micro- and nanosized scale. Such engineered devices allow a better control over fluid flow and provide microenvironmental control over variables that can have major uses in autonomous applications. As a result of its numerous contributions, in this review study, the manufacturing technologies used in the design and manufacture of micro- and nanoscale sensors and their subcomponents were examined. According to the results of the experimental studies, the following inferences have been made:

- (i) Options in production technologies include changes according to the working and measuring features of the designed sensor. There is an increasing tendency to use the FDM method in the selection of the production method. However, it is related to the properties desired to be produced by chemical or physical interaction
- (ii) The sensors to be produced have morphological features that can be used in every field from biomedical to aviation. However, product expectations may not be sufficient for uniform material composition. Printers that are hybrid and can produce different

types of materials (metal-ceramic-polymer) should be used in expanding the product range. The selection of production methods varies in the characteristics of the sensor to be produced

- (iii) The choice of matrix material in the production of composite, coating, and other production methods causes all properties to change

Conflicts of Interest

The authors declare that there is no conflict of interest regarding the publication of this paper.

References

- [1] G. Weisgrab, A. Ovsianikov, and P. F. Costa, "Functional 3D printing for microfluidic chips," *Advanced Materials Technologies*, vol. 4, no. 10, p. 1900275, 2019.
- [2] J. Qiu, Q. Gao, H. Zhao, J. Fu, and Y. He, "Rapid customization of 3D integrated microfluidic chips via modular structure-based design," *ACS Biomaterials Science & Engineering*, vol. 3, no. 10, pp. 2606–2616, 2017.
- [3] A. K. Au, N. Bhattacharjee, L. F. Horowitz, T. C. Chang, and A. Folch, "3D-printed microfluidic automation," *Lab on a Chip*, vol. 15, no. 8, pp. 1934–1941, 2015.
- [4] K. S. Teh, "Additive direct-write microfabrication for MEMS: a review," *Frontiers of Mechanical Engineering*, vol. 12, no. 4, pp. 490–509, 2017.
- [5] C. Acar, A. R. Schofield, A. A. Trusov, L. E. Costlow, and A. M. Shkel, "Environmentally robust MEMS vibratory gyroscopes for automotive applications," *IEEE Sensors Journal*, vol. 9, no. 12, pp. 1895–1906, 2009.
- [6] D. S. Eddy and D. R. Sparks, "Application of MEMS technology in automotive sensors and actuators," *Proceedings of the IEEE*, vol. 86, no. 8, pp. 1747–1755, 1998.
- [7] B. P. Gogoi and D. Mladenovic, "Integration technology for MEMS automotive sensors," in *IEEE 2002 28th Annual Conference of the Industrial Electronics Society. IECON 02*, Seville, Spain, 2002.
- [8] A. Ostendorf and B. N. Chichkov, "Two-photon polymerization: a new approach to micromachining," *Photonics Spectra*, vol. 40, no. 72-undefined, 2006.
- [9] D. Panescu, "MEMS in medicine and biology," *IEEE Engineering in Medicine and Biology Magazine*, vol. 25, no. 5, pp. 19–28, 2006.
- [10] D. L. Polla, A. G. Erdman, W. P. Robbins et al., "Microdevices in medicine," *Annual Review of Biomedical Engineering*, vol. 2, no. 1, pp. 551–576, 2000.
- [11] A. I. Tsung Pan, *Monolithic thermal ink jet printhead with integral nozzle and ink feed*, 1987.
- [12] K. Silverbrook, *Ink jet print device and print head or print apparatus using the same*, 2000.
- [13] C. Hagleitner, A. Hierlemann, D. Lange et al., "Smart single-chip gas sensor microsystem," *Nature*, vol. 414, no. 6861, pp. 293–296, 2001.
- [14] Q. Wan, Q. H. Li, Y. J. Chen et al., "Fabrication and ethanol sensing characteristics of ZnO nanowire gas sensors," *Applied Physics Letters*, vol. 84, no. 18, pp. 3654–3656, 2004.
- [15] T. Waqar and S. Ersoy, "Design and analysis comparison of surface acoustic wave-based sensors for fabrication using

- additive manufacturing,” *Journal of Nanomaterials*, vol. 2021, Article ID 5598347, 12 pages, 2021.
- [16] Shi-Sheng Lee, Long-Sun Huang, Chang-Jin Kim, and M. C. Wu, “Free-space fiber-optic switches based on MEMS vertical torsion mirrors,” *Journal of Lightwave Technology*, vol. 17, no. 1, pp. 7–13, 1999.
- [17] D. M. Marom, D. T. Neilson, D. S. Greywall et al., “Wavelength-selective 1/spl times/K switches using free-space optics and MEMS micromirrors: theory, design, and implementation,” *Journal of Lightwave Technology*, vol. 23, no. 4, pp. 1620–1630, 2005.
- [18] P. F. van Kessel, L. J. Hornbeck, R. E. Meier, and M. R. Douglass, “A MEMS-based projection display,” *Proceedings of the IEEE*, vol. 86, no. 8, pp. 1687–1704, 1998.
- [19] J. M. Bustillo, R. T. Howe, and R. S. Muller, “Surface micromachining for microelectromechanical systems,” *Proceedings of the IEEE*, vol. 86, no. 8, pp. 1552–1574, 1998.
- [20] M. Hoffmann and E. Voges, “Bulk silicon micromachining for MEMS in optical communication systems,” *Journal of Micromechanics and Microengineering*, vol. 12, no. 4, pp. 349–360, 2002.
- [21] J. Hormes, J. Göttert, K. Lian, Y. Desta, and L. Jian, “Materials for LiGA and LiGA-based microsystems,” *Nuclear Instruments and Methods in Physics Research Section B: Beam Interactions with Materials and Atoms*, vol. 199, pp. 332–341, 2003.
- [22] S. Keçili, *Fabrication of microfluidic devices via 3D printer*, 2019.
- [23] Y. Li, Y. Fang, J. Wang et al., “Integrative optofluidic microcavity with tubular channels and coupled waveguides via two-photon polymerization,” *Lab on a Chip*, vol. 16, no. 22, pp. 4406–4414, 2016.
- [24] I. Unalli, S. Ersoy, and I. Ertugrul, “Microfluidics chip design analysis and control,” *Journal of Mechatronics and Artificial Intelligence in Engineering*, vol. 1, no. 1, pp. 2–7, 2020.
- [25] G. Nelson, R. A. Kirian, U. Weierstall et al., “Three-dimensional-printed gas dynamic virtual nozzles for x-ray laser sample delivery,” *Optics Express*, vol. 24, no. 11, pp. 11515–11530, 2016.
- [26] I. Ertugrul and T. Waqar, “Fabrication of bidirectional electrothermal microactuator by two-photon polymerization,” *Current Nanoscience*, vol. 16, 2020.
- [27] C. Peters, M. Hoop, S. Pané, B. J. Nelson, and C. Hierold, “Degradable magnetic composites for minimally invasive interventions: device fabrication, targeted drug delivery, and cytotoxicity tests,” *Advanced Materials*, vol. 28, no. 3, pp. 533–538, 2016.
- [28] U. T. Sanli, H. Ceylan, I. Bykova et al., “3D nanoprinted plastic kinoform X-ray optics,” *Advanced Materials*, vol. 30, no. 36, 2018.
- [29] K. S. Worthington, L. A. Wiley, E. E. Kaalberg et al., “Two-photon polymerization for production of human iPSC-derived retinal cell grafts,” *Acta Biomaterialia*, vol. 55, pp. 385–395, 2017.
- [30] C. A. Lissandrello, W. F. Gillis, J. Shen et al., “A micro-scale printable nanoclip for electrical stimulation and recording in small nerves,” *Journal of Neural Engineering*, vol. 14, no. 3, p. 036006, 2017.
- [31] M. Suzuki, T. Takahashi, and S. Aoyagi, “3D laser lithographic fabrication of hollow microneedle mimicking mosquitos and its characterisation,” *International Journal of Nanotechnology*, vol. 15, no. 1/2/3, p. 157, 2018.
- [32] R. Amin, S. Knowlton, A. Hart et al., “3D-printed microfluidic devices,” *Biofabrication*, vol. 8, no. 2, 2016.
- [33] S. Knowlton, C. H. Yu, F. Ersoy, S. Emadi, A. Khademhosseini, and S. Tasoglu, “3D-printed microfluidic chips with patterned, cell-laden hydrogel constructs,” *Biofabrication*, vol. 8, no. 2, article 025019, 2016.
- [34] C. M. B. Ho, S. H. Ng, K. H. H. Li, and Y. J. Yoon, “3D printed microfluidics for biological applications,” *Lab on a Chip*, vol. 15, no. 18, pp. 3627–3637, 2015.
- [35] A. Dellaquila, *Five short stories on the history of microfluidics*, 2017.
- [36] N.-T. Nguyen and S. Wereley, *Fundamentals and Applications of Microfluidics*, Artech, 2006.
- [37] M. F. Hochella, “There’s plenty of room at the bottom: nanoscience in geochemistry,” *Geochimica et Cosmochimica Acta*, vol. 66, no. 5, pp. 735–743, 2002.
- [38] R. P. Feynman, “There’s plenty of room at the bottom [data storage],” *Journal of Microelectromechanical Systems*, vol. 1, no. 1, pp. 60–66, 1992.
- [39] G. M. Whitesides, “The origins and the future of microfluidics,” *Nature*, vol. 442, no. 7101, pp. 368–373, 2006.
- [40] A. R. Abate, P. Mary, V. van Steijn, and D. A. Weitz, “Experimental validation of plugging during drop formation in a T-junction,” *Lab on a Chip*, vol. 12, no. 8, pp. 1516–1521, 2012.
- [41] R.-L. Chien and W. J. Parce, “Multiport flow-control system for lab-on-a-chip microfluidic devices,” *Fresenius’ Journal of Analytical Chemistry*, vol. 371, no. 2, pp. 106–111, 2001.
- [42] J.-H. Lue, Y. S. Su, and T. C. Kuo, “Workshop, cost-effective and streamlined fabrications of re-usable world-to-chip connectors for handling sample of limited volume and for assembling chip array,” *Sensors*, vol. 18, no. 12, p. 4223, 2018.
- [43] J. Zhong, *Nanofluidics: a window into transport and phase change in nanoporous systems*, [Ph.D. thesis], University of Toronto, Canada, 2019.
- [44] A. Folch and M. Toner, “Cellular micropatterns on biocompatible materials,” *Biotechnology Progress*, vol. 14, no. 3, pp. 388–392, 1998.
- [45] L. Shang, Y. Cheng, and Y. Zhao, “Emerging droplet microfluidics,” *Chemical Reviews*, vol. 117, no. 12, pp. 7964–8040, 2017.
- [46] Y. Whulanza, D. S. Widyaratih, J. Istiyanto, and G. Kiswanto, “Realization and testing of lab-on-chip for human lung replication,” *ARNP Journal of Engineering and Applied Sciences*, vol. 9, pp. 2064–2067, 2014.
- [47] A. M. Ghaemmaghami, M. J. Hancock, H. Harrington, H. Kaji, and A. Khademhosseini, “Biomimetic tissues on a chip for drug discovery,” *Drug Discovery Today*, vol. 17, no. 3-4, pp. 173–181, 2012.
- [48] D. Huh, B. D. Matthews, A. Mammoto, M. Montoya-Zavala, H. Y. Hsin, and D. E. Ingber, “Reconstituting organ-level lung functions on a chip,” *Science*, vol. 328, no. 5986, pp. 1662–1668, 2010.
- [49] A. Williamson, S. Singh, U. Fernekorn, and A. Schober, “The future of the patient-specific body-on-a-chip,” *Lab on a Chip*, vol. 13, no. 18, pp. 3471–3480, 2013.
- [50] C. Moraes, J. M. Labuz, B. M. Leung, M. Inoue, T. H. Chun, and S. Takayama, “On being the right size: scaling effects in designing a human-on-a-chip,” *Integrative Biology*, vol. 5, no. 9, pp. 1149–1161, 2013.

- [51] E. W. Esch, A. Bahinski, and D. Huh, "Organs-on-chips at the frontiers of drug discovery," *Nature Reviews Drug Discovery*, vol. 14, no. 4, pp. 248–260, 2015.
- [52] R. Vitorino, S. Guedes, J. P. da Costa, and V. Kašička, "Microfluidics for peptidomics, proteomics, and cell analysis," *Nanomaterials*, vol. 11, no. 5, p. 1118, 2021.
- [53] W. Lee, P. Tseng, and D. di Carlo, *Microfluidic cell sorting and separation technology*, 2017.
- [54] D. Gao, C. Song, and J.-M. Lin, *Microfluidics-mass spectrometry combination systems for single-cell analysis*, 2019.
- [55] R. Bogue, "MEMS sensors: past, present and future," *Sensor Review*, vol. 27, no. 1, pp. 7–13, 2007.
- [56] J. W. Judy, "Microelectromechanical systems (MEMS): fabrication, design and applications," *Smart Materials and Structures*, vol. 10, no. 6, pp. 1115–1134, 2001.
- [57] P. Pal and K. Sato, "Fabrication methods based on wet etching process for the realization of silicon MEMS structures with new shapes," *Microsystem Technologies*, vol. 16, no. 7, pp. 1165–1174, 2010.
- [58] C. Iliescu and F. E. H. Tay, "Wet etching of glass," in *CAS 2005 Proceedings. 2005 International Semiconductor Conference, 2005*, Sinaia, Romania, October 2005.
- [59] S. Ronggui and G. C. Righini, "Characterization of reactive ion etching of glass and its applications in integrated optics," *Journal of Vacuum Science & Technology A: Vacuum, Surfaces, and Films*, vol. 9, no. 5, pp. 2709–2712, 1991.
- [60] Hayashi Pure Chemical Ind, *High performance anisotropic Si etchant in wet process*, 2008.
- [61] J. Albero, L. Nieradko, C. Gorecki et al., "Fabrication of spherical microlenses by a combination of isotropic wet etching of silicon and molding techniques," *Optics Express*, vol. 17, no. 8, pp. 6283–6292, 2009.
- [62] M. Leester-Schädel, T. Lorenz, F. Jürgens, and C. Richter, "Fabrication of microfluidic devices," in *Microsystems for Pharmatechnology*, Springer International Publishing, 2016.
- [63] J. J. Allen, *Introduction to MEMS (MicroElectroMechanical Systems)*, 2007.
- [64] V. K. Varadan, X. Jiang, and V. Varadan, *Microstereolithography and other Fabrication Techniques for 3D MEMS*, Wiley, 2001.
- [65] M. J. Madou, *Fundamentals of Microfabrication*, CRC Press, 2018.
- [66] D. Holbrook, "Controlling contamination: the origins of clean room technology," *History and Technology*, vol. 25, no. 3, pp. 173–191, 2009.
- [67] J. Castillo-León, "Microfluidics and lab-on-a-chip devices: history and challenges," in *Lab-on-a-Chip Devices and Micro-Total Analysis Systems*, Springer International Publishing, 2015.
- [68] W. J. Whitfield, *Ultra-Clean Room*, 1964.
- [69] W. Whyte, "An introduction to the design of clean and containment areas," in *Cleanroom Design* John Wiley & Sons, Ltd.
- [70] T. Sandle, "Application of quality risk management to set viable environmental monitoring frequencies in biotechnology processing and support areas," *PDA Journal of Pharmaceutical Science and Technology*, vol. 66, no. 6, pp. 560–579, 2012.
- [71] W. Whyte, *Cleanroom Technology: Fundamentals of Design, Testing and Operation*, John Wiley & Sons, 2010.
- [72] Y. Lamkharbach, F. Bazi, L. Haji, L. Bennani, A. Mourran, and M. L. Bouamrani, "Study of changing statistics model's influence on the exploitation and conformity of results in the new standard version ISO 14644 part 1," *Periodicals of Engineering and Natural Sciences (PEN)*, vol. 6, no. 2, 2018.
- [73] D. Khorsandi, A. Fahimipour, P. Abasian et al., "3D and 4D printing in dentistry and maxillofacial surgery: printing techniques, materials, and applications," *Acta Biomaterialia*, vol. 122, pp. 26–49, 2021.
- [74] A. K. Miri, E. Mostafavi, D. Khorsandi, S. K. Hu, M. Malpica, and A. Khademhosseini, "Bioprinters for organs-on-chips," *Biofabrication*, vol. 11, no. 4, p. 042002, 2019.
- [75] S. N. Economidou and D. Douroumis, "3D printing as a transformative tool for microneedle systems: Recent advances, manufacturing considerations and market potential," *Advanced Drug Delivery Reviews*, vol. 173, pp. 60–69, 2021.
- [76] J. R. Tumbleston, D. Shrivanyants, N. Ermoshkin et al., "Continuous liquid interface production of 3D objects," *Science*, vol. 347, no. 6228, pp. 1349–1352, 2015.
- [77] J. C. Brooks, K. I. Ford, D. H. Holder, M. D. Holtan, and C. J. Easley, "Macro-to-micro interfacing to microfluidic channels using 3D-printed templates: application to time-resolved secretion sampling of endocrine tissue," *The Analyst*, vol. 141, no. 20, pp. 5714–5721, 2016.
- [78] M. P. de Beer, H. L. van der Laan, M. A. Cole, R. J. Whelan, M. A. Burns, and T. F. Scott, "Rapid, continuous additive manufacturing by volumetric polymerization inhibition patterning," *Science Advances*, vol. 5, no. 1, p. eaau8723, 2019.
- [79] B. E. Kelly, I. Bhattacharya, H. Heidari, M. Shusteff, C. M. Spadaccini, and H. K. Taylor, "Volumetric additive manufacturing via tomographic reconstruction," *Science*, vol. 363, no. 6431, pp. 1075–1079, 2019.
- [80] A. V. Nielsen, M. J. Beauchamp, G. P. Nordin, and A. T. Woolley, "3D printed microfluidics," *Annual Review of Analytical Chemistry*, vol. 13, no. 1, pp. 45–65, 2020.
- [81] C. M. Spadaccini, G. Farquar, T. Weisgraber et al., *High resolution projection micro stereolithography system and method.*, 2016.
- [82] D. Khorsandi, S. Palacios, Y. Gaslain et al., "P159 Human uterine cervix-on-a-chip: establishing the first in vitro model to study the development of cervical carcinoma and human papilloma virus mechanism of action," in *Poster Exhibition Day 2*, BMJ Publishing Group Ltd, 2019.
- [83] K. C. Hribar, P. Soman, J. Warner, P. Chung, and S. Chen, "Light-assisted direct-write of 3D functional biomaterials," *Lab on a Chip*, vol. 14, no. 2, pp. 268–275, 2014.
- [84] K. A. Homan, D. B. Kolesky, M. A. Skylar-Scott et al., "Bioprinting of 3D convoluted renal proximal tubules on Perfusable chips," *Scientific Reports*, vol. 6, no. 1, 2016.
- [85] S. Wu, J. Serbin, and M. Gu, "Two-photon polymerisation for three-dimensional micro-fabrication," *Journal of Photochemistry and Photobiology A: Chemistry*, vol. 181, no. 1, pp. 1–11, 2006.
- [86] H. Petek, M. J. Weida, H. Nagano, and S. Ogawa, "Real-time observation of adsorbate atom motion above a metal surface," *Science*, vol. 288, no. 5470, pp. 1402–1404, 2000.
- [87] S. Maruo, K. Ikuta, and H. Korogi, "Force-controllable, optically driven micromachines fabricated by single-step two-photon microstereolithography," *Journal of Microelectromechanical Systems*, vol. 12, no. 5, pp. 533–539, 2003.

- [88] F. Abe, "The manufacturing of hard tools from metallic powders by selective laser melting," *Journal of Materials Processing Technology*, vol. 111, no. 1-3, pp. 210–213, 2001.
- [89] H. Exner and A. Streek, *High resolution laser micro sintering / melting using q-switched and high brilliant laser radiation*, H. Helvajian, A. Piqué, M. Wegener, and B. Gu, Eds., 2015.
- [90] T. Petsch, P. Regenfuss, R. Ebert et al., "Industrial laser micro sintering," in *International Congress on Applications of Lasers & Electro-Optics*, Laser Institute of America, 2004.
- [91] J. Bohandy, B. F. Kim, and F. J. Adrian, "Metal deposition from a supported metal film using an excimer laser," *Journal of Applied Physics*, vol. 60, no. 4, pp. 1538–1539, 1986.
- [92] S. Papazoglou and I. Zergioti, "Laser induced forward transfer (LIFT) of nano-micro patterns for sensor applications," *Microelectronic Engineering*, vol. 182, pp. 25–34, 2017.
- [93] W. A. Tolbert, I.-Y. S. Lee, M. M. Doxtader, E. W. Ellis, and D. D. Dlott, "High-speed color imaging by laser ablation transfer with a dynamic release layer: fundamental mechanisms," *Journal of Imaging Science*, vol. 37, pp. 411–421, 1993.
- [94] D. B. Chrisey, A. Pique, J. Fitz-Gerald et al., "New approach to laser direct writing active and passive mesoscopic circuit elements," *Applied Surface Science*, vol. 154–155, pp. 593–600, 2000.
- [95] A. Piqué and B. C. Douglas, *Direct-Write Technologies for Rapid Prototyping Applications: Sensors, Electronics, and Integrated Power Sources*, 2001.
- [96] C. W. Visser, R. Pohl, C. Sun, G. W. Römer, B. Huis in 't Veld, and D. Lohse, "Toward 3D printing of pure metals by laser-induced forward transfer," *Advanced Materials*, vol. 27, no. 27, pp. 4087–4092, 2015.
- [97] H. Alemohammad and E. Toyserkani, "Laser-assisted additive fabrication of micro-sized coatings," in *Advances in Laser Materials Processing*, Elsevier, 2010.
- [98] A. Piqué, H. Kim, R. C. Y. Auyeung, and A. T. Smith, "Laser forward transfer of functional materials for digital fabrication of microelectronics," *Journal of Imaging Science and Technology*, vol. 57, no. 4, pp. 1–8, 2013.
- [99] A. J. Birnbaum, H. Kim, N. A. Charipar, and A. Piqué, "Laser printing of multi-layered polymer/metal heterostructures for electronic and MEMS devices," *Applied Physics A*, vol. 99, no. 4, pp. 711–716, 2010.
- [100] R. C. Y. Auyeung, H. Kim, A. J. Birnbaum, M. Zhalutdinov, S. A. Mathews, and A. Piqué, "Laser decal transfer of free-standing microcantilevers and microbridges," *Applied Physics A*, vol. 97, no. 3, pp. 513–519, 2009.
- [101] C. Duty, D. Jean, and W. J. Lackey, "Laser chemical vapour deposition: materials, modelling, and process control," *International Materials Reviews*, vol. 46, no. 6, pp. 271–287, 2001.
- [102] M. C. Wanke, O. Lehmann, K. Muller, Q. Wen, and M. Stuke, "Laser rapid prototyping of photonic band-gap microstructures," *Science*, vol. 275, no. 5304, pp. 1284–1286, 1997.
- [103] I. Gibson, D. Rosen, and B. Stucker, "Additive manufacturing technologies: 3D printing, rapid prototyping, and direct digital manufacturing, second edition," in *Additive Manufacturing Technologies: 3D Printing, Rapid Prototyping, and Direct Digital Manufacturing, Second Edition*, pp. 1–498, 2015.
- [104] J. Lessing, A. C. Glavan, S. B. Walker, C. Keplinger, J. A. Lewis, and G. M. Whitesides, "Inkjet printing of conductive inks with high lateral resolution on omniphobic "R^F paper" for paper-based electronics and MEMS," *Advanced Materials*, vol. 26, no. 27, pp. 4677–4682, 2014.
- [105] V. Tagliaferri, F. Trovalusci, S. Guarino, and S. Venettacci, "Environmental and economic analysis of FDM, SLS and MJF Additive Manufacturing Technologies," *Materials*, vol. 12, no. 24, p. 4161, 2019.
- [106] J. A. Wittkopf, K. Erickson, P. Olumbummo, A. Hartman, H. Tom, and L. Zhao, "3D printed electronics with multi jet fusion," *NIP & Digital Fabrication Conference*, vol. 2019, no. 1, pp. 29–33, 2019.
- [107] A. C. Lamont, A. T. Alsharhan, and R. D. Sochol, "Geometric Determinants of *In-Situ* Direct Laser Writing," *Scientific Reports*, vol. 9, no. 1, p. 394, 2019.

Research Article

Design and Analysis Comparison of Surface Acoustic Wave-Based Sensors for Fabrication Using Additive Manufacturing

Tayyab Waqar  and Sezgin Ersoy 

Department of Mechatronics Engineering, Marmara University, Istanbul 34100, Turkey

Correspondence should be addressed to Tayyab Waqar; tayyabwaqar@gmail.com

Received 4 February 2021; Revised 23 May 2021; Accepted 29 May 2021; Published 14 June 2021

Academic Editor: Ibrahim Alarifi

Copyright © 2021 Tayyab Waqar and Sezgin Ersoy. This is an open access article distributed under the Creative Commons Attribution License, which permits unrestricted use, distribution, and reproduction in any medium, provided the original work is properly cited.

Sensors have become an integral part of our everyday lives by helping us converting packets of data to make important decisions. Due to this reason, researches are done constantly to improve the fabrication processes of sensors by making them more user-friendly, less time-consuming, and more cost-effective. The application of any fabrication solution that offers those advantages will have a major impact on the manufacturing of modern sensors. To address this issue, a 3D printed Surface Acoustic Wave (SAW) temperature sensor is presented in this paper. The modelling and analysis of such a sensor have been performed for both aluminium and copper electrodes using COMSOL software. In total, 4 different sensing structures, 2 each for both aluminium and copper electrodes based one-port resonators, are designed and analysed for their application in temperature sensing. The resulting responses of those sensors are approximately 2.19 MHz and 424.01 MHz frequency ranges. The novelty lies in the possibility of mass-producing such a sensor using additive manufacturing will have a direct impact in the areas where conventional electronics cannot be utilized.

1. Introduction

Sensor-based technologies are playing an enormous role in fostering social and economic-based advancements in emerging economies all over the globe. To support the necessary technological development in the field of printed electronics [1–3], hence, in the field of sensors, both the researchers [4] and the industries [5] are working in alignment. Research and development are done to cut down the costs [6] and the time [7] to mass-produce sensors that are directly related to the efficiency [8–10] of the production and carry a huge benefit for the industry and also to the end-user. One such technique which can help the advancements towards this common goal is known as 3D printing, and it is already being employed to produce parts for industries such as automotive with greater speed and accuracy. To facilitate the process of 3D printing for sensor manufacturing, ink-jet printing, a technology commonly used in both personal and commercial environments, has surfaced in preference to conventional

electronics fabrication practices [11–14]. Au et al. compared the cost of a traditionally manufactured sensor, i.e., via lithography, to a 3D printed technology, i.e., stereolithography and found the difference to be 15 USD [15]. Not only the cost but also the simplicity of the 3D printing technique plays an important role here as it makes the reproduction of the same structure with minimal human effort. In addition to that, the sensitivity and the accuracy of the printed sensor, compared to the traditional ways, are not affected [16, 17].

Several 3D printing technologies are being currently utilized and are also researched for their implementation in the sensor fabrication process, and one of them is based on Aerosol Jet (AJ) method which can directly print the required sensing structure on the provided substrate. AJ-based direct structure writing technique has been used for the realization of strain sensor [18–20], electrochemical and biosensors [21], antennas [22], electronic interconnect devices [23], transistors [24], solar cells [25, 26], electrothermal actuators [27], and

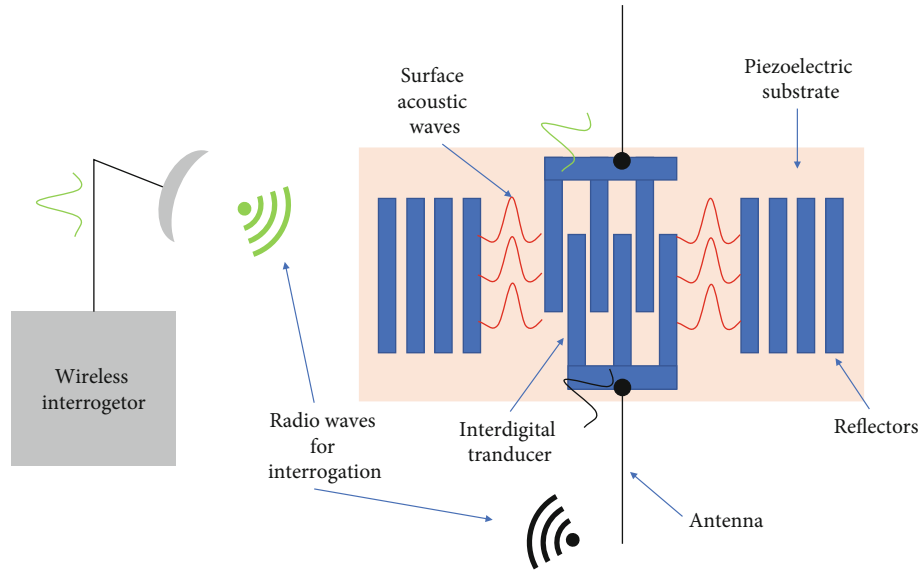


FIGURE 1: Operating principle of a one-port SAW-based resonator.

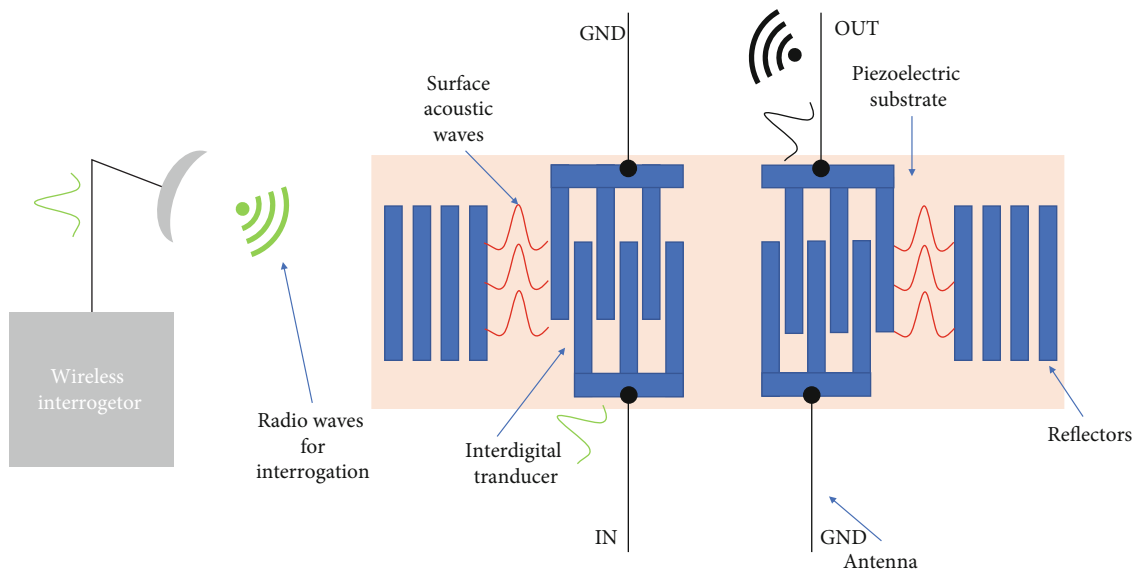


FIGURE 2: Operating principle of a two-port SAW-based resonator.

microbeams [28]. This work focuses on the use of the AJ-based printing method for the surface acoustic wave (SAW) based passive temperature sensor.

SAW-based devices use the principle of piezoelectric effect to convert an electrical signal to a mechanical wave, Rayleigh wave which is a transversal wave, which then propagates through the piezoelectric substrate to the other transducer which then changes it back to an electric signal. The properties of the Rayleigh wave and the principle of the piezoelectric effect need to be understood correctly for the application of them as a sensing device [29].

A radio wave is emitted using a wireless interrogation device which then energizes the SAW device using the opposite of the piezoelectric effect. The radio wave is transferred to

interdigital transducers (IDT) via an antenna. The IDT converts the received electrical signal to a transversal wave, Rayleigh wave, which then propagates along the piezoelectric substrate to form a resonator. This structure has a unique resonating frequency at each temperature, and once the structural parameters of the SAW resonator are known, it can be utilized as a temperature sensing structure [30]. The schematic diagram illustrating the principle of operation of a typical single port SAW resonator is shown in Figure 1. One port resonator has IDT placed in the middle with reflectors on its left and right. Reflectors are used for sending back the generated surface acoustic wave.

Another type of SAW resonator is shown in Figure 2 which is known as the two-port SAW resonator. Due to its

structure, it is mostly used for higher frequency oscillators and narrowband filters.

SAW-based sensors can provide medical [31], telecommunication [32], consumer electronics [33, 34], automotive [31], and industrial [33] sectors with a wide range of use cases. Due to their passive sensing capabilities, SAW devices can be utilized in harsh operating conditions where normal electronic circuits cannot be used, i.e., high temperatures. Normally, SAW-based sensors are fabricated using traditional methods which requires a clean room facility and the obligation to follow complicated several step processes [35] using lithography [36] but the advancements in the 3D printing technologies have allowed the researchers to apply them to sensor fabrication process. These technologies can directly print nanoparticles onto the substrate to fabricate a sensing structure. They decrease the process steps and allow the efficient use of the materials as compared to traditional lithography [37–40].

For this work, the AJ-based stereolithography printing method will be of the focus. This printing method will be explored for the fabrication of a SAW-based temperature sensor. The development of such a sensor is very much in line with the current requirements of many industries [41–45].

This paper presents 4 different designs of SAW-based sensors, to be employed for temperature sensing, based on YZ-cut lithium niobate with either aluminium or copper as the electrodes. The sensing structures are designed using both aluminium and copper electrode-based one-port resonator-based techniques. The models of the aforementioned sensors are mathematically designed, and analyses are performed using COMSOL software. Frequency and voltage-based responses of the sensing structures for all 4 proposed models are also calculated using COMSOL. The novelty lies in the possibility of mass-producing such a sensor using additive manufacturing will have a direct impact in the areas where conventional electronics cannot be utilized.

2. Materials and Methods

2.1. Material Selection. One of the most important steps in designing a SAW-based sensing device is the selection of the substrate and subsequently the electrode materials. Thermal coefficient, wave type, wave propagation velocity, and electromechanical coupling factor (K^2) are some of the properties of the piezoelectric substrate which need to be considered for a SAW-based temperature sensor [46]. These properties are shown in Table 1 for some of the commonly used piezoelectric substrates.

For the design of a SAW-based temperature, the substrate with a higher thermal coefficient should be preferred due to the fact that it is directly related to the changes in the pitch of an IDT as a function of temperature. The change in length along the surface of the piezoelectric substrate will also affect the distance between the IDT electrodes, therefore, affecting the pitch of the device and since synchronous frequency and pitch are related, as in equation (1), therefore, the output signal will show a frequency shift. Depending on the mode of operation of the sensor, this frequency shift can be measured as either a shift in phase or a delay in time.

TABLE 1: Mechanical properties of some commonly available piezoelectric substrates.

Material	Orientation	Thermal coefficient ($10^{-6}/^{\circ}\text{C}$)	SAW velocity (m/s)	Coupling coefficient (%)
Lithium niobate	Y, Z	94	3488	4.6
Lithium niobate	128° -Y, X	75	3992	5.6
Lithium tantalate	Y, Z	35	3230	0.66
Lithium tantalate	X- 112° , Y	22.3	3295	0.75
Langasite	Y, X	38	2330	0.37
Quartz	Y, X	-24	3159	0
Quartz	Y ST, X	0	3159	0.16

TABLE 2: Properties of commonly used conductor material for IDTs.

IDT electrode conductor	Substrate adherence	Electrical resistivity ($\mu\Omega\text{-cm}$)	Melting point ($^{\circ}\text{C}$)
Gold	Poor	2.2	2855
Titanium	Good	50	3286
Tungsten	Normal	5	5554
Aluminium	Good	2.65	2518
Copper	Good	1.7	2926

To this end, looking at Table 1, lithium niobate should be preferred while quartz should be avoided for the application of SAW as a temperature sensor.

Another important thing to consider while designing a SAW sensing structure is the selection of the material for IDTs. Table 2 provides the properties of some of the most commonly used materials for IDTs [46]. YZ-cut lithium niobate will be used as a piezoelectric substrate with both aluminium and copper electrodes for IDT.

2.2. Sensor Design. Figure 3 describes the structural design parameters for the proposed SAW resonator-based temperature sensor. As depicted in Figure 3, the IDT structure is designed with a certain pitch among them, and the resulting surface acoustic wave is well-founded when the pitch of the IDT fingers and the wavelength of the surface wave are equal to each other. Equation (1) is employed to determine the resonant frequency (f), which is a function used for measuring temperature, of the proposed structure, and its relation to the propagation velocity (V_s) of the resulting surface wave.

$$f = \frac{V_s}{\lambda_0}, \quad (1)$$

where λ_0 is the wavelength of the SAW.

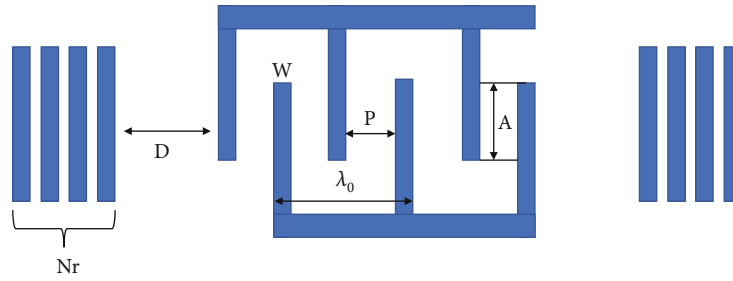


FIGURE 3: Design parameters for a single port SAW-based temperature sensor.

TABLE 3: Summary of geometric parameters for the proposed IDT and reflector structures for the SAW resonator.

Parameter	Symbol	Values for device 1	Values for device 2
Electrode finger width of IDT	W	$350 \mu\text{m}$	$2 \mu\text{m}$
Space between adjacent electrode fingers of IDT	P	$300 \mu\text{m}$	$2 \mu\text{m}$
Aperture width of the IDT finger	A	$6000 \mu\text{m}$	$300 \mu\text{m}$
Number of IDT finger pairs	N_o	25	25
Number of SAW reflector pairs	N_r	62	62
Distance between IDT and reflectors	D	$200 \mu\text{m}$	$3 \mu\text{m}$
Thickness of IDT electrode fingers	t	$200 \mu\text{m}$	$0.5 \mu\text{m}$

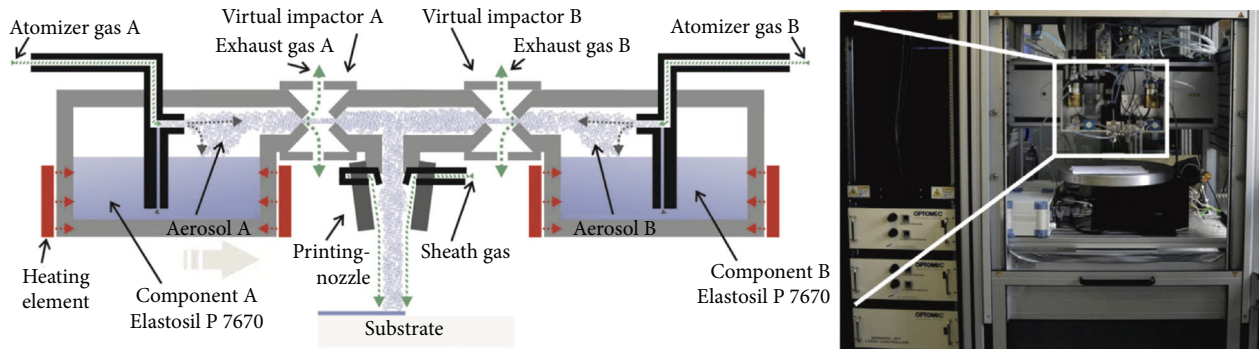


FIGURE 4: Functional block diagram for the generation of aerosol streams for a typical AJ-based printer [48].

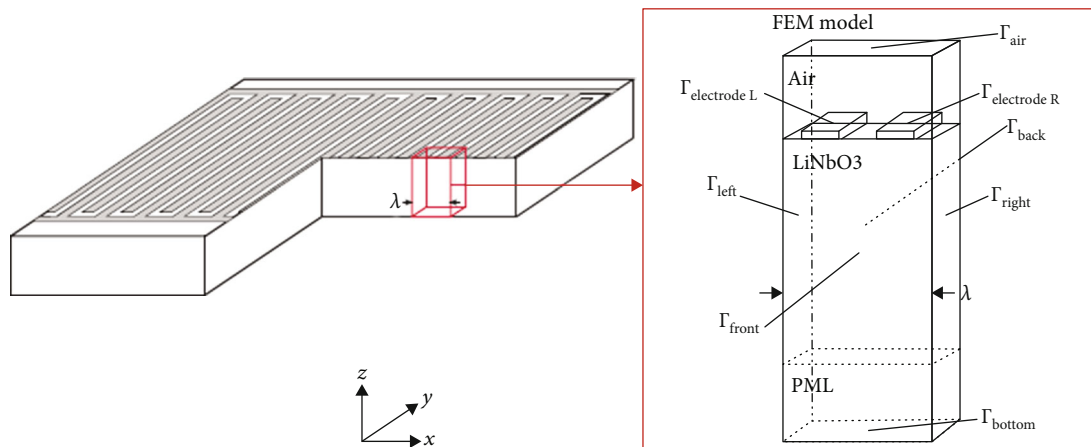


FIGURE 5: Finite element model for the analysis of the proposed SAW-based temperature sensing devices [49].

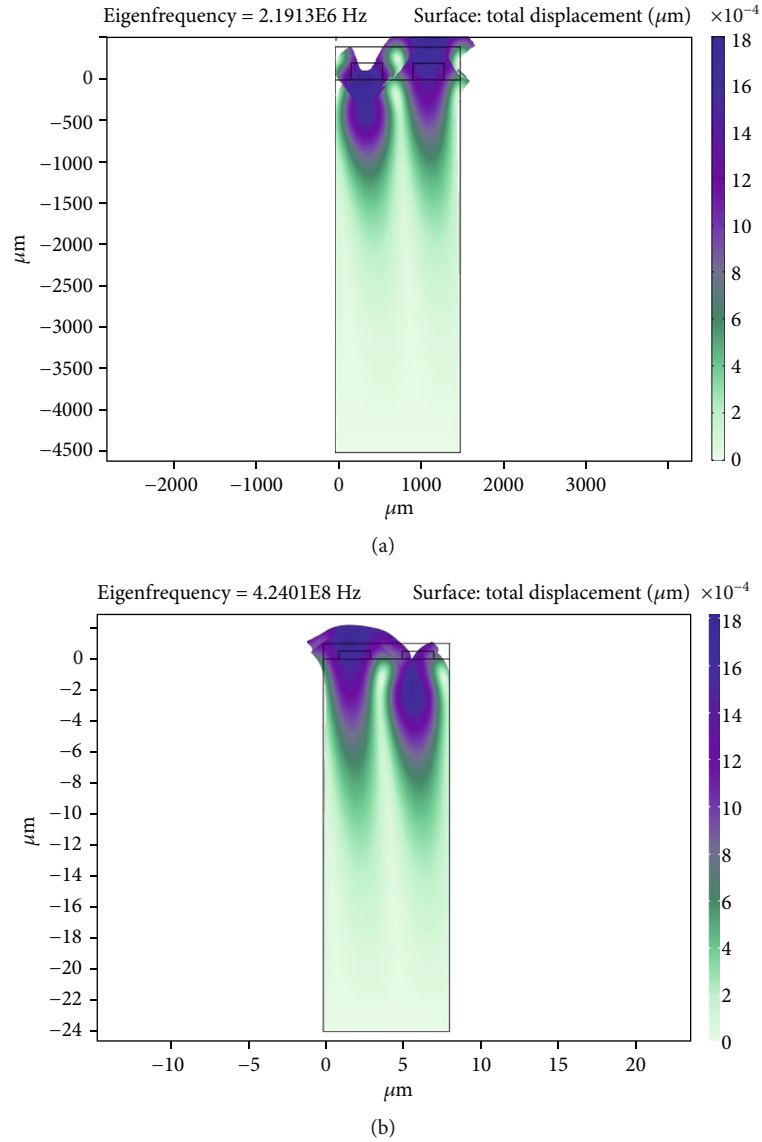


FIGURE 6: Resonant frequency mode plot of the proposed SAW temperature sensors with aluminium electrodes as IDTs: (a) device 1 and (b) device 2.

The IDT structure needs to be quantified in order to develop its model. Figure 3 and Table 3 show the labelled IDT structure and its explanation, respectively.

In order to achieve the strongest IDT activation and phase superposition of SAW, the IDT pitch, which is $W + P$, should be equal to half of the SAW wavelength, as described by the wave interference principle. Therefore,

$$W + P = N \frac{\lambda_0}{2}. \quad (2)$$

The distance between the IDT and the adjacent reflectors should also satisfy equation (3) to make sure

that IDT receives the standing wave on its peak.

$$D = \left(N - \frac{1}{2} \right) \frac{\lambda_0}{2}. \quad (3)$$

Aperture width of the IDT fingers also plays an important role in the performance of the SAW resonator. Normally, it is between 50 and 100 times the SAW wavelength [47].

2.3. Aerosol Jet-Based 3D Printing. The possibility of the mass production of the 3D printed electronic structures is directly correlated to the advancements in the 3D printing technology, stereolithography. To this end, Optomec's AJ system, which using additive manufacturing,

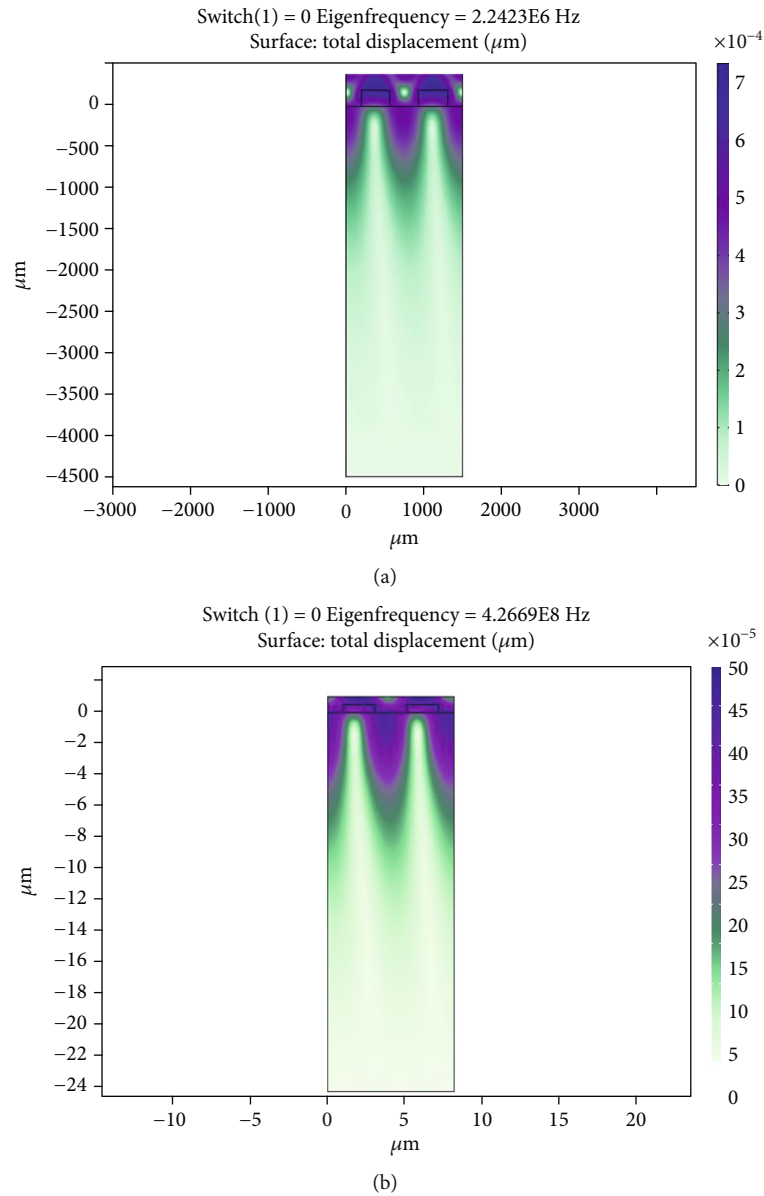


FIGURE 7: Antiresonant frequency mode plot of the proposed SAW temperature sensors with aluminium electrodes as IDTs: (a) device 1 and (b) device 2.

offers the possibility of producing those minute electronic sensing structures to any desirable substrate using nanoparticles from the range of 1 mm to 10 microns. The working principle of the AJ-based system is shown in Figure 4.

A pneumatic or more preferably ultrasonic, due to fewer suspension requirements, the based transducer is utilized to produce the aerosol flow which is then focused on the substrate to be deposited via a printing nozzle by forming a coaxial flow between the aerosol and inert gas streams acting as a sheath. The coaxial flow prevents the internal clogging in the printing nozzle. The width of the deposited structure on the substrate can be as minute as 10 microns if a 100-micron printing nozzle is used. Once

the deposition of the structure is finished, a sintered laser can be used to extract the final structure.

The fabrication of the proposed device using a direct 3D printing technique will be implemented for two different scenarios. The first scenario will have a YZ-cut lithium niobate as the piezoelectric substrate with a thin polyisobutylene film using aluminium for IDT electrodes. The second scenario will have copper IDT electrodes, and the rest will stay the same.

3. Results and Discussion

The finite element analysis of the proposed SAW-based temperature sensing devices is performed using COMSOL

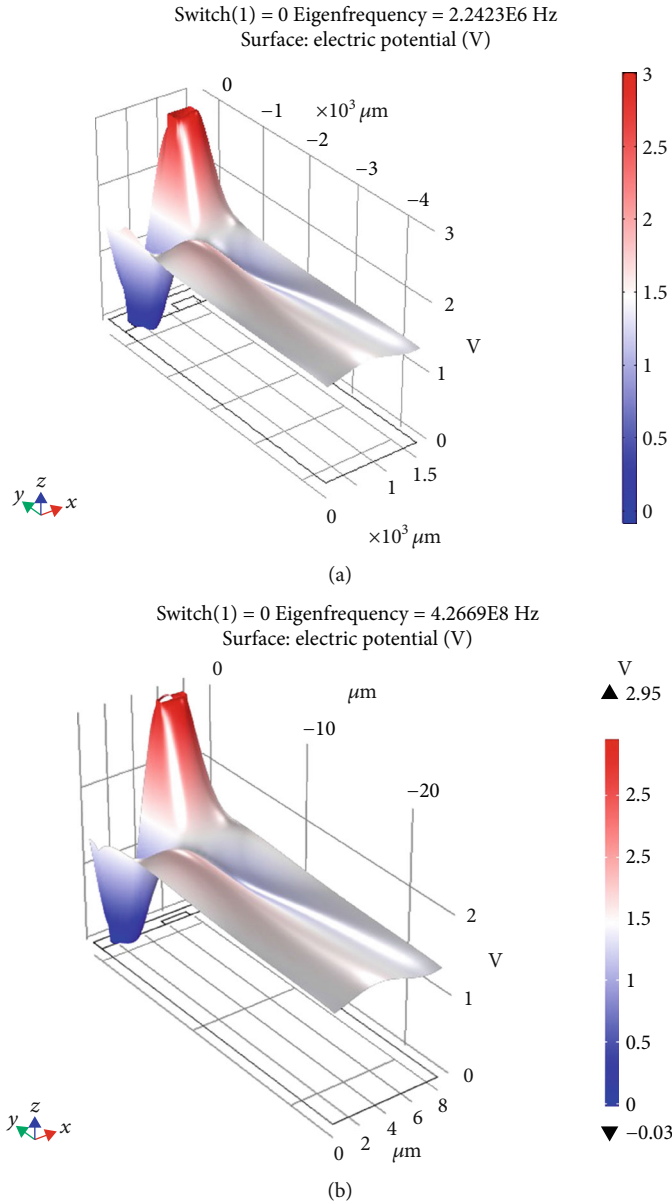


FIGURE 8: Electrical potential distributions at the 2nd eigenfrequencies of the proposed SAW temperature sensors: (a) device 1 and (b) device 2.

multiphysics. The results of those analyses are used to simulate and thus evaluate the performance of those devices. The configuration of the proposed devices is described in Section 2. The analysis can be performed using a pair of electrode fingers, since IDTs are periodic, for displacement. Again, using the boundary conditions, the aperture of the device can be assumed infinite reducing it to a few of the wavelength. The developed model is illustrated in Figure 5.

3.1. Implementation of SAW Using Aluminium Electrodes. The resonance frequency of the SAW-based resonator is calculated via piezoelectric material and eigenfrequency which in turn determines the velocity of the SAW in the designed structure. YZ-cut lithium niobate structure with the follow-

ing constants is used for this study. Equations (4) defines the elasticity matrix as E :

$$E = \begin{bmatrix} 242.4 & 75.2 & 75.2 & 0 & 0 & 0 \\ 0 & 203 & 57.3 & 0 & 8.5 & 0 \\ 0 & 0 & 203 & 0 & -8.5 & 0 \\ 0 & 0 & 0 & 75.2 & 0 & 8.5 \\ 0 & 0 & 0 & 0 & 59.5 & 0 \\ 0 & 0 & 0 & 0 & 0 & 59.5 \end{bmatrix} \times 10^9. \tag{4}$$

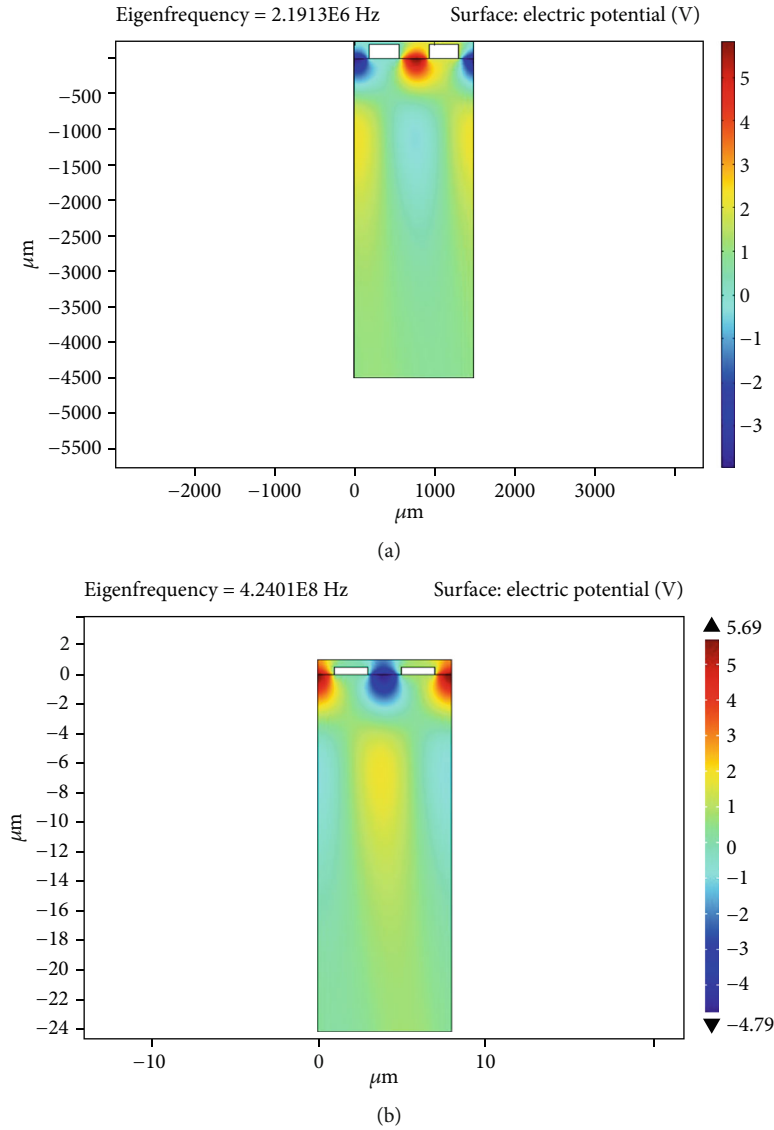


FIGURE 9: Sensors: (a) device 1 and (b) device 2.

The coupling matrix is shown in equation (5) as C :

$$C = \begin{bmatrix} 1.33 & 0.23 & 0.23 & 0 & 0 & 0 \\ 0 & 0 & 0 & -2.5 & 0 & 3.7 \\ 0 & -2.5 & 2.5 & 0 & 3.7 & 0 \end{bmatrix} \times C/m^2. \quad (5)$$

The relative permittivity, ϵ , is described in equation (6) as:

$$\epsilon = \begin{bmatrix} 28.7 & 0 & 0 \\ 0 & 85.2 & 0 \\ 0 & 0 & 85.2 \end{bmatrix}. \quad (6)$$

The density is 0.918 g/cm^3 while Poisson's ratio is considered to be 0.48 and Young's modulus is 10 GPa. The usage of the periodic boundary condition implies that the electrical potential and the displacement are identical along both the vertical sections of the model.

The results of the analysis show the resonant frequencies, as shown in Figure 6, for SAW device 1 and device 2 to be at 2.19 MHz and 424.01 MHz, respectively. The antiresonant frequencies, depicted in Figure 7, for SAW device 1 and device 2 are 2.24 MHz and 426.69 MHz, respectively.

Considering the first and second eigenfrequencies of the SAW modes, shown in Figures 6 and 7, the electric potential distribution characteristics according to the illustrated solutions are shown in Figure 8 below.

The electrical response of both the proposed devices is presented in Figure 9. It can be seen from the graph that when an electrical potential is applied to the IDTs, the device

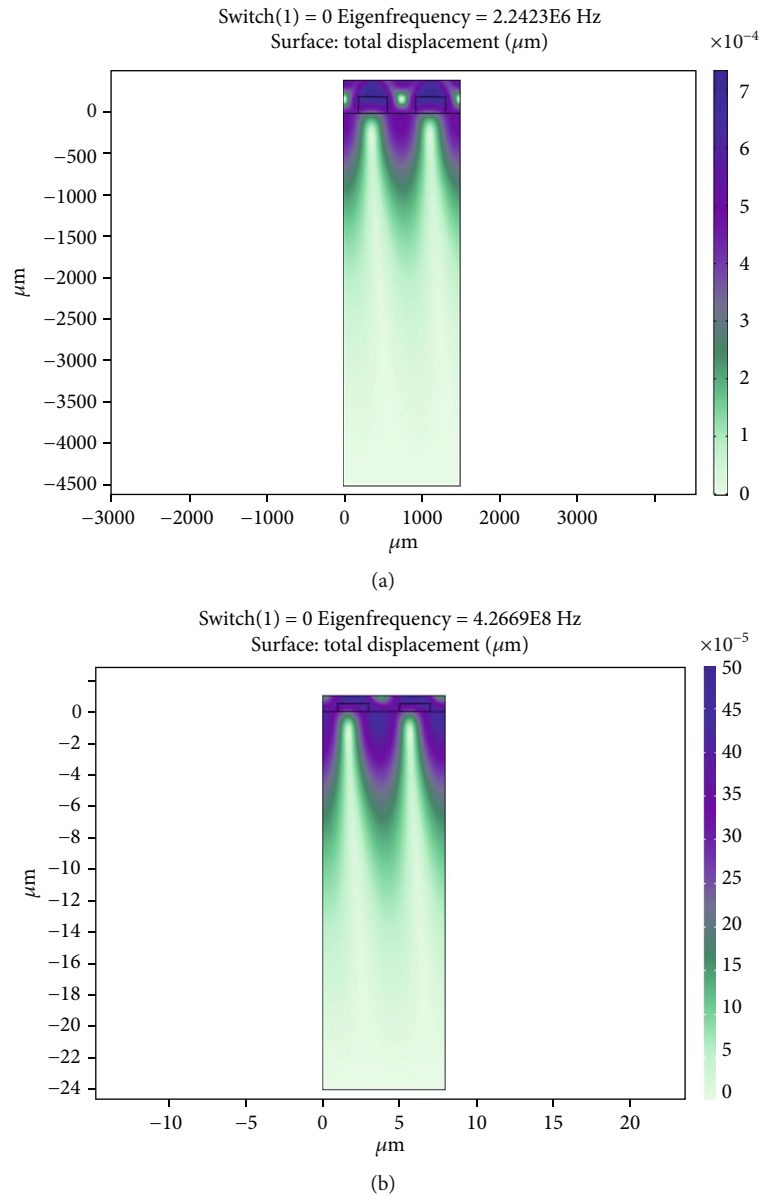


FIGURE 10: Resonant frequency mode plot of the proposed SAW temperature sensors with copper electrodes as IDTs: (a) device 1 and (b) device 2.

experiences strain in its piezoelectric substrate and produces SAW that travels across the surface and thus causing deformation in the structure.

3.2. Implementation of SAW Using Copper Electrodes. The same analysis is performed for the device having copper electrodes. The results of the analysis show the resonant frequencies, shown in Figure 10, for SAW device 1 and device 2 to be at 2.07 MHz and 398.22 MHz, respectively. The antiresonant frequencies, depicted in Figure 11, for SAW device 1 and device 2 are 2.43 MHz and 401.57 MHz, respectively.

2 MHz and 4 MHz SAW-based sensing structures are designed and modelled in this paper. In order to derive the output voltages and the displacement of the SAW sensors,

transient analyses are performed using COMSOL software. The results for the field displacement are shown in Figures 6, 7, 10, and 11. Aluminium electrode-based one-port resonator shows a maximum displacement of $1800 \mu\text{m}$ for device 1 and $12 \mu\text{m}$ for device 2. Meanwhile, these values for copper-based one-port resonator were near to $0 \mu\text{m}$ for device 1 and $10 \mu\text{m}$ for device 2. Results show that electrodes based on aluminium are more efficient for the excitation of the sensing structure. Results also indicate that in all considered cases, the in-plane horizontal displacements are more important than the vertical ones, confirming thus the shear-horizontal nature of the generated waves. Results indicate that acoustic waves generated in the first device are in advance by about 0.05 V, with respect to the second device.

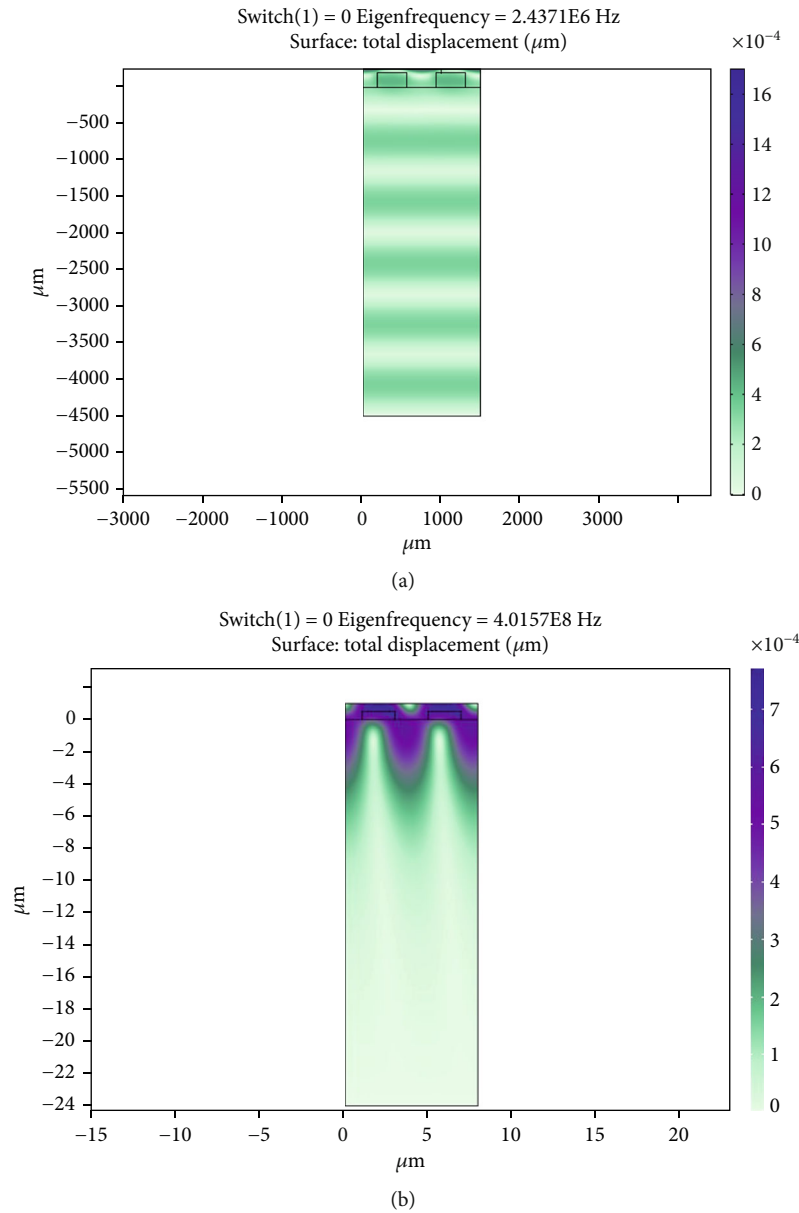


FIGURE 11: Antiresonant frequency mode plot of the proposed SAW temperature sensors with aluminium electrodes as IDTs.

4. Conclusion

SAW-based sensing technology in combination with the advancements in the 3D printing techniques shows promise for its implementation in wireless sensing applications. To this end, SAW-based temperature sensing devices were designed and modelled using COMSOL multiphysics and presented in this paper. All the structural designed parameters for both the proposed devices were calculated, and the simulations of their eigenfrequencies and impedances were performed using FEM. The designed sensors were found to be operating at 2.19 MHz for device 1 and 424 MHz for device 2 using YZ-cut lithium niobate as substrate and aluminium as the conducting metal for IDT electrodes. The proposed sensors have the capabilities of being a passive wireless

sensing device. Finally, the findings presented in this paper pave the way for the possible fabrication of SAW-based temperature sensors with high accuracy using the AJ system-based direct 3D printing method.

Data Availability

All the data generated or analysed for this study are included in the article.

Conflicts of Interest

All the authors declare no conflict of interest.

References

- [1] Z. Zhan, J. An, Y. Wei, and D. Hejun, "Inkjet-printed optoelectronics," *Nanoscale*, vol. 9, no. 3, pp. 965–993, 2017.
- [2] Y. Khan, A. Thielens, S. Muin, J. Ting, C. Baumbauer, and A. C. Arias, "A new frontier of printed electronics: flexible hybrid electronics," *Advanced Materials*, vol. 32, no. 15, p. 1905279, 2020.
- [3] S. Khan, L. Lorenzelli, and R. S. Dahiya, "Technologies for printing sensors and electronics over large flexible substrates: a review," *IEEE Sensors Journal*, vol. 15, no. 6, pp. 3164–3185, 2014.
- [4] M. G. Mohammed and R. Kramer, "All-printed flexible and stretchable electronics," *Advanced Materials*, vol. 29, no. 19, p. 1604965, 2017.
- [5] A. K. Au, W. Huynh, L. F. Horowitz, and A. Folch, "3D-printed microfluidics," *Angewandte Chemie International Edition*, vol. 55, no. 12, pp. 3862–3881, 2016.
- [6] M. Berggren, D. Nilsson, and N. Robinson, "Organic materials for printed electronics," *Nature materials*, vol. 6, no. 1, pp. 3–5, 2007.
- [7] J. Perelaer, P. J. Smith, D. Mager et al., "Printed electronics: the challenges involved in printing devices, interconnects, and contacts based on inorganic materials," *Journal of Materials Chemistry*, vol. 20, no. 39, pp. 8446–8453, 2010.
- [8] R. F. Pease and S. Y. Chou, "Lithography and other patterning techniques for future electronics," *Proceedings of the IEEE*, vol. 96, no. 2, pp. 248–270, 2008.
- [9] A. Nathan, A. Ahnood, M. T. Cole et al., "Flexible electronics: the next ubiquitous platform," *Proceedings of the IEEE*, vol. 100, no. Special Centennial Issue, pp. 1486–1517, 2012.
- [10] R. R. Søndergaard, M. Hösel, and F. C. Krebs, "Roll-to-roll fabrication of large area functional organic materials," *Journal of Polymer Science Part B: Polymer Physics*, vol. 51, no. 1, pp. 16–34, 2013.
- [11] M. Bozzi, C. Tomassoni, L. Perregrini, R. Bahr, and M. Tentzeris, "Additive manufacturing of substrate integrated waveguide components," *Advanced Materials and Processes for RF and THz Applications (IMWS-AMP) 2016 IEEE MTT-S International Microwave Workshop Series on*, pp. 1–4, 2016.
- [12] D. L. Tong, A. A. Manga, P. Minard, A. Delattre, L. Crowther-Alwyn, and P. Borel, "Comparative study of WLAN dual-band monopole antennas printed and etched on paper and PET substrates," in *2016 46th European Microwave Conference (EuMC)*, pp. 1243–1246, London, UK, 2016.
- [13] Y. Morimoto, M. Memarian, X. Li, and T. Itoh, "Open-end microstrip line terminations using lossy gray-scale inkjet printing," *Microwave Theory and Techniques IEEE Transactions on*, vol. 65, no. 12, pp. 4861–4870, 2017.
- [14] A. Sahu, P. H. Aaen, A. Lewandowski et al., "Robust microwave characterization of inkjet-printed coplanar waveguides on flexible substrates," *Instrumentation and Measurement IEEE Transactions on*, vol. 66, no. 12, pp. 3271–3279, 2017.
- [15] A. K. Au, W. Lee, and A. Folch, "Mail-order microfluidics: evaluation of stereolithography for the production of microfluidic devices," *Lab on a Chip*, vol. 14, no. 7, pp. 1294–1301, 2014.
- [16] J. J. Adams, S. C. Slimmer, J. A. Lewis, and J. T. Bernhard, "3D-printed spherical dipole antenna integrated on small RF node," *Electronics Letters*, vol. 51, no. 9, pp. 661–662, 2015.
- [17] J. Kimionis, M. Isakov, B. S. Koh, A. Georgiadis, and M. M. Tentzeris, "3D-printed origami packaging with inkjet-printed antennas for RF harvesting sensors," *IEEE Transactions on Microwave Theory and Techniques*, vol. 63, no. 12, pp. 4521–4532, 2015.
- [18] M. T. Rahman, A. Rahimi, S. Gupta, and R. Panat, "Microscale additive manufacturing and modeling of interdigitated capacitive touch sensors," *Sensors and Actuators A: Physical*, vol. 248, pp. 94–103, 2016.
- [19] D. Zhang, C. Jiang, J. Tong, X. Zong, and W. Hu, "Flexible strain sensor based on layer-by-layer self-assembled graphene/polymer nanocomposite membrane and its sensing properties," *Journal of Electronic Materials*, vol. 47, no. 4, pp. 2263–2270, 2018.
- [20] B. Andò, S. Baglio, S. La Malfa, and G. L'Episcopo, "All inkjet printed system for strain measurement," in *SENSORS, 2011 IEEE*, pp. 215–217, Limerick, Ireland, 2011.
- [21] H. Yang, T. Rahman, D. Du, R. Panat, and Y. Lin, "3-D printed adjustable microelectrode arrays for electrochemical sensing and biosensing," *Sensors and Actuators B: Chemical*, vol. 230, pp. 600–606, 2016.
- [22] T. Rahman, L. Renaud, D. Heo, M. Renn, and R. Panat, "Aerosol based direct-write micro-additive fabrication method for sub-mm 3D metal-dielectric structures," *Journal of Micromechanics and Microengineering*, vol. 25, no. 10, p. 107002, 2015.
- [23] C. Goth, S. Putzo, and J. Franke, "Aerosol Jet printing on rapid prototyping materials for fine pitch electronic applications," in *2011 IEEE 61st electronic components and technology conference (ECTC)*, pp. 1211–1216, Lake Buena Vista, FL, USA, 2011.
- [24] J. H. Cho, J. Lee, Y. U. Xia et al., "Printable ion-gel gate dielectrics for low-voltage polymer thin-film transistors on plastic," *Nature materials*, vol. 7, no. 11, pp. 900–906, 2008.
- [25] A. Mette, P. L. Richter, M. Hörteis, and S. W. Glunz, "Metal aerosol jet printing for solar cell metallization," *Progress in Photovoltaics: Research and Applications*, vol. 15, no. 7, pp. 621–627, 2007.
- [26] C. Yang, E. Zhou, S. Miyanishi, K. Hashimoto, and K. Tajima, "Preparation of active layers in polymer solar cells by aerosol jet printing," *ACS Applied Materials & Interfaces*, vol. 3, no. 10, pp. 4053–4058, 2011.
- [27] I. Ertugrul and T. Waqar, "Fabrication of bidirectional electrothermal microactuator by two-photon polymerization," *Current Nanoscience*, vol. 16, 2020.
- [28] I. Ertugrul, "The fabrication of micro beam from photopolymer by digital light processing 3D printing technology," *Micromachines*, vol. 11, no. 5, p. 518, 2020.
- [29] J. Kirschner, "Surface acoustic wave sensors (SAWS)," *Micromechanical systems*, 2010.
- [30] B. Liu, C. Zhang, X. Ji, J. Chen, and T. Han, "An improved performance frequency estimation algorithm for passive wireless SAW resonant sensors," *Sensors*, vol. 14, no. 12, pp. 22261–22273, 2014.
- [31] <https://www.fierceelectronics.com/components/acoustic-wave-technology-sensors>.
- [32] D. C. Malocha, "Evolution of the SAW transducer for communication systems," in *IEEE Ultrasonics Symposium, 2004*, vol. 1, pp. 302–310, Montreal, QC, Canada, 2004.
- [33] S. Xu, C. Li, H. Li, M. Li, Q. Changqing, and B. Yang, "Carbon dioxide sensors based on a surface acoustic wave device with a

- graphene–nickel–L-alanine multilayer film,” *Journal of Materials Chemistry C*, vol. 3, no. 16, pp. 3882–3890, 2015.
- [34] D. C. Malocha, M. Gallagher, B. Fisher, J. Humphries, D. Gallagher, and N. Kozlovski, “A passive wireless multi-sensor SAW technology device and system perspectives,” *Sensors*, vol. 13, no. 5, pp. 5897–5922, 2013.
- [35] S.-H. Seo, W.-C. Shin, and J.-S. Park, “A novel method of fabricating ZnO/diamond/Si multilayers for surface acoustic wave (SAW) device applications,” *Thin Solid Films*, vol. 416, no. 1-2, pp. 190–196, 2002.
- [36] M. R. Zakaria, U. Hashim, and M. H. I. M. Amin, “Design and fabrication of IDT saw by using conventional lithography technique,” *Middle-East Journal of Scientific Research*, vol. 18, no. 9, pp. 1281–1285, 2013.
- [37] M. Maiwald, C. Werner, V. Zoellmer, and M. Busse, “INKtel-ligent printed strain gauges,” *Sensors and Actuators A: Physical*, vol. 162, no. 2, pp. 198–201, 2010.
- [38] B. Thompson and H.-S. Yoon, “Aerosol printed carbon nanotube strain sensor,” in *Smart Sensor Phenomena, Technology, Networks, and Systems Integration 2012*, vol. 8346, article 83461C, International Society for Optics and Photonics, 2012.
- [39] Y. Zhang, N. Anderson, S. Bland, S. Nutt, G. Jursich, and S. Joshi, “All-printed strain sensors: building blocks of the aircraft structural health monitoring system,” *Sensors and Actuators A: Physical*, vol. 253, pp. 165–172, 2017.
- [40] B. Thompson and H.-S. Yoon, “Aerosol-printed strain sensor using PEDOT: PSS,” *IEEE Sensors Journal*, vol. 13, no. 11, pp. 4256–4263, 2013.
- [41] W. C. Wilson and G. M. Atkinson, “Passive wireless sensor applications for NASA’s extreme aeronautical environments,” *IEEE Sensors Journal*, vol. 14, no. 11, pp. 3745–3753, 2014.
- [42] R. R. Romanosky and S. M. Maley, “Harsh environment sensor development for advanced energy systems,” in *Micro-and Nanotechnology Sensors, Systems, and Applications V*, vol. 8725, article 87250H, International Society for Optics and Photonics, 2013.
- [43] E. J. Fichtel and A. D. McDaniel, *High Temperature Strain Gage Technology for Gas Turbine Engines*, 1994.
- [44] J.-F. Lei and H. A. Will, “Thin-film thermocouples and strain-gauge technologies for engine applications,” *Sensors and Actuators A: Physical*, vol. 65, no. 2-3, pp. 187–193, 1998.
- [45] J. Watson and G. Castro, “A review of high-temperature electronics technology and applications,” *Journal of Materials Science: Materials in Electronics*, vol. 26, no. 12, pp. 9226–9235, 2015.
- [46] M. L. Chin, *A fabrication study of surface acoustic wave devices for magnetic field detection*, 2006.
- [47] X. Ye, F. Lu, B. Liang et al., “Studies of a high-sensitive surface acoustic wave sensor for passive wireless blood pressure measurement,” *Sensors and Actuators A: Physical*, vol. 169, no. 1, pp. 74–82, 2011.
- [48] S. Reitelshöfer, M. Göttler, P. Schmidt, P. Treffer, M. Landgraf, and J. Franke, “Aerosol-Jet-Printing silicone layers and electrodes for stacked dielectric elastomer actuators in one processing device,” in *Electroactive Polymer Actuators and Devices (EAPAD) 2016*, vol. 9798, article 97981Y, International Society for Optics and Photonics, 2016.
- [49] H. Chambon, P. Nicolay, G. Bruckner, and A. Benjeddou, “Analysis of the sensitivity to pressure and temperature of a membrane based SAW sensor,” *International Journal of Smart and Nano Materials*, vol. 8, no. 2-3, pp. 95–109, 2017.

Research Article

Lifetime Prediction for a Cell-on-Board (COB) Light Source Based on the Adaptive Neuro-Fuzzy Inference System (ANFIS)

İsmail Kiyak ¹, Gökhan Gökmen ² and Gökhan Koçyiğit ³

¹Department of Electrical and Electronics Engineering, Faculty of Technology, Marmara University, Istanbul, Turkey

²Department of Mechatronics Engineering, Faculty of Technology, Marmara University, Istanbul, Turkey

³Department of Electric and Electronics Engineering, Faculty of the Engineering, Trakya University, Edirne, Turkey

Correspondence should be addressed to İsmail Kiyak; imkiyak@marmara.edu.tr

Received 29 November 2020; Accepted 20 March 2021; Published 31 March 2021

Academic Editor: Hassan Karimi-Maleh

Copyright © 2021 İsmail Kiyak et al. This is an open access article distributed under the Creative Commons Attribution License, which permits unrestricted use, distribution, and reproduction in any medium, provided the original work is properly cited.

Predicting the lifetime of a LED lighting system is important for the implementation of design specifications and comparative analysis of the financial competition of various illuminating systems. Most lifetime information published by LED manufacturers and standardization organizations is limited to certain temperature and current values. However, as a result of different working and ambient conditions throughout the whole operating period, significant differences in lifetimes can be observed. In this article, an advanced method of lifetime prediction is proposed considering the initial task areas and the statistical characteristics of the study values obtained in the accelerated fragmentation test. This study proposes a new method to predict the lifetime of COB LED using an artificial intelligence approach and LM-80 data. Accordingly, a database with 6000 hours of LM-80 data was created using the Neuro-Fuzzy (ANFIS) algorithm, and a highly accurate lifetime prediction method was developed. This method reveals an approximate similarity of 99.8506% with the benchmark lifetime. The proposed methodology may provide a useful guideline to lifetime predictions of LED-related products which can also be adapted to different operating conditions in a shorter time compared to conventional methods. At the same time, this method can be used in the life prediction of nanosensors and can be produced with the 3D technique.

1. Introduction

Before the 1990s, LEDs were used in backlighting, communication, healthcare services, and signage and accent lighting systems especially thanks to their small (<10 mm) size [1, 2]. With the correct design, they offer the energy saving advantages of higher energy efficiency with lower voltage (usually <4 volts) and operation at low currents (usually <700 mA) with lower power consumption [3]. LED lighting fixtures are superior to traditional light sources with their properties such as saving energy (high efficiency), long life (50,000-100,000 hours), smaller size, perfect on/off response, low-temperature lighting, and being free of environmentally hazardous mercury (Hg) [4, 5]. Their on/off response time of microseconds, a wide range of color temperatures (3200-12,000 K) that is controllable, and a wide range of operating temperatures (20-950°C) guarantee high performance [6].

Usage of high-power white LEDs (HPLEDs) in light fixtures is currently a subject of extensive research, and HPLEDs have an increasing market share thanks to their environmentally friendly features, crucially important to help prevent global warming [7, 8].

The main limitation of the lighting fixtures of LED semiconductor components is the low power of single-chip diodes and the resulting low luminous flux. Manufacturers of light fixtures tried and solved this problem by creating a matrix structure with multiple single-chip LEDs [9, 10]. The product of fixing a multichip LED on a surface and covering it with a phosphorus-silicon mixture based on traditional filling technology is the COB (cell on board), a high-brightness, high-power white light that can be used indoors and outdoors [11]. This technology makes it possible to place multichips in a small area in order to create a multichip LED structure [12]. LED lighting fixtures of approximately 500 W power

and 60,000lm luminous flux can be produced by securing good thermal conductivity with the help of modern thermal conductive adhesives [13, 14].

The COB technology allows the side-by-side mounting of LED chips directly on a substrate or circuit board. This package design enables higher power intensity [15]. As LED chips are very closely spaced, designers must first optimize the distance between them to ensure an ideal balance of their thermal and optical properties [16, 17]. A LED array can be formed with two different methods. The first one is to line a printed circuit board (PCB) with high-power LED packages of the surface mount type (SMT). The other is to directly form a matrix with the chips on a PCB (these are called a COB array) [18]. There are two types of COB packages: ceramic substrate and metal substrate [19].

Nowadays, commercial demands for LED-containing fixtures in terms of lumen degradation are based entirely on the data from LM-79 and LM-80 and the TM-21 calculations [20]. IES LM-80-08 is an approved method for measuring the lumen values of LED lighting sources. The IES standard TM-21-11 is the most common method used to predict the lifetime of LED fixtures. For reliable long-term predictions, at least 6000 hours of testing are needed with LM-80 [21, 22]. The mean value for the normalized light output values from the LM-80 report is used, and a nonlinear regression is performed for a lifetime prediction model [20].

Figure 1 shows the change occurring in lifetime L (luminous flux) of the LED equipment over time. The formula called $B_{50} - L_{70}$ means that 50% of the lumen output (B_{50}) is smaller than 70% (L_{70}) of the baseline. Lamp manufacturers perform lifetime testing on their products and define the lamp's lifetime as the length of time that the light output drops below L_{70} in 50% of the testing time [24]. $L_{70}-L_{85}$ are mostly preferred for outdoor applications, whereas L_{90} is preferred for indoor applications. In some lighting projects that do not require precise lighting, L_{50} is also considered and used as a design parameter [23].

Qu et al. proposed a lifetime prediction method based on an accelerated distortion test and statistical data on lifetime [23]. Sun et al. used both the structure of the LED and the impact of the driver on the light source [2], and Li et al. used the Weibull distribution to determine the error rate of the prediction method [24]. Chen et al. presented an online test method at a test temperature of 125°C [25]. Park and Kim used the gamma model to predict the service life of LEDs [5], and Zhang et al. estimated the mean time to failure (MTTF) using exponential distribution [26]. Liu et al. studied the ANN distribution for temperature and lifetime in multi-chip LEDs [27], and Alfarog et al. used the thermally connected FEM [28]. Niu et al. studied the effects of LED driver Al-Cap core on life parameters [7]. Wang and Chu performed accelerated degradation testing (ADT) for light bars used in laptops [29]. Hao et al. performed the gradual aging test based on the Nelson model [30], and Wang and Lu used the degradation-data-driven method (DDDM) to predict the lifetime of HP white LEDs [6].

The lifetime calculations for LED light sources were previously performed using conventional methods; however,

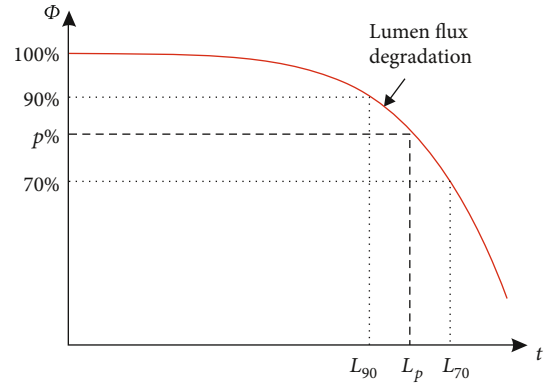


FIGURE 1: Luminous flux change curve for the LED light source based on time [23].

AI-based calculation methods are more and more employed in recent years. In this study, an innovative method is proposed to predict the lifetime of a COB LED light source that is in the process of being introduced to the market. The proposed technique uses LM-80 data obtained in accordance with the IES TM-21-11 Lifetime Prediction Method to develop a prediction method based on AI (artificial intelligence). In line with the method developed, a data set for training and testing was created for ANFIS based on the results of measurements performed for 6000 hours. The developed ANFIS architecture allows for a high-accuracy lifetime prediction for the COB LED. This article is organized as follows: In the first part, the structure of the COB LED and semiconductor lifetime prediction methods are explained. The second part is dedicated to elaborating the COB LED used in the study, the lifetime prediction method, and the ANFIS structure. The lifetime prediction method developed for the selected COB LED lamp and the results obtained are described in the third part, and the last part concludes this study.

2. Methodology and Calculations of COB LED L_{70}

For this project, a technically and economically advanced system was developed due to the high density of large buildings in Istanbul. Accordingly, energy-production estimates were obtained using the PV*SOL program based on 1-year sunshine data for Istanbul. The real-time application was then compared with the production data. PV plants with 23.68 kW of DC power were installed on the roofs of three buildings with similar features in the same location (in the Başakşehir District of Istanbul). All three PV plants (fixed-angle, adjustable-angle, and automatic solar-tracking systems) were mounted on the buildings, and each was comprised of 320 W polycrystalline PV panels with 16.5% efficiency.

An EV charging station enables the recharging of EVs using external energy sources. Although such systems are usually connected to the grid, they may also be connected to renewable energy sources. EV charging stations draw high current during operations and also generate harmonics due

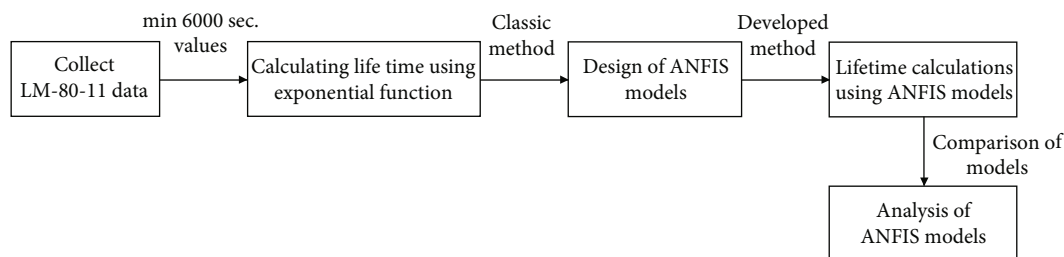


FIGURE 2: Block diagram of the methodology.

TABLE 1: Technical specifications of the Nichia NVELJ048Z COB LED used in the study [32].

Item	Symbol	Absolute maximum rating	Unit
Forward current	I_F	1000	mA
Pulse forward current	I_{FP}	1500	mA
Allowable reverse current	I_R	85	mA
Power dissipation	P_D	38.7	W
Operating temperature	T_{opr}	-40~105	$^{\circ}\text{C}$
Storage temperature	T_{stg}	-40~100	$^{\circ}\text{C}$
Junction temperature	T_J	150	$^{\circ}\text{C}$

to the structure of their electronic circuits. Therefore, EV charging stations should have filtering and compensation systems so as to conform to standards. Overcurrent, short-circuit, and residual-current protections should be present in every electrical device; these features are available as the standard for these devices. Furthermore, these stations should have a software infrastructure for processing the charging data because of the need for energy sales at the stations. A communication system that is capable of sharing data with the relevant companies and processing data for the user's account is also needed. This communication can be provided by systems such as Wi-Fi, GPRS, RS-485, and TCP/IP. EV charging stations also often have hardware such as radio-frequency identification card readers for users. The standards for charging stations vary by region. Prediction of the useful lifetime of light power is based on a standard procedure. The LM-80-08 standard, published by the Illuminating Engineering Society of North America (IESNA), is used to predict the lifetime of light sources with the help of an exponential regression equation calculated on the basis of the reduction of initial luminous flux [31]. The traditional method of estimating lifetime is the regression model [5].

What makes this study stand out from others on the same theme can be explained as follows:

- (1) In recent studies performed to predict the lifetime of LEDs, the Fuzzy Logic and Neural Network algorithms from among the AI methods were used. This

study uses the Adaptive Neuro-Fuzzy Inference System (ANFIS) for COB LED lifetime prediction

- (2) Most of the work performed is based on techniques used exclusively for a tester. The method developed in this study provides fast and accurate results for all semiconductor lighting products with an LM-80-08 report

This study is aimed at developing a new method for the safe and fast determination of the lifetime of the COB LED light source, which has been used for lighting purposes in the last five years. The block diagram of the methodology is given in Figure 2.

Firstly, LM-80 test data obtained with at least 6000 hours of laboratory measurement of COB LED were obtained from the relevant company. In the study, COB LED with the product code of NVELJ048Z of the Nichia Corporation was used.

In the second stage, the COB LED L_{70} lifetime was calculated using the exponential function from the catalog data for the 80°C junction temperature.

In the third stage, three ANFIS models with different membership function types were created for detailed analysis of life expectancy. In order to find the most accurate approach according to the type of data obtained, models were created using the triangle, gbell, and Gaussian membership functions.

In the last stage, the lifetimes were calculated according to the ANFIS model. The life expectancies found using the exponential function and the ANFIS models were compared with the reference value.

2.1. Test Device. The research object selected for this study was the NVELJ048Z model white COB LED (Table 1) of Nichia Corporation.

A chip made of indium gallium nitride (GaN) was combined on the metal interconnection layer, and a ceramic substrate of high thermal conductivity $2\text{ W}/(\text{m}\cdot\text{K})$ was used to increase heat distribution [5, 32].

2.2. Lumen Maintenance Degradation (L_{70}). The IES TM-80-08 "Measurement of the Luminous Flux Maintenance in LED Light Sources" was further improved to develop and publish the IES TM-21-11 "Lifetime Prediction Method" standard in 2011, which helped to estimate long-term luminous flux drop with LM-80 data [33].

TABLE 2: Charging-station information reliability requirement of LED light source and LAMP in current standards [23].

Test item	Standards	Descriptions	Remark
Lumen maintenance	IES LM-80-08/Energy Star	6000 hr. life test at 3 different case temperatures: 55°C and 85°C, as defined by the manufacturer	10 samples by Energy Star
Rapid-cycle stress test	Energy Star	Cycle times: 2 minutes on, 2 minutes off. Lamp cycled once for every two hours of required minimum L_{70} life	10 samples by Energy Star
Lumen maintenance	IEC/PAS 62612	6000 hits life test at 45°C ambient temperature	Sample size 10
Rapid-cycle stress test	IEC/PAS 62612	Cycle times: 30 sec. on, 30 sec. off. Lamp cycled once for every two hours of required minimum L_{70} life	
Thermal shock	IEC/PAS 62612	-10°C~50°C 1 hr. dwell 5 cycles	

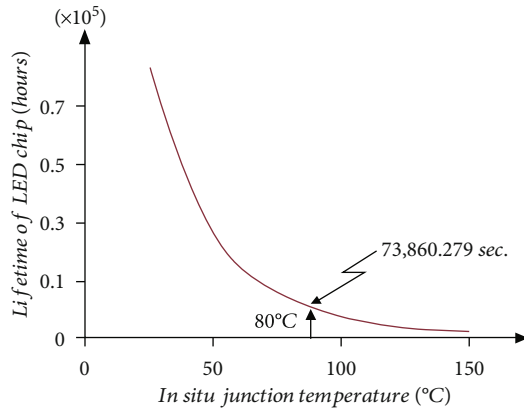
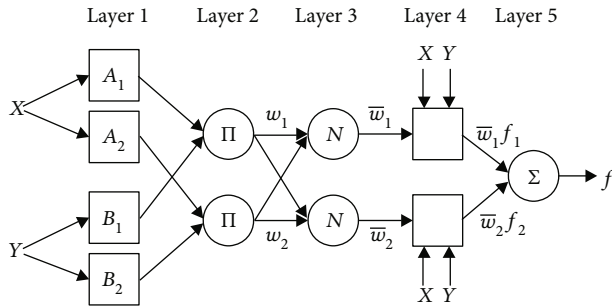
FIGURE 3: Calculation lifetime (L_{70}) using exponential function.

FIGURE 4: The ANFIS model with two inputs, two rules, and one output [35, 36].

According to the IES TM-21-11 Lifetime Prediction Method Standard, the luminous flux reduction is estimated using the LM-80 data. Under this standard, a minimum of 6000 hours of laboratory measurements are performed and this value is considered equal for the lifetime of the light fixture; however, the fixture's optical design and electrical elements should also be factored in as they affect the luminous flux [34].

The lifetime of light sources is described as the time until the lumen output of the lamp is reduced to less than 70% of the baseline as a result of the decrease in lumen or the deterioration caused by its electronic components [24]. Table 2 shows the change of lifetime in different operating modes over the lifetime of the lumen output of an LED light source

rather than measuring the lamp's entire lifetime. Nowadays, the IES LM-80 test data are a common requirement for lamps containing a LED light source in the market to simplify the evaluation of LED efficiency and state the product's lifetime. On the other hand, the LM-80 test reports are generally carried out below typical constant driving current values and specific conditions with at least three different ambient temperatures (55°C, 85°C, and one manufacturer-defined value) [23].

After the LM-80 test procedure, TM-21 is generally used for luminous maintenance with the mean values of LM-80 data, and lumen maintenance data can be specified by means of the least squares method using the exponential light replacement formulation:

$$\Phi_i(t) = B e^{(-\beta_i t)}, \quad (1)$$

where t is the working time in hours, $\Phi_i(t)$ is the average normalized luminous flux in the conditional state at time t , B is an estimated primary constant obtained from the least squares equation. β_i is a decay rate constant obtained from the Arrhenius formula incorporated with the ambient temperature ($T_{a,i}$):

$$\beta_i = A_0 e^{(-E_a/K \cdot T_{a,i})}, \quad (2)$$

where α is the decay rate constant obtained from the least squares equation, β is the shape factor [20, 26].

For each current and temperature, the L_{70} value, i.e., $\Phi = 0.7$, can be found by means of the average normalized light output:

$$L_{70} = \left(\frac{-\ln(0.7)}{\alpha} \right)^{1/\beta}. \quad (3)$$

Considering the $T_{j,i}$ -related appropriate junction temperature ($T_{j,i}$), the Arrhenius equation can be formulated as follows:

$$\beta_i = A_0 e^{(-E_a/K \cdot T_{j,i})}, \quad (4)$$

where A_0 is an exponential factor, E_a is the activation energy (eV), K is the Boltzmann constant

TABLE 3: Summary report for the Nichia COB LED LM-80-08 with model number NVELJ048Z [32].

Data set	Case temperature (T_S)	Ambient temperature (T_A)	Drive current (I_F)	Average current per die	Lumen maintenance at 10,000 hours	Chromaticity shift at 10,000 hours	TM-21 projection L_{70} (10 K)
1	55°C	>50°C	3300 mA	1100 mA	95.0%	0.0022	>55,000 hours
2	85°C	>80°C	2350 mA	783 mA	94.7%	0.0022	>55,000 hours
3	85°C	>80°C	3300 mA	1100 mA	94.4%	0.0024	>55,000 hours
4	105°C	>100°C	2350 mA	783 mA	94.0%	0.0022	>55,000 hours

TABLE 4: LED chip lifetime of light output maintenance.

Lifetime maintenance	1500 mA/57.3 °C	1500 mA/87.5 °C	1140 mA/87.4 °C	1140 mA/105.5 °C
L_{98}	4118.932	2945.860	4222.648	4418.790
L_{96}	8322.795	5952.463	8532.367	8928.695
L_{94}	12,615.171	9022.367	12,932.822	13,533.553
L_{92}	16,999.856	12,158.298	17,427.922	18,237.447
L_{90}	21,480.923	15,363.154	22,021.820	23,044.732
L_{88}	26,062.690	18,640.035	26,718.959	27,960.055
L_{86}	30,749.799	21,992.257	31,524.090	32,988.384
L_{84}	35,547.200	25,423.360	36,442.292	38,135.037
L_{82}	40,460.214	28,937.143	41,479.016	43,405.717
L_{80}	45,494.532	32,537.699	46,640.114	48,806.551
L_{78}	50,656.343	36,229.418	51,931.890	54,344.129
L_{76}	55,952.231	40,017.038	57,361.111	60,025.557
L_{74}	61,389.370	43,905.687	62,935.171	65,858.507
L_{72}	66,975.459	47,900.875	68,661.942	71,851.283
L_{70}	72,718.941	52,008.574	74,550.044	78,012.892

($8.6173 \cdot 10^{-5}$ eV/K), $T_{j,i}$ is the ambient temperature, $T_{a,j}$ is the absolute T_j .

$$L_p = \frac{\ln(100(B/p))}{\beta_i} = \frac{\ln(100(B/p))}{A_0 e^{(-E_a/K \cdot T_{j,i})}}, \quad (5)$$

where p is the percentage of the first maintained luminous output. The $T_{j,i}$ stated here is the instantaneous junction temperature of the LED under the working ambient conditions obtained with $T_{j,i}$.

In Figure 3, the lifetime curve is shown for Nichia brand NVELJ048Z model COB LED. Using equation (5), the COB L_{70} lifetime was found to be 168,844.6 hours, according to the catalog values and the calculation for the 80°C junction temperature.

2.3. Adaptive Neuro-Fuzzy Inference System. The Adaptive Neuro-Fuzzy Inference System (ANFIS) is a model based on the combination of Artificial Neural Networks (ANN) and Fuzzy Logic. It combines the flexible adaptability of Fuzzy Logic with ANN's successful classification performance. It is very successful in solving nonlinear problems.

In fact, ANFIS is a rule-based model such as the Fuzzy Inference System (FIS). The biggest challenge in FIS is to define a rule base [35–37]. Jyh-Shing and Jang suggested an optimization of the FIS parameters through the use of ANN as a solution [38]. In this method, ANN promotes decision-making with a Takagi-Sugeno type “if, then” rule table. The linguistic expressions of a Sugeno type fuzzy model with two inputs as x and y are as follows [35–38]:

$$\begin{aligned} \text{if } x \text{ is } X_1 \text{ and } y \text{ is } Y_1 \text{ then } f_1 &= p_1 x + q_1 y + r_1, \\ \text{if } x \text{ is } X_2 \text{ and } y \text{ is } Y_2 \text{ then } f_2 &= p_2 x + q_2 y + r_2, \end{aligned} \quad (6)$$

where X_i and Y_i are the fuzzy sets; f_i is the output function; and p_i , q_i , and r_i are the design parameters determined at the training phase [35, 36].

The ANFIS model consists of 5 layers (Figure 4). The first one is the fuzzification layer. It determines the membership value of each input. The nodes in the input layer are expressed as follows:

$$o_i^1 = \mu_{X_i}(x), \quad \text{for } i = 1, 2. \quad (7)$$

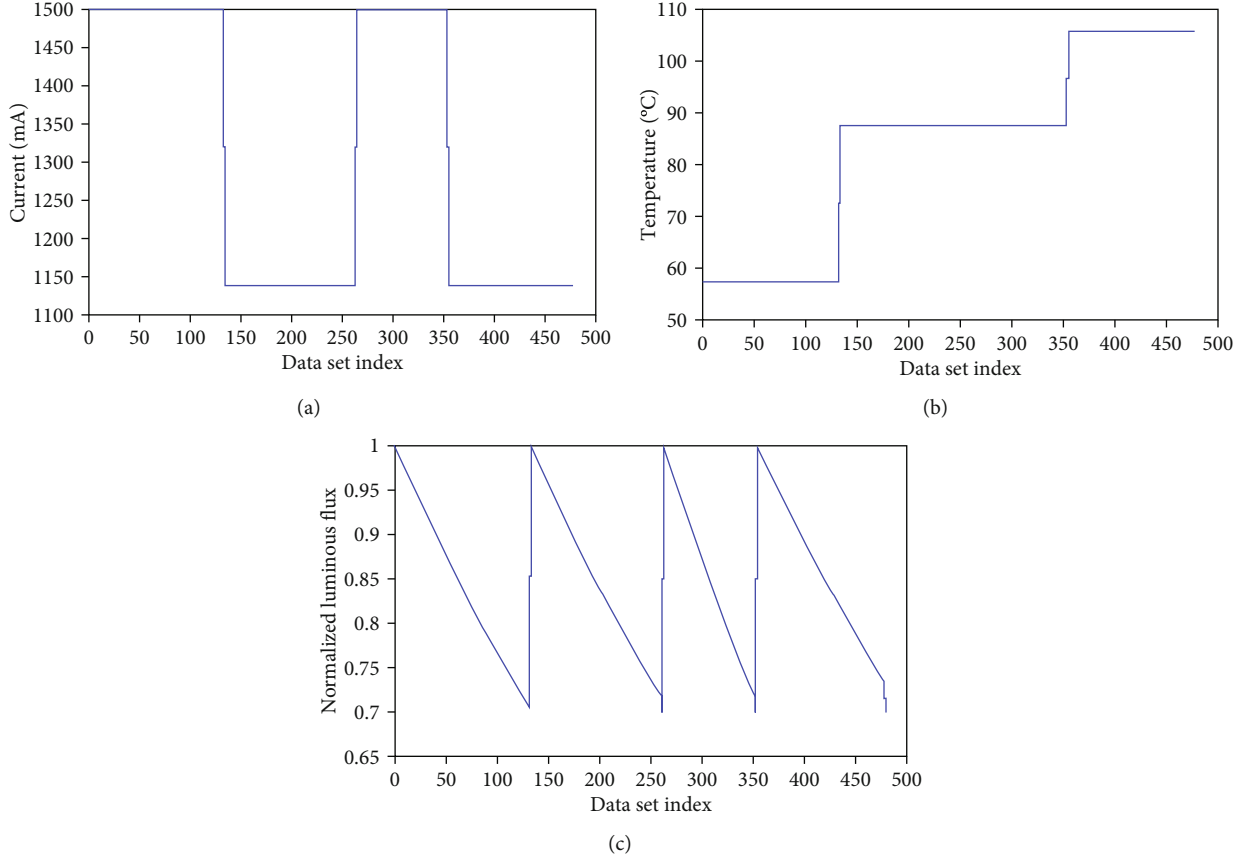


FIGURE 5: Inputs for ANFIS: (a) drive current, (b) operating temperature, and (c) normalized luminous flux.

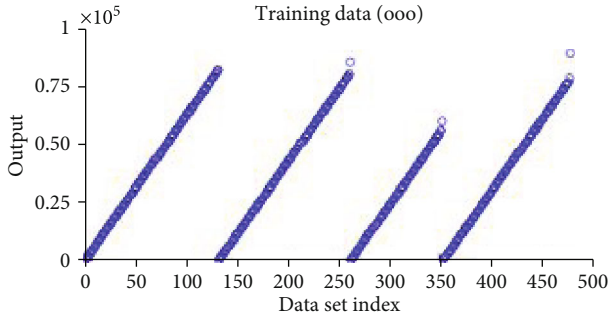


FIGURE 6: Training output data.

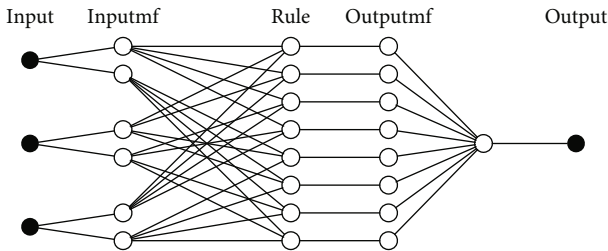


FIGURE 7: Proposed ANFIS model.

It is determined according to the selected membership function. It can be a triangle, a trapezoid, a bell, or a Gaussian curve [35–38].

The second layer provides the activation of the fuzzy rules, and it is where the data from the first layer is multiplied [35–38]:

$$o_i^2 = w_i = \mu_{X_i}(x) \times \mu_{Y_i}(y), \quad \text{for } i = 1, 2. \quad (8)$$

The third one is the normalization layer, and it provides the normalization of the firing strength of the fuzzy rules [35–38]:

$$o_i^3 = \bar{w}_i = \frac{w_i}{w_1 + w_2}, \quad \text{for } i = 1, 2. \quad (9)$$

The fourth layer is the defuzzification layer. It is obtained by multiplying the linear function or the constant determined for each rule through the normalized firing strength [35–38]:

$$o_i^4 = \bar{w}_i \times f_i = \bar{w}_i \times (p_i x + q_i y + r_i) \quad \text{for } i = 1, 2. \quad (10)$$

The fifth layer is where all outputs are summed [35–38]:

$$o_i^5 = \sum \bar{w}_i \times f_i, \quad \text{for } i = 1, 2. \quad (11)$$

ANFIS also has two adaptation layers. Adaptation is achieved during the training phase of ANFIS through the

TABLE 5: The best performance parameter of ANFIS models.

Model	Input membership function type	Number of membership function	Output membership function type	RMSE (training)	RMSE (testing)	R^2 (training)	R (testing)
Mdl 1	Triangle	6	Constant	352.556	412.875	0.9974	0.9952
Mdl 2	Gbell	6	Constant	935.428	914.820	0.9841	0.9827
Mdl 3	Gauss	7	Constant	1579.06	1513.185	0.9722	0.9705

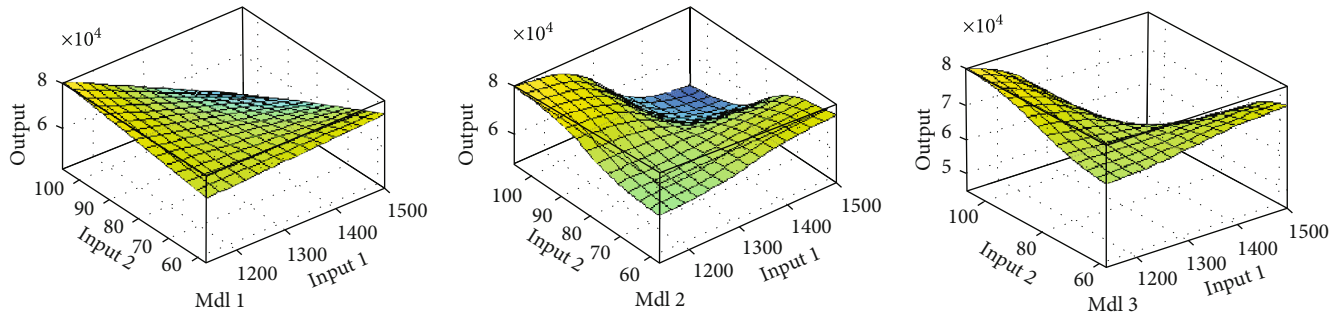


FIGURE 8: FIS surfaces of the proposed models.

TABLE 6: Mdl 1 output vs. LED chip lifetime.

Lifetime maintenance	1500 mA/57.3°C		1500 mA/87.5°C		1140 mA/87.4°C		1140 mA/105.5°C	
	Target	Output	Target	Output	Target	Output	Target	Output
L_{98}	4118.932	4068.596	2945.860	2888.466	4222.648	4152.667	4418.790	4338.818
L_{96}	8322.795	8266.483	5952.463	5895.363	8532.367	8460.271	8928.695	8848.185
L_{94}	12,615.171	12,558.250	9022.367	8969.501	12,932.822	12,864.213	13,533.553	13,458.395
L_{92}	16,999.856	16,947.078	12,158.298	12,113.163	17,427.922	17,367.747	18,237.447	18,172.865
L_{90}	21,480.923	21,436.299	15,363.154	15,328.740	22,021.820	21,974.300	23,044.732	22,995.184
L_{88}	26,062.690	26,029.396	18,640.035	18,618.718	26,718.959	26,687.450	27,960.055	27,929.081
L_{86}	30,749.799	30,730.022	21,992.257	21,985.717	31,524.090	31,510.932	32,988.384	32,978.486
L_{84}	35,547.200	35,541.990	25,423.360	25,432.472	36,442.292	36,448.670	38,135.037	38,147.498
L_{82}	40,460.214	40,469.309	28,937.143	28,961.850	41,479.016	41,504.773	43,405.717	43,440.420
L_{80}	45,494.532	45,516.185	32,537.699	32,576.859	46,640.114	46,683.552	48,806.551	48,861.767
L_{78}	50,656.343	50,687.008	36,229.418	36,280.652	51,931.890	51,989.501	54,344.129	54,416.229
L_{76}	55,952.231	55,986.395	40,017.038	40,076.544	57,361.111	57,427.428	60,025.557	60,108.836
L_{74}	61,389.370	61,419.204	43,905.687	43,968.023	62,935.171	63,002.231	65,858.507	65,944.794
L_{72}	66,975.459	66,990.551	47,900.875	47,958.705	68,661.942	68,719.204	71,851.283	71,929.528
L_{70}	72,718.941	70,875.766	52,008.574	50,741.645	74,550.044	72,705.949	78,012.892	76,103.018

adjustment of the prerequisite parameters in the first layer and the result parameters in the fourth. The Hybrid Learning Algorithm consists of two stages. In the forward pass, the prerequisite parameters remain constant, and the result parameters are defined according to the least squares method. In the backward pass, the result parameters are kept constant, error rates are back propagated, and the prerequisite parameters are adjusted with a gradual decrease [36, 37].

3. Experimental Results and Discussion

The white COB LED with the model number NVELJ048Z is manufactured by the Nichia Corporation. IES published a

standard IES LM-80-08 in 2008 to define the methodology of light output measurements for the LED light source. This is a practice widely accepted by the LED light source manufacturing and lighting industries. LEDs were tested at three different temperatures (55°C, 85°C, and 105°C) for 6000 hours [32].

The LM-80-08 test report for the white COB LED with model number NVELJ048Z, based on the measurements carried out in the Nichia Corporation LED Testing Laboratory, are presented in Table 3.

The requested lifetime L is generally not measured. The Illumination Engineers Society (IES) [38] assigns the measurement methods as per the industry norm IES

TABLE 7: Mdl 2 output vs. LED chip lifetime.

Lifetime maintenance	1500 mA/57.3 °C		1500 mA/87.5 °C		1140 mA/87.4 °C		1140 mA/105.5 °C	
	Target	Output	Target	Output	Target	Output	Target	Output
L_{98}	4118.932	3818.217	2945.860	2783.437	4222.648	4006.339	4418.790	4289.884
L_{96}	8322.795	7889.633	5952.463	5683.255	8532.367	8159.987	8928.695	8614.042
L_{94}	12,615.171	12,352.778	9022.367	8862.082	12,932.822	12,713.281	13,533.553	13,354.248
L_{92}	16,999.856	17,012.808	12,158.298	12,181.137	17,427.922	17,467.437	18,237.447	18,303.561
L_{90}	21,480.923	21,690.503	15,363.154	15,512.773	22,021.820	22,239.611	23,044.732	23,271.636
L_{88}	26,062.690	26,289.418	18,640.035	18,788.298	26,718.959	26,931.417	27,960.055	28,156.041
L_{86}	30,749.799	30,844.624	21,992.257	22,032.690	31,524.090	31,578.631	32,988.384	32,994.020
L_{84}	35,547.200	35,507.528	25,423.360	25,353.793	36,442.292	36,335.713	38,135.037	37,946.382
L_{82}	40,460.214	40,447.607	28,937.143	28,872.310	41,479.016	41,375.573	43,405.717	43,193.132
L_{80}	45,494.532	45,721.041	32,537.699	32,628.263	46,640.114	46,755.556	48,806.551	48,793.963
L_{78}	50,656.343	51,203.237	36,229.418	36,532.892	51,931.890	52,348.469	54,344.129	54,616.448
L_{76}	55,952.231	56,634.208	40,017.038	40,401.028	57,361.111	57,889.108	60,025.557	60,384.558
L_{74}	61,389.370	61,728.828	43,905.687	44,029.615	62,935.171	63,086.614	65,858.507	65,795.451
L_{72}	66,975.459	66,269.116	47,900.875	47,263.386	68,661.942	67,718.591	71,851.283	70,617.542
L_{70}	72,718.941	70,138.976	52,008.574	50,019.641	74,550.044	71,666.623	78,012.892	73,852.756

TABLE 8: Mdl 3 output vs. LED chip lifetime.

Lifetime maintenance	1500 mA/57.3 °C		1500 mA/87.5 °C		1140 mA/87.4 °C		1140 mA/105.5 °C	
	Target	Output	Target	Output	Target	Output	Target	Output
L_{98}	4118.932	4047.894	2945.860	2858.584	4222.648	4114.390	4418.790	4284.867
L_{96}	8322.795	7507.493	5952.463	5346.754	8532.367	7680.967	8928.695	8029.431
L_{94}	12,615.171	11,950.713	9022.367	8541.899	12,932.822	12,260.853	13,533.553	12,837.402
L_{92}	16,999.856	17,031.934	12,158.298	12,194.742	17,427.922	17,496.592	18,237.447	18,332.747
L_{90}	21,480.923	22,156.159	15,363.154	15,876.080	22,021.820	22,772.734	23,044.732	23,867.975
L_{88}	26,062.690	26,839.843	18,640.035	19,236.212	26,718.959	27,587.647	27,960.055	28,914.388
L_{86}	30,749.799	31,032.743	21,992.257	22,236.295	31,524.090	31,885.171	32,988.384	33,410.210
L_{84}	35,547.200	35,109.318	25,423.360	25,142.358	36,442.292	36,046.019	38,135.037	37,751.710
L_{82}	40,460.214	39,600.678	28,937.143	28,333.281	41,479.016	40,612.717	43,405.717	42,505.249
L_{80}	45,494.532	44,858.880	32,537.699	32,061.290	46,640.114	45,946.632	48,806.551	48,049.213
L_{78}	50,656.343	50,792.038	36,229.418	36,263.670	51,931.890	51,958.486	54,344.129	54,293.395
L_{76}	55,952.231	56,844.226	40,017.038	40,548.521	57,361.111	58,088.014	60,025.557	60,657.874
L_{74}	61,389.370	62,304.681	43,905.687	44,413.736	62,935.171	63,617.060	65,858.507	66,398.119
L_{72}	66,975.459	66,698.688	47,900.875	47,523.797	68,661.942	68,065.879	71,851.283	71,016.535
L_{70}	72,718.941	69,929.003	52,008.574	49,810.105	74,550.044	71,336.352	78,012.892	73,099.388

TABLE 9: Lifetime prediction (L_{70}).

Model type	Lifetime (hrs.)
Reference	76,216.842
Exponential function	73,860.280
Mdl 1	76,103.018
Mdl 2	73,852.756
Mdl 3	73,099.388

LM-80 [27]. It requires that the LED lamps are tested for at least 6000 hours with a sufficient number of samples and data. Many measurements are performed by LED producers and are under 10,000 hours. After that, the lifetime was estimated according to test report in the IES LM-80 with the exponential light exchange model as described by the standard IES TM-21 [32].

In this study, for the modeling of the ANFIS system, the light output maintenance values of the COB LED fixtures

were used. The required reference values for this were obtained from the relevant company report [27, 32]. Table 4 presents summary information on the current, temperature, luminous flux, and lifetime values of the tested LED fixtures.

As seen in Table 4, the designed ANFIS model had three input parameters: the current values, fixture temperature, and normalized luminous flux values of the COB LED fixtures (Figure 5). The drive current range was from 1.140 to 1.500 mA, whereas the temperature varied between 57.3°C and 105.50°C. Operating times corresponding to 98% to 70% of the initial luminous fluxes of COB LED fixtures constitute the output of the ANFIS model.

Of the total of 595×4 data, 479×4 were used for training and 118×4 for testing (Figure 6). A total of 6 (2 2 2) inputs, 2 fuzzy sets, and 8 rules were created for the first and second models. For the third model, a total of 7 (2 2 3) inputs and 2 fuzzy sets were used for the output, and 12 rules were created (Figure 7).

Inputs were fuzzified with the triangle, bell, and Gaussian membership functions, respectively (trimf, gbellmf, and gaussmf). Output membership function was selected as a “constant.” Models created with the hybrid learning algorithm were individually tested for all types of fuzzy sets. Table 5 shows the best obtained performance parameters.

FIS surfaces for the inputs and outputs of the models are presented in Figure 8.

When the models are compared, it is seen that the smallest RMSE value is obtained with Mdl 1 which used the triangular membership function. Bigger RMSE values were obtained in Mdl 3 and Mdl 2. For a better evaluation of the ANFIS model output values, the prediction times obtained with the values in Table 1 are provided in Tables 6–8.

4. Conclusion

Multiple factors affect the LED lifetime. Among them are LED’s operating time, temperature, and driving current. Differences are observed even in the same group of LED chips. An analysis of the results obtained shows that the LED lifetime decreases as the operating temperature increases. Nevertheless, an increase in the driving current at the same temperature reduces the LED lifetime. The remaining LED lifetime at the desired temperature and current values can be successfully predicted with the suggested ANFIS model. The aim of this study is to propose the new method which predicted the lifetime of high-power COB LED fixtures. In addition, this method can also be used in the life estimation of nanosensors and can be produced with 3D technology in the future. The data from Tables 6–8 can be summarized as follows:

- (i) For Mdl 1, according to Table 6, when the operating current increases by about 32%, the lifetime decreases by about 40.1%. Moreover, it was seen that in the same model, operating temperature increases of about 18% and 31% caused a decrease in the lifetime by about 4.1% and 39.1%, respectively

- (ii) For Mdl 2, according to Table 7, when the operating current increases by about 32%, the lifetime decreases by about 42.7%. Moreover, it was seen that in the same model, operating temperature increases of about 18% and 31% caused a decrease in the lifetime by about 4.4% and 40.9%, respectively

- (iii) For Mdl 3, according to Table 8, when the operating current increases by about 32%, the lifetime decreases by about 45.3%. Moreover, it was found that in the same model, operating temperature increases of about 18% and 31% caused a decrease in the lifetime by about 4.8% and 42.4%, respectively

Table 9 shows the L_{70} lifetime prediction values according to the obtained models. The product’s life expectancy (reference) value is 76216.842 hours in the catalog [32]. According to the classical calculation method (exponential function), the lifetime was found to be 73860.279 hours. Accordingly, the Mdl 1 results created with ANFIS was found to be close to the reference at the rate of 99.8506%. For Mdl 2, this value is 96.8982%; for Mdl 3, this value is 95.9097%. Consequently, it can be said that the most successful model is Mdl 1.

Data Availability

The dataset supporting the conclusions of this article are included within the article.

Conflicts of Interest

The authors declare that they have no conflicts of interest.

References

- [1] P. L. Tavares, J. M. S. Dutra, A. R. Silva et al., “Comparison of analytical method of flux density prediction for COB and discrete LED luminaires,” in *13th IEEE International Conference on Industry Applications*, pp. 487–494, Sao Paulo, Brasil, November 2018.
- [2] B. Sun, X. Fan, H. Ye et al., “A novel lifetime prediction for integrated LED lamps by electronic-thermal simulation,” *Reliability Engineering and System Safety*, vol. 163, pp. 14–21, 2017.
- [3] H.-H. Wu, K.-H. Lin, and S.-T. Lin, “A study on the heat dissipation of high power multi-chip COB LEDs,” *Microelectronics Journal*, vol. 43, no. 4, pp. 280–287, 2012.
- [4] K. İsmail, T. Vedat, and O. Bülent, “Modeling of dimmable High Power LED illumination distribution using ANFIS on the isolated area,” *Expert Systems with Applications*, vol. 38, no. 9, pp. 11843–11848, 2011.
- [5] S. H. Park and J. H. Kim, “Lifetime estimation of LED lamp using gamma process model,” *Microelectronics Reliability*, vol. 57, pp. 71–78, 2016.
- [6] F.-K. Wang and Y.-C. Lu, “Useful lifetime analysis for high-power white LEDs,” *Microelectronics Reliability*, vol. 54, no. 6-7, pp. 1307–1315, 2014.
- [7] H. Niu, S. Wang, X. Ye, H. Wang, and F. Blaabjerg, “Lifetime prediction of aluminum electrolytic capacitors in LED drivers

- considering parameter shifts,” *Microelectronics Reliability*, vol. 88–90, pp. 453–457, 2018.
- [8] H. Yang, B. Yang, J. Li, and P. Yang, “Failure analysis and reliability reinforcement on gold wire in high-power COB-LED under current and thermal shock combined loading,” *Applied Thermal Engineering*, vol. 150, pp. 1046–1053, 2019.
- [9] K. İsmail, “A study on the working performance of dimming methods for single and multi chip power LEDs,” *International Journal of Photoenergy*, vol. 6, no. 1, 8 pages, 2012.
- [10] D. Czyżewski, “Investigation of COB LED luminance distribution,” in *IEEE Lighting Conference of the Visegrad Countries (Lumen V4)*, pp. 1–4, Poland, 2016.
- [11] J. Fan, C. Xie, Q. Cheng, X. Fan, and G. Zhang, “Luminescence mechanism analysis on high power tunable color temperature chip-on-board white LED modules,” in *IEEE 18th International Conference on Thermal, Mechanical 1 and Multi-Physics Simulation and Experiments in Microelectronics and Microsystems*, pp. 1–6, Dresden, Germany, April 2017.
- [12] S.-H. Moon, Y.-W. Park, and H.-M. Yang, “A single unit cooling fins aluminum flat heat pipe for 100 W socket type COB LED lamp,” *Applied Thermal Engineering*, vol. 126, pp. 1164–1169, 2017.
- [13] İ. Kiyak, B. Oral, and V. Topuz, “Smart indoor LED lighting design powered by hybrid renewable energy systems,” *Energy and Buildings*, vol. 148, pp. 342–347, 2017.
- [14] V. Smirnov, V. Sergeev, A. Gavrikov, and A. Shorin, “Modulation method for measurement of thermal resistance of high-power COB LEDs,” in *IEEE 23 International Workshop on Thermal Investigations of ICs and Systems*, pp. 1–4, Amsterdam, Nederland, September 2017.
- [15] S.-P. Ying and W.-B. Shen, “Thermal analysis of high-power multichip COB light-emitting diodes with different chip sizes,” *IEEE Transactions on Electron Devices*, vol. 62, no. 3, pp. 896–901, 2015.
- [16] N. Vakrilov, A. Andonova, and N. Kafadarova, “Study of high power COB LED modules with respect to topology of chips,” in *IEEE 38. Int. Spring Seminar on Electronics Technology*, pp. 108–113, Hungary, May 2015.
- [17] G. Gökhan and K. İsmail, “The system design of photovoltaic supported light pipe LED hybrid illumination,” in *6. European Conference on Renewable Energy Systems ECRES 2018*, pp. 1079–1088, İstanbul, Turkey, June 2018.
- [18] F. He, Q. Chen, J. Liu, and J. Liu, “Thermal analysis of COB array soldered on heat sink,” *International Communications in Heat and Mass Transfer*, vol. 59, pp. 55–60, 2014.
- [19] D. Lee, H. Choi, S. Jeong et al., “A study on the measurement and prediction of LED junction temperature,” *International Journal of Heat and Mass Transfer*, vol. 127, pp. 1243–1252, 2018.
- [20] W. D. van Driel, M. Schuld, B. Jacobs, F. Commissaris, J. van der Eyden, and B. Hamon, “Lumen maintenance predictions for LED packages,” *Microelectronics Reliability*, vol. 62, pp. 39–44, 2016.
- [21] M. Cai, D. Yang, K. Tian et al., “A hybrid prediction method on luminous flux maintenance of high-power LED lamps,” *Applied Thermal Engineering*, vol. 95, pp. 482–490, 2016.
- [22] X. Qu, Q. Liu, H. Wang, and F. Blaabjerg, “System-level lifetime prediction for LED lighting applications considering thermal coupling between LED sources and drivers,” *IEEE Journal of Emerging and Selected Topics in Power Electronics*, vol. 6, no. 4, pp. 1860–1870, 2018.
- [23] Q. Xiaohui, H. Wang, X. Zhan, F. Blaabjerg, and H. S.-H. Chung, “A lifetime prediction method for LEDs considering mission profiles,” in *IEEE Applied Power Electronics Conference and Exposition (APEC)*, pp. 2154–2160, USA, March 2016.
- [24] X. P. Li, L. Chen, and M. Chen, “An approach of LED lamp system lifetime prediction,” in *IEEE International Conference on Quality and Reliability*, pp. 110–114, Bangkok, Thailand, Sept. 2011.
- [25] Q. Chen, Q. Chen, and X. Luo, “Fast estimation of LED’s accelerated lifetime by online test method,” in *IEEE 64th Electronic Components and Technology Conference (ECTC)*, pp. 1992–1995, FL, USA, May 2014.
- [26] R. Zhang, C. Zhang, D. Liu, M. Zhao, J. Huang, and L. Xu, “Lifetime evaluation methods for LED products,” in *IEEE 17th International Conference on Thermal, Mechanical and Multi-Physics Simulation and Experiments in Microelectronics and Microsystems*, pp. 1–5, Montpellier, France, April 2016.
- [27] H. Liu, D. Yu, P. Niu et al., “Lifetime prediction of a multi-chip high-power LED light source based on artificial neural networks,” *Results in Physics*, vol. 12, pp. 361–367, 2019.
- [28] A. O. Alfarg, X. QuI, H. Wang, F. Blaabjerg, and Z. Li, “Lifetime prediction of LED lighting systems considering thermal coupling between LED sources and drivers,” in *IECON 2017-43rd Annual Conference of the IEEE Industrial Electronics Society*, pp. 1273–1278, Beijing, China, Nov. 2017.
- [29] F.-K. Wang and T.-P. Chu, “Lifetime predictions of LED-based light bars by accelerated degradation test,” *Microelectronics Reliability*, vol. 52, no. 7, pp. 1332–1336, 2012.
- [30] J. Hao, D. Li, C. He, Q. Sun, and H. Ke, “Step-down accelerated aging test for LED lamps based on Nelson models,” *Optik*, vol. 149, pp. 69–80, 2017.
- [31] B. Tahsin and K. İsmail, “COB LED’lerde Yaşlandırma ve Ömür Tahmini Analizi,” *Kırklareli University Journal of Engineering and Science*, vol. 4, pp. 153–162, 2018.
- [32] Nichia Corporation, “LED Testing Laboratory, COB-Z LM-80 Test Report,” 2019, http://www.tdelektronik.com/s/uploads/documents/2612018YGA1SFyFFvugCH1_06dfF-CrsDB_vByE.pdf.
- [33] M. Hodapp, *IESNA LM-80 and TM-21*, Philips Lumileds Press, Street Lighting Consortium & Workshop, Florida, USA, 2015.
- [34] Energy Star®, “TM-21 Calculator for Uneven LM-80 Intervals,” 2019, https://www.energystar.gov/sites/default/files/ENERGY%20STAR%20TM-21%20Calculator%20for%20Uneven%20Test%20Intervals%20rev%202015_0.xlsx.
- [35] M. Şahin and R. Erol, “Prediction of attendance demand in European football games: comparison of ANFIS, Fuzzy Logic, and ANN,” *Computational Intelligence and Neuroscience*, vol. 2018, Article ID 5714872, 14 pages, 2018.
- [36] M. Guzel, I. Kok, D. Akay, and S. Ozdemir, “ANFIS and Deep Learning based missing sensor data prediction in IoT,” in *Concurrency Computation Practice and Experience*, pp. 1–15, Wiley Online Library, 2019.
- [37] R. J. Jyh-Shing, “ANFIS: adaptive-network based fuzzy inference system,” *IEEE Transactions On Systems, Man, and Cybernetics*, vol. 23, no. 3, pp. 665–685, 1993.
- [38] M. Yucel, F. V. Celebi, M. Torun, and H. H. Goktas, “Adaptive neuro-fuzzy based gain controller for erbium-doped fiber amplifiers,” *Advances in Electrical and Computer Engineering*, vol. 17, no. 1, pp. 15–20, 2017.

Research Article

Design and Analysis of a Laminar Diffusion-Based Micromixer with Microfluidic Chip

Osman Ulkir ¹, Oguz Girit ², and Ishak Ertugrul ³

¹Department of Electronics and Automation, Mus Alparslan University, Mus 49100, Turkey

²Department of Machine Engineering, Marmara University, Istanbul 34100, Turkey

³Department of Mechatronics, Mus Alparslan University, Mus 49100, Turkey

Correspondence should be addressed to Osman Ulkir; o.ulkir@alparslan.edu.tr

Received 1 November 2020; Revised 10 December 2020; Accepted 24 December 2020; Published 2 January 2021

Academic Editor: Pooyan Makvandi

Copyright © 2021 Osman Ulkir et al. This is an open access article distributed under the Creative Commons Attribution License, which permits unrestricted use, distribution, and reproduction in any medium, provided the original work is properly cited.

This study aims to perform optimization to achieve the best diffusion control between the channels by designing and analysing a microfluidic-based micromixer. The design and analysis of the micromixer were made with the COMSOL Multiphysics program. Some input and output parameters must be defined for diffusion control of the micromixer. Among these parameters, inputs are the diffusion coefficient and inlet flow rate, while outputs are velocity, pressure, and concentration. Each input parameter in the microfluidic chip affects the output of the system. To make the diffusion control in the most optimum way, the data were obtained by making much analysis. The data obtained from this program was also provided with the Fuzzy Logic method to optimize the microfluidic chip. The diffusion coefficient value ($5E-11 \text{ m}^2/\text{s}$) should be given to the channels to achieve the optimum diffusion between the micromixer channels, if the inlet flow rate value ($15E-15 \text{ m}^3/\text{s}$) is the output value of the system, the velocity is 0.09 mm/s . The pressure is 2 Pa , and the concentration is 0.45 mol/m^3 . These values are the optimum values obtained from the analysis without damaging the liquid's microfluidic channels supplied to the micromixer's inlet.

1. Introduction

Microfluidic devices are the technology that allows us to manipulate and process small amounts of liquid using channels several micrometers long. The microfluidics field uses fabrication technologies developed by the microelectronics and microelectromechanical system (MEMS) industry [1, 2]. It provides outstanding advantages over macroscale instruments such as better sensitivity and higher resolution in separation and detection, batch production, faster analysis, and lower sample consumption. Thanks to these advantages, such devices are recognized as a promising option for miniaturization in the field of environmental and defense monitoring, chemical synthesis, and biomedical applications [3–5]. Stirring of samples in such applications is considered a significant part of microfluidic systems. In these systems, mixing becomes one of the critical points for the success of chemical reactions. Rapid mixing at microscale sizes has been a difficult problem in many applications. For this reason, micromixers have become an essential part of microfluidic systems.

Microfluidics integrates various subcomponents such as pumps, micromixers, reactors, and dilution chambers [6, 7]. Therefore, the study of microscale (i.e., microfluids) fluid flow has become central to the development of the respective devices. Micromixers are often vital components for microfluidic chip devices, as they are required for chemical applications, biological applications, and detection/analysis of chemical or biochemical content [8–10]. In the past, the importance of micromixers was poorly understood, and only a few research groups focused on this area [11, 12]. Recently, many new micromixer studies have been published [13–17]. Saygili et al. produced microfluidic molds using the 3D printing method. They observed mixing on different microplatforms with and without mixer geometry to understand the underlying diffusion mechanism that causes mixing in the microchannel [18]. Rasouli and Tabrizian proposed an energy-efficient acoustic platform based on the boundary-oriented acoustic flow that provides the rapid mixing required controlling nanoprecipitation [19]. The device encompasses vibrating bubbles and sharp edges in the microchannel to convert acoustic energy into

powerful vortices fluid movements. Dehghani et al. sought to increase microfluidics' mixing using a micromixer with a passive method [20]. Du et al. used an AC field-effect flow control in induced charged electroosmotic (ICEO) to develop an electrokinetic micromixer with 3D electrode layouts [21]. Nan et al. have also dealt with micromixers in general reviews on micrototal analysis systems (microTAS) [22]. In this study, different from other studies, diffusion control of the micromixer designed and analyzed using COMSOL Multiphysics program was performed. The optimization of this control process was done using the fuzzy logic method. The necessary input parameters for this method, which works without mathematical modeling, were determined as a result of the analysis. The Fuzzy logic, which has been preferred in many fields for years [23–25], will be used for the first time to optimize the micromixer.

In microfluidic devices, the channel's size is microscale, and therefore the flow velocity is minimal. The Reynolds number, defined as the inertia force ratio to viscous force, indicates whether the fluid flow is turbulent or laminar [26]. When the dimensions are microscale, a Reynolds number of less than one indicates that the flow behavior is viscous. Because the flow's nature is laminar, the fluid flows in parallel layers without interruption between layers. The mixing of fluids is mainly dependent on diffusion with a very low mixing efficiency. For example, in a water-based microfluidic system (2 kg/m^3 liquid density and 0.001 Ns/m^2 viscosity) with a channel width of $200 \mu\text{m}$ and a flow rate of $2 \mu\text{L/s}$, the Reynolds number is 0.1 and the fluids spread is 2 s and 2 mm for $2 \mu\text{m}$ for 2000 seconds. Therefore, it is imperative to develop different micromixers to increase mixing efficiency in the development of microfluidic systems. There are different types of micromixers categorized as passive micromixer and active micromixer [27, 28]. An active micromixer is where mixing is provided by external input energy [29]. The passive micromixer has no external energy source or moving parts, and therefore mixing is achieved by the geometry of their structure [30, 31]. Most passive micromixers provide high mixing efficiency at a low flow rate [32, 33]. Because of this simple concept, passive micromixers are often preferred to integrate microfluidic devices [34, 35]. In this study, microfluidic modeling has been done by using a passive micromixer.

This article proposes a simple model for controlled mixing by diffusion where two different laminar streams are in contact for a specific controlled time. The micromixer model was designed using the COMSOL Multiphysics program. The input parameters applied in this program's analysis process were the diffusion coefficient and inlet flow rate, while the output parameters were determined as velocity, pressure, and concentration. As a result of the analysis, diffusion control of fluids in the microchannel was performed using the fuzzy logic method. As a result, by controlling the inlet flow rate and the diffusion coefficient of the fluids, it has been observed that it is possible to control the concentration, pressure, and velocity of the species transported from one stream to another diffusion.

2. Materials and Methods

In this study, the design of the microfluidic-based micromixer was realized with COMSOL Multiphysics software.

To apply diffusion control in the best way, attention has been paid to designing the channels in the micromixer. As a result of dozens of different analyses made with this software, the diffusion coefficient and flow rate of two different laminar flows entering the micromixer channels were determined as input data. Pressure, velocity, and concentration values were obtained by changing these data. The optimization of the data obtained from the analysis was done using the fuzzy logic method. In this section, the micromixer design, analysis, and optimization processes will be explained in detail.

2.1. Design of Micromixer. The geometry of the micromixer has a size in the order of microscale. The micromixer consists of a single microchannel with two inputs and two outputs. The width of the micromixer is determined as $150 \mu\text{m}$ and the height as $100 \mu\text{m}$. The developed model is based on the controlled diffusion micromixer model, which is assumed to be the fluid creeping flow. Creeping flow refers to fluid flow dominated by viscosity with a low Reynolds number; therefore, inertial forces can be neglected. This makes the flow more suitable for micromixer simulation than the laminar flow assumption. The geometry of the device is shown in Figure 1. The device is divided into two parts due to its symmetrical geometry. The design is aimed at preserving a laminar flow area when two different fluids are combined, thus, preventing uncontrolled convective mixing. Transport of species between these fluids must be carried out solely by diffusion so that species with low diffusion coefficients remain in the respective streams. Both compounds diffuse into the water flow in different amounts depending on their diffusion coefficient.

The flow rate at the inlet is about 0.1 mm/s . The Reynolds number significant for characterizing the flow is given by:

$$\text{Re} = \frac{\rho UL}{\mu} = 0.001. \quad (1)$$

ρ is the liquid density (kg/m^3), U is the characteristic velocity of the flow, μ is the liquid viscosity ($1 \text{ mPa}\cdot\text{s}$), and L is a characteristic dimension of the device ($150 \mu\text{m}$). When the Reynolds number is significantly less than 1 in this model, the creeping flow interface can be used. The convective term in the Navier-Stokes equations can be removed by dropping the incompressible Stokes equations:

$$\begin{aligned} \nabla \left(-pI + \mu \left(\nabla u + (\nabla u)^T \right) \right) &= 0, \\ \nabla \cdot u &= 0. \end{aligned} \quad (2)$$

U is the local velocity (m/s), and p is the pressure (Pa).

Mixing in the instrument is performed with relatively low concentrations of the species compared to the solvent. In this case, the mixture should contain water. This means that solute molecules only interact with water molecules, and Fick's law can describe diffusive transport. The mass balance equation for dissolved matter is as follows:

$$-\nabla \cdot (-D\nabla c + cu) = 0. \quad (3)$$

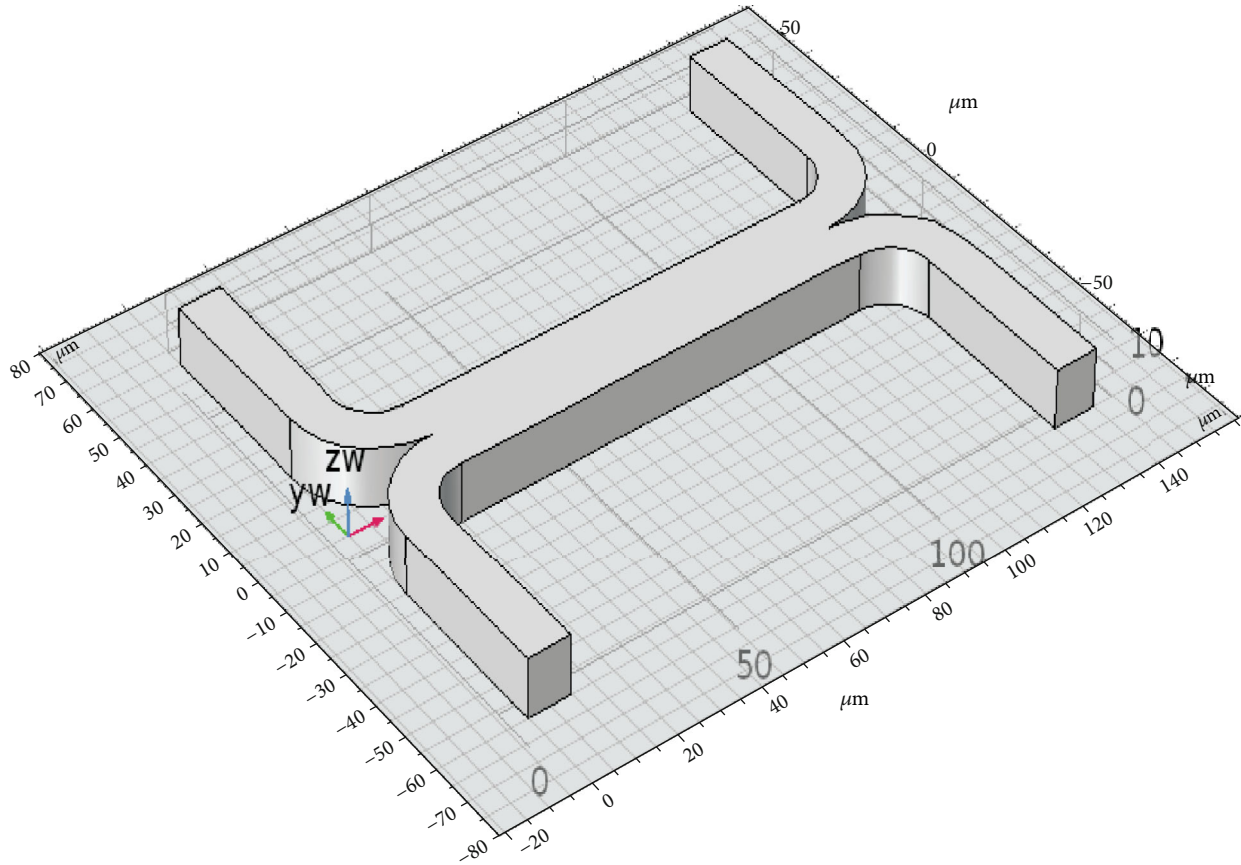


FIGURE 1: Micromixer model geometry.

In this equation, D is the diffusion coefficient of the solute (m^2/s), and c is the concentration (mol/m^3). Another dimensionless number can characterize standard streams: The Peclet number is given as:

$$\text{Pe} = \frac{LU}{D} \quad (4)$$

In this model, the parametric solver is used to solve Equation (1) for three different types, each with different D values: $D: 1 \times 10^{-11} \text{ m}^2/\text{s}$ and $1 \times 10^{-10} \text{ m}^2/\text{s}$. These D values correspond to the Peclet numbers of 100, 20, and 10, respectively. Since these Peclet numbers are all greater than 1, numerical stabilization is required when solving the Fick equation, as a cell significantly more extensive than 1 expresses the Peclet number.

Two versions of the model have been solved:

- (i) In the first version, it is assumed that a change in solute concentration does not affect the liquid's density and viscosity. This means that it is possible to solve the Navier-Stokes equations and then solve the mass balance equation
- (ii) In the second version, viscosity is quadratically dependent on concentration:

$$\mu = \mu_0(1 + ac^2). \quad (5)$$

In this equation, a is the constant of the size m^3/mol^2 , and μ_0 is the viscosity at zero concentration. Such a relationship between concentration and viscosity is often observed in solutions of larger molecules.

2.2. Analysis of Micromixer. The micromixer model processes an H-shaped microfluidic device for controlled mixing by diffusion. The device brings two different laminar streams into contact for a controlled time. The contact surface is well defined, and by controlling the flow rate, it is possible to control the number of species transferred from one stream to another by diffusion. The diagram of the microfluidic-based micromixer two input and two output devices to be analyzed is shown in Figure 2.

The purpose of the design is to avoid convective mixing by preserving the laminar flow area when two flows converge along with inlet A and inlet B, respectively, and the fluid flow is defined as creeping flow due to Reynolds number. The different species concentrations will be injected into the micromixer from inlet A and inlet B. The transport of the species between streams A and B must be done by diffusion so that the low diffusion coefficient species remain in their respective streams. The analysis process of the micromixer

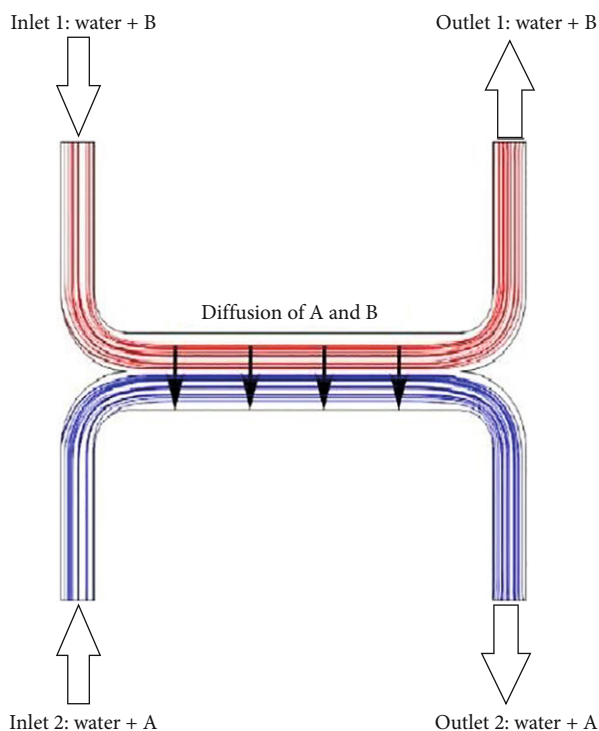


FIGURE 2: Diagram of the micromixer device.

using COMSOL Multiphysics will be explained in this section.

After the design process is completed, some parameters and definitions should be made to the system. The diffusion coefficients and inlet flow rate ratio of A and B fluids entering the channels are significant for diffusion control. These parameters must be defined as variable input during the analysis process.

In this study, the designed micromixer was loaded into the COMSOL program, and the necessary parameters were defined in the program. We use the program's fluid flow and chemical type transport module to simulate the geometric model. Some of the parameters specified in the system are fixed, and some are variable. The system's input and output parameters are variable since optimization will be made with the fuzzy logic method. While the input parameters used in the analysis process were diffusion coefficient and inlet flow rate, the output parameters were determined as concentration, pressure, and velocity.

The Reynolds number was determined as 0.001 to provide the laminar flow area of the A and B fluids, which are given as input to the micromixer channel. This number is vital to prevent convective interference. Another critical parameter is the diffusion coefficient. Choosing these coefficients low is essential for successful diffusion control. In this study, the diffusion coefficient for A and B was entered between $5\text{E}-11\text{ m}^2/\text{s}$. The inlet flow rate has been entered as $10\text{E}-15\text{ m}^3/\text{s}$.

Analysis of the microfluidic-based micromixer is required for the optimization process. The problem of the system must be well understood to perform analysis operations. Data will be obtained according to the analysis results made on the specified input and output parameters. The optimization process

will be carried out with the help of these data. The analysis process took much time because the input and output parameters were not fixed numbers in the system. Dozens of different analyses were performed in the COMSOL program, and optimum values were obtained for the micromixer model.

2.3. Optimization with Fuzzy Logic. The claim that classical logic is insufficient to meet both right and wrong and neither right nor wrong at the same time because it is based on a two-valued system that is thought to see everything as right or wrong has led to the development of precious and fuzzy logic systems [36, 37]. Fuzzy logic is the extraction of result values with the help of certain mathematical functions, depending on each rule that it will create, by processing the values obtained with specific algorithms using the result of experiences and data of people. Fuzzy logic is not based on Aristotelian (classical) logic but uses functions expressing fuzzy sets. There is a binary value (0-1) logic in classical logic [38]. Fuzzy logic derives results by considering binary values and expresses them with verbal variables such as less, less, more, medium, long, and regular. It allows processing with intermediate values (such as 0.3 and 0.92) instead of 0-1 values. It adds the ability to generalize by carrying two valuable memberships to multipreciousness. In this method, uncertainties in the system can be expressed. It is also a suitable method for systems whose mathematical model is complex and challenging [39].

The fundamental elements that make up the fuzzy logic method are inputs, outputs, fuzzification, rules, and defuzzification (Figure 3). The fuzzification unit maps measured inputs, which can be net values, to ambiguous linguistic values using the fuzzy reasoning mechanism. The step after fuzzification consists of two parts. These are fuzzy rule base and fuzzy inference. The fuzzy rule base provides the necessary definitions to describe linguistic control rules and fuzzy data manipulation in a fuzzy logic method. The Fuzzy Inference unit is the fuzzy reasoning mechanism that performs various fuzzy logic operations to understand the control action for a given fuzzy input. Based on fuzzy concepts, humans can simulate decision making and derive fuzzy control actions using inference rules in fuzzy logic. Defuzzification is a scale mapping that converts output variables into discourse universes corresponding to the value range. A unit provides a blur-free control action from an uncertain control action. As a result, fuzzy outputs are made available in real-time systems [40, 41].

The first step of system modeling with the fuzzy logic method is determining the input and output variables to be applied. The most important task of the microfluidic-based micromixer modeled in this study is to perform diffusion control of A and B fluids in the channels. To achieve this, attention must be paid to the diffusion-related fuzzy logic method's output parameters, and the rules should be written clearly. In this study, optimization processes are made according to input and output parameters using the Matlab-Fuzzy Logic program. The system's input parameters are defined as the diffusion coefficient and inlet flow rate of A and B fluids entering the micromixer. The output parameters of the system are determined as velocity, pressure, and concentration of the liquids. Diffusion coefficient values allow the diffusion of A

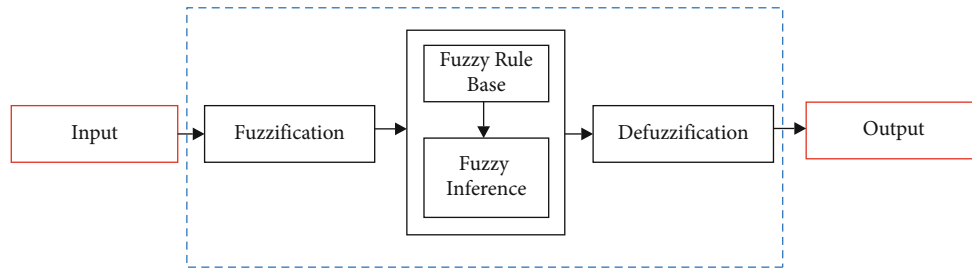


FIGURE 3: The basic structure of the fuzzy logic controller.

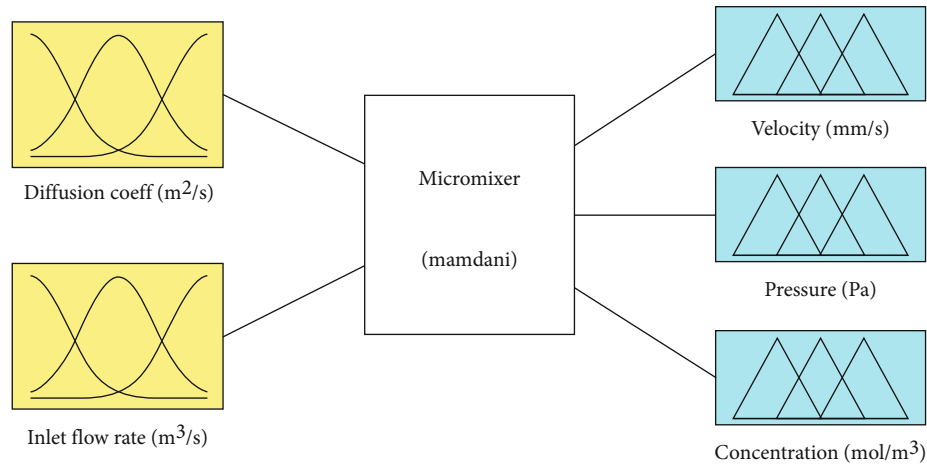


FIGURE 4: Fuzzy logic model of the micromixer.

and B liquids to occur. The inlet flow rate ratio of liquids also affects the fluids' pressure and outlet velocity in the micromixer channel. The inputs and outputs of the fuzzy logic system are shown in Figure 4.

In the fuzzy logic method, the membership function values written for each input and output value are adjusted according to the values of the upper and lower limits of the input and output parameters. Dozens of different analysis processes were carried out with the COMSOL Multiphysics program. Rules and parameter values were determined according to the analysis results. After selecting the upper and lower limits for modeling the necessary parameters with the membership function, a total of 9 rules were created to define the relationship between these parameters. This rule table is shown below (Table 1).

In the triangular membership function used for diffusion coefficient input, "LOW" for values in the range [1–3], "MIDDLE" for values in the range [3–7], and "HIGH" for values in the range of [7–10] were used. In the triangle membership function used for inlet flow rate input, "LOW" for values in the range of [1–10 m³/s], "MIDDLE" for values in the range of [10–20 m³/s], and "HIGH" for values in the range of [20–30 m³/s] were used. In the triangle membership function used for velocity output, "LOW" for values in the range of [0–0.06 mm/s], "MIDDLE" for values in the range of [0.06–0.12 mm/s], and "HIGH" for values in the range of [0.12–0.2 mm/s] were used. In the triangle membership func-

TABLE 1: Fuzzy logic rules.

	Inputs			Outputs		
	Diffusion coeff	Inlet flow rate		Velocity	Pressure	Concentration
1	L	L	THEN	L	L	BD-1
2	L	MD	THEN	MD	MD	BD-1
3	L	HG	THEN	HG	HG	BD-1
4	MD	L	THEN	L	L	GOOD
5	MD	MD	THEN	MD	MD	GOOD
6	MD	HG	THEN	HG	HG	GOOD
7	HG	L	THEN	L	L	BD-2
8	HG	MD	THEN	MD	MD	BD-2
9	HG	HG	THEN	HG	HG	BD-2

L: LOW, MD: MIDDLE, HG: HIGH, BD-1: BAD, GD: GOOD, BD-2: BAD.

tion used for pressure output, "LOW" for values in the range of [0–1 Pa], "MIDDLE" for values in the range of [1–3 Pa], and "HIGH" for values in the range of [3–4 Pa] were used. In the triangular membership function used for concentration output, "BD-1" for values in the range [0–0.3], "GOOD" for values in the range [0.3–0.6], and "BD-2" for values in the range [0.6–1] were used.

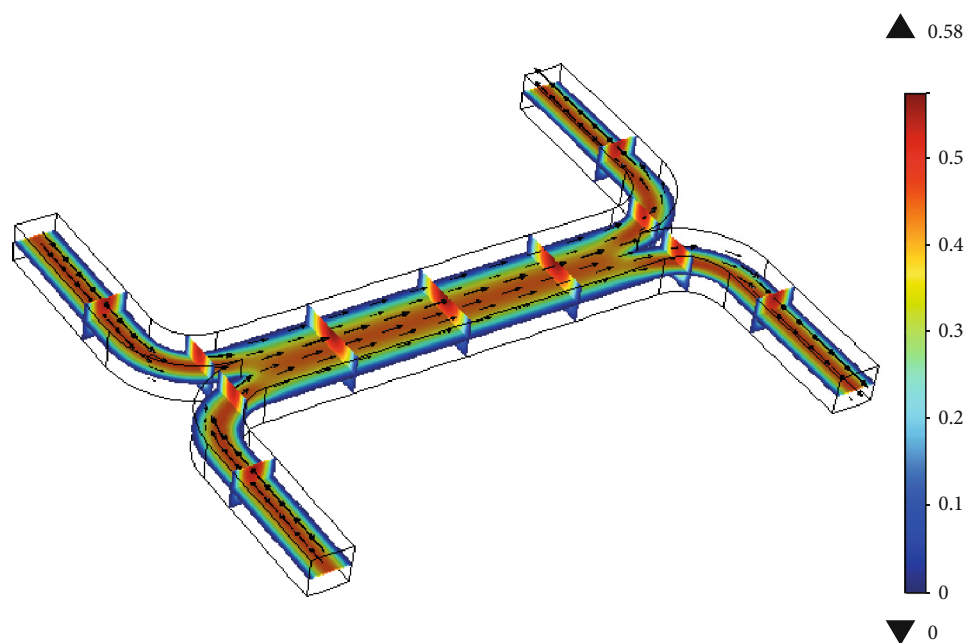


FIGURE 5: Velocity magnitude on the channel.

3. Results and Discussions

3.1. COMSOL Analysis Results. Analyses of the microfluidic-based micromixer device were performed using the COMSOL Multiphysics program. Fifty different analyses were performed to achieve optimum results for the device. The system's input variables are the diffusion coefficient and inlet flow rate, while the outputs are velocity, pressure, and concentration. According to the analysis results, the liquid type's diffusion coefficient used in the micromixer for diffusion control should be optimum $5\text{E-}11\text{ m}^2/\text{s}$, and the inlet flow rate of the liquid should be $15\text{E-}15\text{ m}^3/\text{s}$. When these input parameters are applied to the micromixer device, it is understood that the velocity in the output channel is 0.09 mm/s , the pressure is 2 Pa , and the concentration is 0.45 mol/m^3 .

The velocity field is shown in Figure 5 for the case where viscosity is independent of concentration. The flow is symmetrical and is not affected by the concentration area. The arrow volume plot is used to visualize the flow direction. The color in the figure shows the respective values. The highest velocity value measured along the channel is 0.58 mm/s .

Figure 6 shows the corresponding pressure distribution in the channel walls resulting from the flow. It indicates that the pressure at the inlets is very high compared to the outlets required to drive the fluid through the system. As the liquid passes through the guided channel of the micromixer, the pressure decreases. The highest pressure measured in micromixer channels is 8.03 Pa .

The effect of the diffusion coefficient on species concentration is shown in Figure 7. Mixing for A and B liquid types is almost perfect for the diffusion coefficient chosen. The concentration ratio is equal to 0.45 mol/m^3 for these species. As a result of the analysis, it clearly shows that the micromixer device can be used to separate lighter molecules from

heavier ones. By placing some of these devices in series, a high degree of separation can be achieved.

It has been observed that the species with the smallest diffusion coefficient do not undergo any significant mixing between both streams, and the mixture is almost perfect as the species with the largest diffusion coefficient. Therefore, it can be concluded that the concentration of the species depends on the diffusion coefficient of the molecule. Therefore, this micromixer can be used to separate types with different diffusion coefficients, i.e., lighter molecules from heavier ones, if multiple stages of this device are arranged in series.

3.2. Fuzzy Logic Results. As a result of the COMSOL Multiphysics program analysis, a large amount of data was obtained. Using these data, the optimization of the microfluidic-based micromixer has been made. The optimization process was carried out with the method of fuzzy logic using the Matlab program. Input and output parameters used for this method are described in Section 2.3. The micromixer device is designed to have two input and three output variables. After determining the lower-upper values for each variable parameter with the membership function, a total of 9 rules were created to define the relationship between the parameters. These rules determined by applying the Min-Max operator are shown in 3-dimensional graphs in Figure 8. These figures show the relationship between input and output parameters.

The inlet flow rate affects the micromixer's velocity and pressure in direct proportion (Figures 8(a) and 8(b)). The diffusion coefficient input value has less effect on the velocity and pressure of the mixer. After about $20\text{ m}^3/\text{s}$, inlet flow rate, pressure, and velocity values have increased significantly. While the maximum pressure acting along the channel in the micromixer is 3 Pa , the maximum velocity has been determined as 0.15 mm/s . The result of the fuzzy logic model

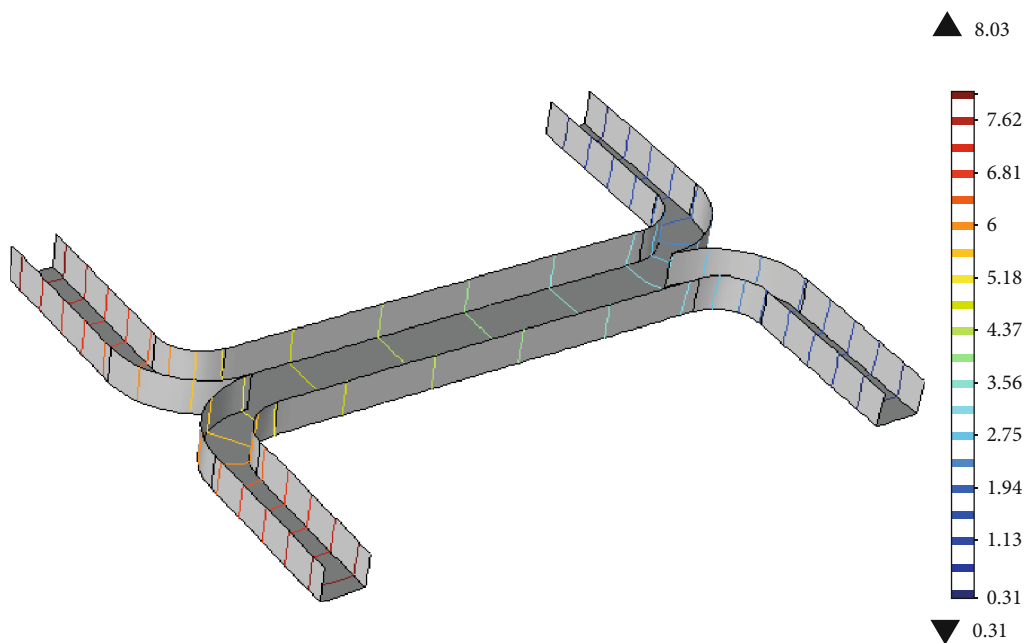


FIGURE 6: Pressure distribution on the channel walls.

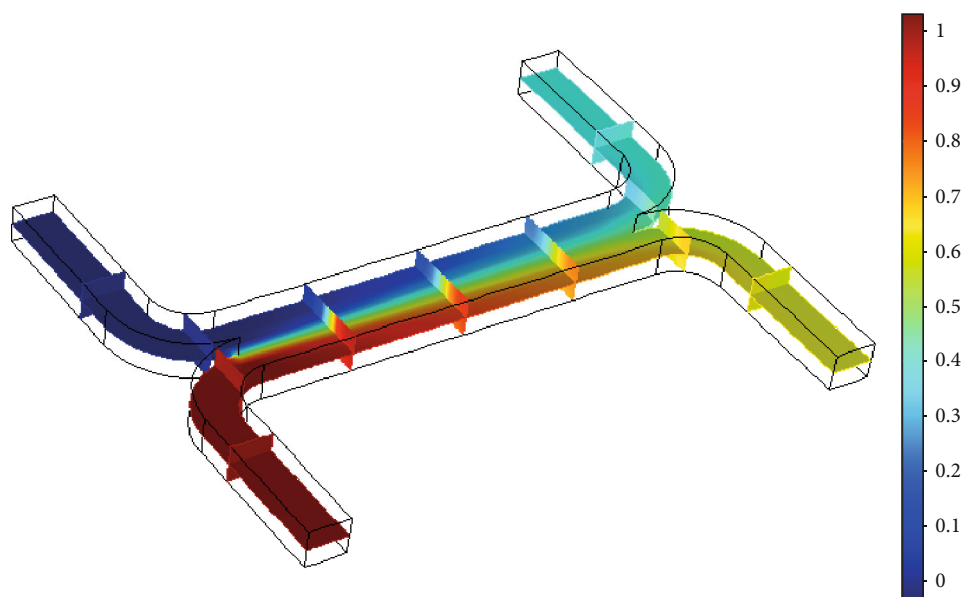


FIGURE 7: Concentration distribution for a species with diffusivity.

developed to perform diffusion control of two different types of liquid in the micromixer channels is shown in Figure 8(c). In this model, the effect of the liquid species' diffusion coefficient in the concentration process is high. The success rate in the concentration process increased after the $5\text{E-}11\text{ m}^2/\text{s}$ coefficient value. The change in the inlet flow rate was less significant. If liquids with a very low diffusion coefficient are supplied to the micromixer device, the concentration does not occur, and diffusion control cannot be achieved. The change in the output parameters obtained in response

to the input variables applied to the liquids entering the micromixer channel is shown in Table 2.

4. Conclusions

In this study, the design and analysis of a microfluidic-based micromixer device has been designed and optimized to achieve the best diffusion control between the channels. The data obtained from the analysis were classified in Fuzzy Logic, and optimization processes were made. The system's

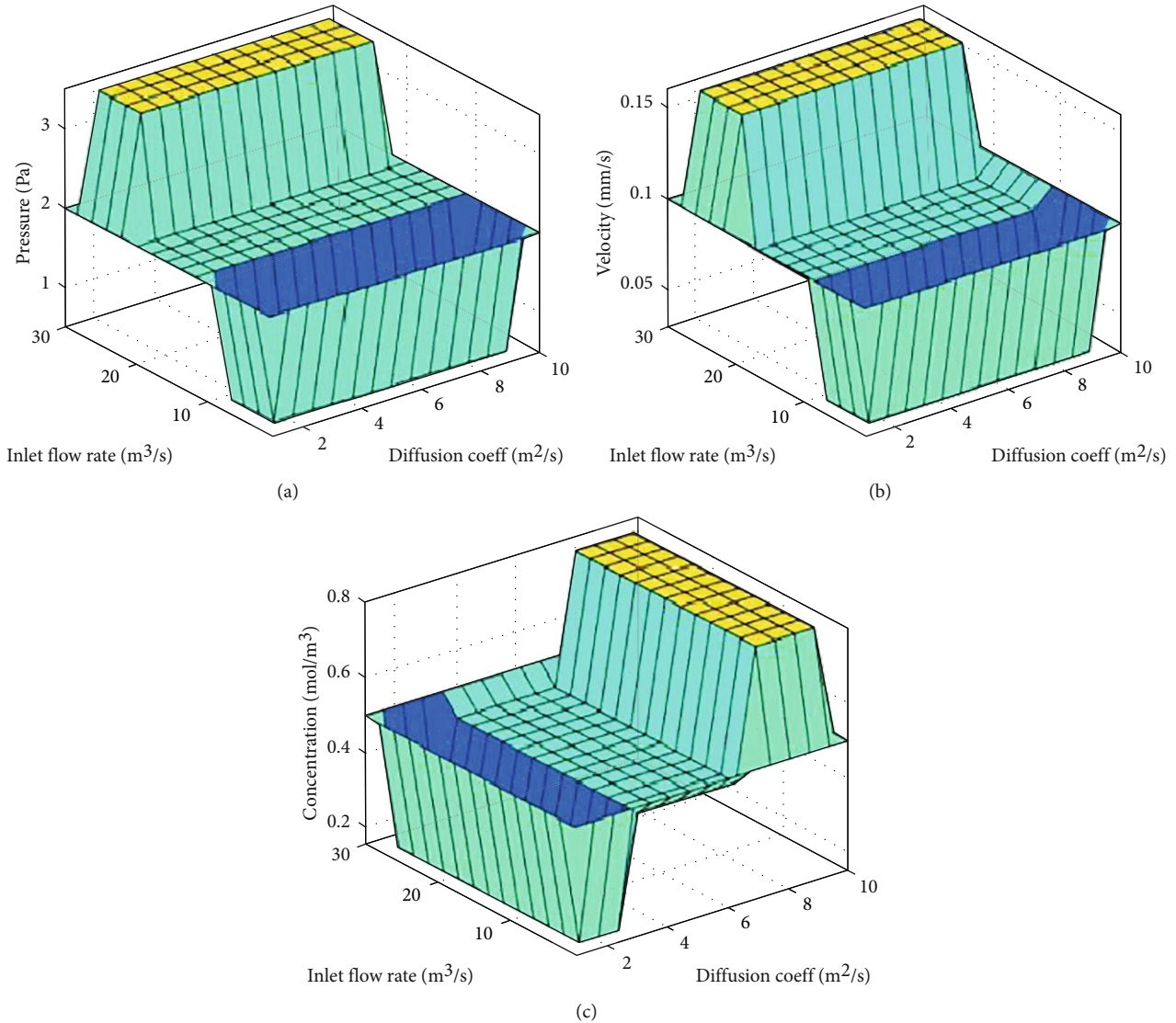


FIGURE 8: (a) Inlet flow rate and diffusion coefficient affect the pressure. (b) Inlet flow rate and diffusion coefficient affect the velocity. (c) Inlet flow rate and diffusion coefficient affect the concentration.

TABLE 2: Fuzzy logic outputs in response to the inputs.

Inputs		Outputs		
Diffusion coeff [m ² /s]	Inlet flow rate [m ³ /s]	Velocity [mm/s]	Pressure [Pa]	Concentration [mol/m ³]
2	5	0.03	0.5	0.15
2	15	0.09	2	0.15
2	25	0.16	3.5	0.15
5	5	0.03	0.5	0.45
5	15	0.09	2	0.45
5	25	0.16	3.5	0.45
8	5	0.03	0.5	0.8
8	15	0.09	2	0.8
8	25	0.16	3.5	0.8

input parameters are the diffusion coefficient and inlet flow rate, while the output parameters are speed, pressure, and concentration. The output data obtained in the optimization processes were obtained by changing the input variables.

As a result of analysis and optimization processes, the liquids' diffusion coefficient should be higher than 5E-11 m²/s. The inlet flow rate value should be higher than 15E-15 m³/s to perform diffusion control of two different liquids types. Suppose the input variables are applied to the micromixing device in these value ranges. In that case, it is understood that the pressure in the outlet duct is in the range of 2-6 Pa, the velocity is in the range of 0.09-0.5 mm/s, and the concentration is in the range of 0-1 mol/m³. These values are the optimum values obtained for the analysis without damaging the microfluidic channels of the liquid supplied to the micromixer's inlet.

With this study, the diffusion control of two different liquids was successfully carried out in the microfluidic-based micromixing device. The analysis and optimization processes

showed that the separation between liquids depends on the diffusion coefficients of the species. The larger the difference in diffusion coefficients results in more efficient separation. This device can be used for diffusion control at the microlevel in many biomedical applications such as drug delivery, tumor cells, and blood analogs. In our next study, different sizes of micromixers will be designed, and their effect on the diffusion of liquids will be investigated.

Data Availability

Data deposited in a repository We prefer authors to deposit their data in a public repository that meets appropriate standards of archiving, citation, and curation.

Conflicts of Interest

The authors declare that they have no conflicts of interest.

References

- [1] E. Cesewski, A. P. Haring, Y. Tong et al., "Additive manufacturing of three-dimensional (3D) microfluidic-based microelectromechanical systems (MEMS) for acoustofluidic applications," *Lab on a Chip*, vol. 18, no. 14, pp. 2087–2098, 2018.
- [2] D. Sun and K. F. Böhringer, "Self-cleaning: from bio-inspired surface modification to MEMS/microfluidics system integration," *Micromachines*, vol. 10, no. 2, p. 101, 2019.
- [3] K. Özsoy, B. Duman, and G. D. İçkale, "Metal part production with additive manufacturing for aerospace and defense industry," *SDU International Journal of Technological Science*, vol. 11, no. 3, 2019.
- [4] X. Zhang, L. Li, and C. Luo, "Gel integration for microfluidic applications," *Lab on a Chip*, vol. 16, no. 10, pp. 1757–1776, 2016.
- [5] S. Akay, R. Heils, H. K. Trieu, I. Smirnova, and O. Yesil-Celiktas, "An injectable alginate-based hydrogel for microfluidic applications," *Carbohydrate Polymers*, vol. 161, pp. 228–234, 2017.
- [6] I. Uguz, C. M. Proctor, V. F. Curto et al., "A microfluidic ion pump for in vivo drug delivery," *Advanced Materials*, vol. 29, no. 27, p. 1701217, 2017.
- [7] M. S. Sotoudegan, O. Mohd, F. S. Ligler, and G. M. Walker, "Paper-based passive pumps to generate controllable whole blood flow through microfluidic devices," *Lab on a Chip*, vol. 19, no. 22, pp. 3787–3795, 2019.
- [8] S. Sivashankar, S. Agambayev, Y. Mashraei, E. Q. Li, S. T. Thoroddsen, and K. N. Salama, "A "twisted" microfluidic mixer suitable for a wide range of flow rate applications," *Bio-microfluidics*, vol. 10, no. 3, article 034120, 2016.
- [9] B. Mondal, S. Pati, and P. K. Patowari, "Influence of confluence angle between inlets on the mixing performance of micro-mixer with obstacles," in *Techno-Societal*, pp. 275–283, Springer, Cham, 2020.
- [10] L. Cortelezzi, S. Ferrari, and G. Dubini, "A scalable active micro-mixer for biomedical applications," *Microfluidics and Nanofluidics*, vol. 21, no. 3, p. 31, 2017.
- [11] A. A. S. Bhagat, E. T. Peterson, and I. Papautsky, "A passive planar micromixer with obstructions for mixing at low Reynolds numbers," *Journal of Micromechanics and Microengineering*, vol. 17, no. 5, pp. 1017–1024, 2007.
- [12] N. Sasaki, T. Kitamori, and H. B. Kim, "AC electroosmotic micromixer for chemical processing in a microchannel," *Lab on a Chip*, vol. 6, no. 4, pp. 550–554, 2006.
- [13] S. D. Svetlov and R. S. Abiev, "Formation mechanisms and lengths of the bubbles and liquid slugs in a coaxial- spherical micro mixer in Taylor flow regime," *Chemical Engineering Journal*, vol. 354, pp. 269–284, 2018.
- [14] M. A. Ansari, K. Y. Kim, and S. M. Kim, "Numerical and experimental study on mixing performances of simple and vortex micro T-mixers," *Micromachines*, vol. 9, no. 5, p. 204, 2018.
- [15] A. Haghghinia and S. Movahedirad, "Mass transfer in a novel passive micro-mixer: flow tortuosity effects," *Analytica Chimica Acta*, vol. 1098, pp. 75–85, 2020.
- [16] A. Shamloo, M. Mirzakanloo, and M. R. Dabirzadeh, "Numerical simulation for efficient mixing of Newtonian and non-Newtonian fluids in an electro-osmotic micro-mixer," *Chemical Engineering and Processing-Process Intensification*, vol. 107, pp. 11–20, 2016.
- [17] A. Usefian, M. Bayareh, A. Shateri, and N. Taheri, "Numerical study of electro-osmotic micro-mixing of Newtonian and non-Newtonian fluids," *Journal of the Brazilian Society of Mechanical Sciences and Engineering*, vol. 41, no. 5, p. 238, 2019.
- [18] E. Saygılı and Ö. Y. Celiktaş, "3d microfabrication and mixing phenomena in microfluidics," *Electronic Journal of Vocational Colleges*, vol. 8, no. 2, pp. 175–177, 2018.
- [19] M. R. Rasouli and M. Tabrizian, "An ultra-rapid acoustic micromixer for synthesis of organic nanoparticles," *Lab on a Chip*, vol. 19, no. 19, pp. 3316–3325, 2019.
- [20] T. Dehghani, F. S. Moghanlou, M. Vajdi, M. S. Asl, M. Shokouhimehr, and M. Mohammadi, "Mixing enhancement through a micromixer using topology optimization," *Chemical Engineering Research and Design*, vol. 161, pp. 187–196, 2020.
- [21] K. Du, W. Liu, Y. Ren et al., "A high-throughput electrokinetic micromixer via AC field-effect nonlinear electroosmosis control in 3D electrode configurations," *Micromachines*, vol. 9, no. 9, p. 432, 2018.
- [22] K. Nan, Z. Hu, W. Zhao, K. Wang, J. Bai, and G. Wang, "Large-scale flow in micro electrokinetic turbulent mixer," *Micromachines*, vol. 11, no. 9, p. 813, 2020.
- [23] H. Garg, "Linguistic Pythagorean fuzzy sets and its applications in multiattribute decision-making process," *International Journal of Intelligent Systems*, vol. 33, no. 6, pp. 1234–1263, 2018.
- [24] S. Guo and H. Zhao, "Fuzzy best-worst multi-criteria decision-making method and its applications," *Knowledge-Based Systems*, vol. 121, pp. 23–31, 2017.
- [25] M. Kuncan, K. Kaplan, A. C. A. R. Fatih, I. M. Kundakçi, and H. M. Ertunç, "Fuzzy logic based ball on plate balancing system real time control by image processing," *International Journal of Natural and Engineering Sciences*, vol. 10, no. 3, pp. 28–32, 2016.
- [26] S. Chung, L. E. Breshears, S. Perea et al., "Smartphone-based paper microfluidic particulometry of norovirus from environmental water samples at the single copy level," *ACS Omega*, vol. 4, no. 6, pp. 11180–11188, 2019.
- [27] M. Bayareh, M. N. Ashani, and A. Usefian, "Active and passive micromixers: a comprehensive review," *Chemical Engineering*

- and Processing-Process Intensification*, vol. 147, p. 107771, 2020.
- [28] G. Kunti, A. Bhattacharya, and S. Chakraborty, "Rapid mixing with high-throughput in a semi-active semi-passive micro-mixer," *Electrophoresis*, vol. 38, no. 9-10, pp. 1310–1317, 2017.
- [29] Y. Cheng, Y. Jiang, and W. Wang, "Numerical simulation for electro-osmotic mixing under three types of periodic potentials in a T-shaped micro-mixer," *Chemical Engineering and Processing-Process Intensification*, vol. 127, pp. 93–102, 2018.
- [30] P. Vatankhah and A. Shamloo, "Parametric study on mixing process in an in-plane spiral micromixer utilizing chaotic advection," *Analytica Chimica Acta*, vol. 1022, pp. 96–105, 2018.
- [31] W. Ruijin, L. Beiqi, S. Dongdong, and Z. Zefei, "Investigation on the splitting-merging passive micromixer based on Baker's transformation," *Sensors and Actuators B: Chemical*, vol. 249, pp. 395–404, 2017.
- [32] M. Nafea, N. Ahmad, A. R. Wahap, and M. S. M. Ali, "Modeling and simulation of a wireless passive thermopneumatic micromixer," in *Communications in Computer and Information Science*, pp. 312–322, Springer, Singapore, 2017.
- [33] A. Bordbar, A. Taassob, and R. Kamali, "Diffusion and convection mixing of non-Newtonian liquids in an optimized micro-mixer," *The Canadian Journal of Chemical Engineering*, vol. 96, no. 8, pp. 1829–1836, 2018.
- [34] S. Rashidi, H. Bafekr, M. S. Valipour, and J. A. Esfahani, "A review on the application, simulation, and experiment of the electrokinetic mixers," *Chemical Engineering and Processing-Process Intensification*, vol. 126, pp. 108–122, 2018.
- [35] H. Wang, Y. L. Zhang, W. Wang, H. Ding, and H. B. Sun, "On-chip laser processing for the development of multifunctional microfluidic chips," *Laser & Photonics Reviews*, vol. 11, no. 2, p. 1600116, 2017.
- [36] E. De Santis, A. Rizzi, and A. Sadeghian, "Hierarchical genetic optimization of a fuzzy logic system for energy flows management in microgrids," *Applied Soft Computing*, vol. 60, pp. 135–149, 2017.
- [37] K. Kaplan, M. Kuncan, and H. M. Ertunc, "Prediction of bearing fault size by using model of adaptive neuro-fuzzy inference system," in *2015 23rd signal processing and communications applications conference (SIU)*, pp. 1925–1928, Malatya, Turkey, May 2015.
- [38] W. Deng, J. Yang, C. Jiang, and D. Qiu, "Opacity of fuzzy discrete event systems," in *2019 Chinese control and decision conference (CCDC)*, pp. 1840–1845, Nanchang, China, June 2019.
- [39] M. J. Rivera, M. Santisteban, J. Aroba et al., "Application of fuzzy logic techniques for biogeochemical characterization of dams affected by acid mine drainage (AMD) processes in the Iberian Pyrite Belt (IPB), Spain," *Water, Air, & Soil Pollution*, vol. 231, no. 4, pp. 1–12, 2020.
- [40] Z. Li and L. Chen, "A novel evidential FMEA method by integrating fuzzy belief structure and grey relational projection method," *Engineering Applications of Artificial Intelligence*, vol. 77, pp. 136–147, 2019.
- [41] B. Pang, "Fuzzy counterparts of hull operators and interval operators in the framework of $_L$ -convex spaces," *Fuzzy Sets and Systems*, vol. 369, pp. 20–39, 2019.

Review Article

A Review Study on Mechanical Properties of Obtained Products by FDM Method and Metal/Polymer Composite Filament Production

Ümit Çevik¹ and Menderes Kam²

¹Düzce University, Institute of Science, Department of Manufacturing Engineering, Düzce, Turkey

²Düzce University, Cumayeri Vocational School, Department of Mechanical and Metal Technologies, Düzce, Turkey

Correspondence should be addressed to Menderes Kam; mendereskam@duzce.edu.tr

Received 24 June 2020; Accepted 20 October 2020; Published 21 November 2020

Academic Editor: Ehsan N. Zare

Copyright © 2020 Ümit Çevik and Menderes Kam. This is an open access article distributed under the Creative Commons Attribution License, which permits unrestricted use, distribution, and reproduction in any medium, provided the original work is properly cited.

In addition to traditional manufacturing methods, Additive Manufacturing (AM) has become a widespread production technique used in the industry. The Fused Deposition Modeling (FDM) method is one of the most known and widely used additive manufacturing techniques. Due to the fact that polymer-based materials used as depositing materials by the FDM method in printing of parts have insufficient mechanical properties, the technique generally has limited application areas such as model making and prototyping. With the development of polymer-based materials with improved mechanical properties, this technique can be preferred in wider application areas. In this context, analysis of the mechanical properties of the products has an important role in the production method with FDM. This study investigated the mechanical properties of the products obtained by metal/polymer composite filament production and FDM method in detail. It was reviewed current literature on the production of metal/polymer composite filaments with better mechanical properties than filaments compatible with three-dimensional (3D) printers. As a result, it was found that by adding reinforcements of composites in various proportions, products with high mechanical properties can be obtained. Thus, it was predicted that the composite products obtained in this way can be used in wider application areas.

1. Introduction

Additive Manufacturing (AM), also known as three-dimensional (3D) production and 3D printers, has been used in many applications in daily life, especially in recent years, with great technological progress. 3D printers, also known as one of the rapid prototyping methods, are used in research and academic studies as well as industry [1]. AM is a general definition that covers several methods used in the manufacturing of 3D objects. 3D production refers to a computer-aided mode of production using a data file derived from geometry data of objects with simple or complex geometry. The parts to be produced layer by layer based on different joining principles according to traditional methods used from the derived data file [2, 3].

AM is the process of depositing materials by layers on the layer to create parts from 3D model data instead of traditional

production methodologies and stereotyped manufacturing methods. Traditional manufacturing methods are based on the principle of extracting chip materials from the raw materials during the manufacture of the parts. The device used in manufacturing by following a tool path derived from the part geometry to be produced. Due to this peculiarity of additive manufacturing, it is possible to manufacture parts with complex geometries, as there is no chip removal during manufacturing, so material loss is minimal [3, 4]. AM has great potential to reduce both production time and cost of a product.

1.1. Literature Studies. We carried out literature studies systematically using scientific digital databases. We looked through national and international thesis and articles published between 1998 and 2020 and conducted scans in English and Turkish languages using the following words:

composite filament, metal/polymer composite filaments, FDM, polymer review, filament, and mechanical properties.

The literature studies on the metal/polymer composite filament manufacture and the mechanical properties of the products via the FDM method are given in Table 1.

In the literature studies, a commercial PLA filament has an average tensile strength of 60 MPa; it is expected that the tensile strength of any piece to be produced in the same cross-sections from the pure PLA filament is also close to that value. Various additives and additive ratios are subject to experimental studies in order to increase this value. For example, Matsuzaki et al. [9], in their work, while the material produced with the addition of 6.6% carbon to the PLA filament achieved 185.2 MPa tensile strength and increased the tensile strength of the material, achieved a tensile strength (57.1 MPa) close to the unadulterated PLA filament with the addition of jute at the same contribution rate (6.1%).

Significant increases in the tensile strength of the parts produced from composite filament, which is formed by adding additives such as carbon, carbon fiber, aramid, and glass fiber to a commercial filament without additives, decreased the strength of the material in the addition of materials with low strength such as cardboard powder. For example, Van Der Klift et al. [8], with the addition of 20.7% carbon to nylon filament, achieved 464.4 MPa tensile strength; Gregor-Svetek et al. [40] in HDPE reached the value of 1.89 MPa tensile strength with the addition of 75% cardboard powder to the filament. Similarly, Bettini et al. [12] achieved 203 MPa tensile strength with 8.6% aramid additive to PLA filament; Akhouni et al. [13] made PLA of 479 MPa tensile strength with the addition of 49% glass fiber to the filament. He et al. [41]. In their experimental study, reached a high tensile strength value of 939.7 MPa with the addition of carbon fiber to the PA6 filament by removing the gaps formed in the part with the controlled compression method during production.

In addition to the type of additive, additive ratios are very important in determining the mechanical properties of the material. Adding the same type of additive to the same filament in different proportions can also lead to significant changes in the mechanical properties of the material, and increasing the proportion of the additive does not always mean that it will increase the strength of the material (for example, Hwang et al. [20]). While ABS has a tensile strength of 42 MPa by adding 10% copper to the filament, tensile strength decreased to 26.5 MPa when they increased the copper additive to 30%.

The increase in the tensile strength of the material was observed until the contribution rate increased from 10% to 40% (Rajpurahit et al. [21]). As the rate of graphene used as additive material increases, a decrease in tensile strength of the material was observed.

2. Additive Manufacturing (AM) and 3D Printing Technologies

In this section, additive manufacturing methods, application areas of 3D printing technologies, history, advantages,

mechanical properties of production, and products with the FDM method are explained.

2.1. A Brief History of 3D Printing Technology. 3D printing technology was first developed by Charles Hull in 1984. Within 5-10 years, different printing technologies have been developed by making investments in 3D printing technology. SLS and FDM technologies were found in 1988. 3D printing technology started to be used in our daily life as the source of open source printers under the name of Reprap which entered the technology world in 2007 [5].

2.2. Advantages of 3D Printing Technology. The advantages of 3D printing technology include the following: minimum amount of waste material, low cost, enabling the production of complex geometry parts, no need for molds, enabling the production of parts with the desired composition, use in office-type working environments, measurement accuracy, chip removal, deburring, and no need for successive operations.

2.3. Application Areas of 3D Printing Technologies. Today, 3D printing technologies are used in sectors such as the automotive, aerospace, defense, and aviation industries, but their use in architectural structures, product and machine designs, prototype part production, education, textiles, toys and medical devices, and organ, prosthesis, and implant applications in the healthcare industry is becoming widespread.

2.4. Additive Manufacturing (AM) Methods. Many methods can be used in additive manufacturing and production, and the differences between methods are generally related to the method of creating layers. Selective Laser Sintering (SLS), Selective Laser Melting (SLM), Electron Beam Melting (EBM), Laser Metal Deposition (LMD), Fused Deposition Modeling (FDM), Stereolithography (SLA), and Digital Light Processing (DLP) technologies are among the most applied technologies for additive manufacturing [5, 43].

2.5. Production with FDM Method. Part production in 3D printers of the FDM type is similar to the traditional polymer extrusion process. The first stage of production is modeling the part in Computer-Aided Design (CAD) environment. The designed model is then converted into STL format to enable data transfer between the CAD environments. After 2D slicing of the model, data related to the model in STL format is transmitted to the 3D printer. 3D geometry of the piece designed in the computer environment is obtained with the superposition of thermoplastic molten material called filament, which is deposited from the nozzle of the 3D printer. Briefly, the FDM method is the process of pouring the molten material in a hot nozzle onto a heated flat table surface in layers (Figure 1).

The FDM production method is based on the principle of melting and bonding thermoplastic material where the polymer is used as the printing material. The method is becoming more and more widespread due to the advantages of the thermoplastic material used, such as cheap, long life, high toughness, easy to find, enabling recycling, some types can be dissolved quickly in nature, low shaping temperature, and

TABLE 1: Literature studies on composite filament production.

Study	Matrix materials	Additive materials	Fiber volume percentage (%)	Tensile strength (MPa)	Tensile modulus (GPa)	Compression strength (MPa)	Flexural strength (MPa)	Flexural modulus (GPa)	Breaking elongation (%)
Çantı [2]	ABS	ZrB ₂	1.5	40.2	2.14	—	—	—	5.88
		SiO ₂	1.5	44.72	2.49	—	—	—	4.84
		MWCNTs	1.5	41.2	1.68	—	—	—	4.05
		Al	1.5	44.56	2.55	—	—	—	6.99
Patan [5]	ABS	CF	12	31.70	2.72	70.51	43.80	—	1.64
Hodzic and Pandzic [6]	PLA	CF	20	29.96	4.54	—	—	—	—
	PET-G	CF	20	32.79	4.26	—	—	—	—
Mori et al. [7]	ABS	C	1.6	43	—	—	—	—	—
Van Der Klift et al. [8]	Nylon	C	6.9	140	14	—	—	—	—
		C	20.7	464.4	35.7	—	—	—	—
Matsuzaki et al. [9]	PLA	C	6.6	185.2	19.5	—	—	—	—
		Jut	6.1	57.1	5.11	—	—	—	—
Li et al. [10]	PLA	C	34	91	23.8	—	156	—	—
Yang et al. [11]	ABS	C	6.5	147	4.18	—	127	7.72	—
Bettini et al. [12]	PLA	Aramid	8.6	203	9.34	—	—	—	—
Akhoundi et al. [13]	PLA	Glass fiber	49	478	29.41	—	—	—	—
Saini [14]	—	ABS/PETG	50/50	32.5	—	—	—	—	—
Nagendra and Prasad [15]	Nylon	Aramid	2	51.45	—	—	98.16	—	—
Ning et al. [16]	ABS	CF	7.5	41.5	2.5	—	—	—	—
		CF	15	35	2.25	—	—	—	—
Tambrellimath et al. [17]	PC70%+ABS30%	GF	0.8	—	4.03	—	—	—	—
		Cu	—	58.3	1.01	—	118.7	3.84	—
		Wood	—	38.7	0.8	—	71	2.65	—
Liu et al. [18]	PLA	Ceramic	—	46.5	1.05	—	100.1	4.62	—
		Al	—	51.1	0.83	—	97.8	3.27	—
		CF	—	41.3	0.74	—	75.6	2.93	—
Tian et al. [19]	PLA	CF	27	—	—	—	335	30	—
		Cu	10	42	0.93	—	—	—	—
Hwang et al. [20]	ABS	Cu	30	26.5	0.91	—	—	—	—
		Fe	10	43.4	0.96	—	—	—	—
		Fe	40	36.2	0.95	—	—	—	—
		GF	0	44.75	0.71	—	75.50	2.52	—
Rajpurohit and Dave [21]	PLA	GF	1	43.65	0.81	—	56.65	2.25	—
		GF	3	31.60	0.60	—	61.80	2.34	—
		GF	5	24.65	0.57	—	50.55	2.11	—
Zhong et al. [22]	ABS	Glass fiber	18	58.6	—	—	—	—	—
		CF	10	52	7.7	—	—	—	—
Tekinalp et al. [23]	ABS	CF	20	60	11.5	—	—	—	—
		CF	30	62	13.8	—	—	—	—
		CF	40	67	13.7	—	—	—	—
Love et al. [24]	ABS	CF	13	70.69	8.91	—	—	—	—
Hill et al. [25]	ABS	CF	20	66.8	8.4	—	—	—	—
		CF	20	65.7	11.9	—	—	—	—
Duty et al. [26]	ABS	GF	20	54.3	5.7	—	—	—	—
		GF	40	51.2	10.8	—	—	—	—

TABLE 1: Continued.

Study	Matrix materials	Additive materials	Fiber volume percentage (%)	Tensile strength (MPa)	Tensile modulus (GPa)	Compression strength (MPa)	Flexural strength (MPa)	Flexural modulus (GPa)	Breaking elongation (%)
Kunc [27]	ABS	CF	13	53	8.15	—	—	—	—
Gardner et al. [28]	PEI	CNT	4.7	125.3	3	—	—	—	—
DeNardo [29]	PPS	CF	50	92.2	26.4	—	—	—	—
Perez et al. [30]	ABS	Jute fiber	5	25.9	1.54	—	—	—	—
Mahajan and Cormier [31]	Epoxy	CF	15	66.3	4.05	—	—	—	—
Ferreira et al. [32]	PLA	CF	15	53.4	7.54	—	—	—	—
Compton and Lewis [33]	Epoxy	SiC CF	10	66.2	24.5	—	—	—	—
Dickson et al. [34]	Nylon	CF	11	198	8.46	—	—	—	—
		AF	8	110	4.23	—	—	—	—
		GF	8	156	3.29	—	—	—	—
		GF	10	212	4.91	—	—	—	—
Shofner et al. [35]	ABS	VGCF	10	37.4	0.8	—	—	—	—
Melenka et al. [36]	Nylon	Kevlar	4.04	31	1.77	—	—	—	—
		Kevlar	8.08	60	6.92	—	—	—	—
		Kevlar	10.1	84	9	—	—	—	—
Gao et al. [37]	PLA	Talc	2	57.9	1.47	—	—	—	7.3
		CF	5	31.7	1.10	—	—	—	13
		Cu	25	17.12	0.7	—	—	—	8.46
Nabipour et al. [38]	PE	Cu	50	18.25	0.79	—	—	—	7.45
		Cu	75	19.41	1.2	—	—	—	5.95
Wang et al. [39]	SCF/PA	C-CFRP	25	288.65	28.97	—	—	—	—
	PLA	C-CFRP	25	277.11	29.12	—	—	—	—
	PA	C-CFRP	25	252.36	26.68	—	—	—	—
	PC	C-CFRP	25	238.85	26.28	—	—	—	—
Gregor-Svetek et al. [40]	HDPE	PET-G	25	256.04	28.21	—	—	—	—
		Cardboard	20	9.04	0.32	—	—	—	36.2
		Cardboard	50	2.05	0.12	—	—	—	7.6
He et al. [41]	PA6	CF	—	939.7	83.2	—	1051.8	57.3	—
Karaman and Çolak [42]	ABS	CF	10	32.78	1.67	—	—	—	—

reshaping when heated. Today, home users can also produce various parts with this method. Due to the simple working principle and low equipment required, the costs of devices producing with the FDM method are lower than the devices used in other AM methods.

Due to these features, the FDM method produced devices called 3D printers suitable for desktop use (Figure 2). Due to the low cost and other advantages of both devices and thermoplastic materials, the FDM method has also been used by individual users. Thermoplastics used in production with FDM are materials of polymer class; they can be softened and shaped when they are heated while being present in a solid

state at low temperatures. After the thermoplastic-forming process is finished, it cools and solidifies, and in this way, the product with the desired geometry is obtained.

2.6. Filaments Used in 3D Printers. Thermoplastic-based filaments used in 3D printers are produced by plastic extrusion machines called filament extruders. Extrusion systems work with the logic of mixing raw plastic granules and other additives, if any, in a mechanical mixer and then transporting the composite granules formed through a feed hopper to the heater nozzle side with the help of a screw shaft (Figure 3).

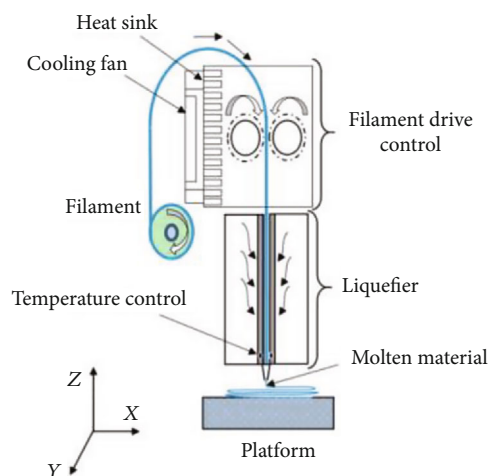


FIGURE 1: Production by FDM method [6].

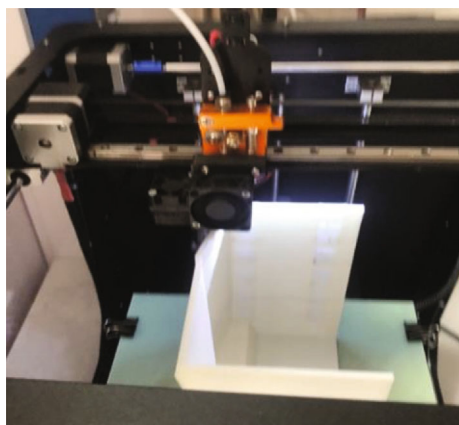


FIGURE 2: 3D printer.

The raw material, which is melted in the filament extruder and gained fluidity, is removed in the desired diameter (usually 1.75 mm or 3 mm) and turned into a film strip in various colors and properties, called filament, ready for use in a 3D printer (Figure 4).

Polymers with filament raw materials are preferred as matrix materials in the production of composite materials due to their low shaping costs and ability to work with many traditional production methods, enabling the production of complex-shaped parts due to their low density, and ease of metal removal processes. In addition to these advantages, polymer materials have low mechanical properties and thermal resistance. Therefore, metal/polymer composites with high mechanical and thermal properties are needed in the industry. Polymers used as a polymer matrix in composite materials are thermosets and thermoplastics. Metal/polymer composite filaments are produced by making particle reinforcement to improve many properties such as thermal resistance, strength, and impact resistance to polymer materials (Figure 5). Thus, with the development of polymer-based materials with improved mechanical properties, the production with the FDM method can find a wider application in the industry.

In addition to the polymer filament type used as the matrix phase on the mechanical properties of the parts produced by the FDM method, adding the additives to improve the mechanical properties with the production parameters are also effective. Although the types of filaments frequently used in production are Acrylonitrile Butadiene Styrene (ABS), Polylactic Acid (PLA), and Polyethylene Terephthalate-Glycol (PET-G) [45, 46], metal/polymer composite materials produced by adding metal or thermoplastic materials in various proportions have also been used in recent years. This study also compiled important literature studies to improve the mechanical properties of existing filaments using additional additives. The aim of the research is to bring together the most important studies in this field and to reveal what are the additives that provide improvement in the mechanical properties of the composite filaments produced. In addition, it is intended to be a practical guide in experimental studies and planning for those who will start new research in this field or those who designs a new composite filament.

2.7. Mechanical Properties of Products. In order for the materials to be used successfully, it is necessary to know the mechanical properties, and if necessary, these properties should be improved according to the usage area. When the mechanical properties of the material are mentioned, tensile strength, impact strength, elastic modulus, yield strength, fatigue strength, hardness, etc., features come to mind. If we evaluate the determination of the mechanical properties of the products printed by the FDM method under two main headings, we can conclude that the first of these is the printing parameters and the other is additives and additive ratios.

Many studies have been conducted in the literature to examine the effect of 3D printing parameters on the mechanical properties of 3D printed products [47–55]. Kam et al. [47] in their study produced six different filling test samples by keeping parameters such as the filling ratio, printing speed, layer thickness, filament, and nozzle diameter constant. As a result of the experimental study, it was concluded that the strength of the parts produced with the rectilinear filling pattern is approximately 15% higher than the parts produced with the other filling pattern. It is also stated in the same study that the full honeycomb filling method shows more extension than other filling forms. In this study, studies to investigate the effect of additive, which is another important issue in determining the mechanical properties of the parts produced by the FDM method, on the mechanical properties of the parts produced by the FDM method, were compiled.

3. Conclusion

In this review study, works on the changes in the mechanical properties of metal/polymer composite filaments or products printed by FDM method adding various additives to commercial filaments were compiled. According to the results obtained from experimental studies, the following inferences are made:

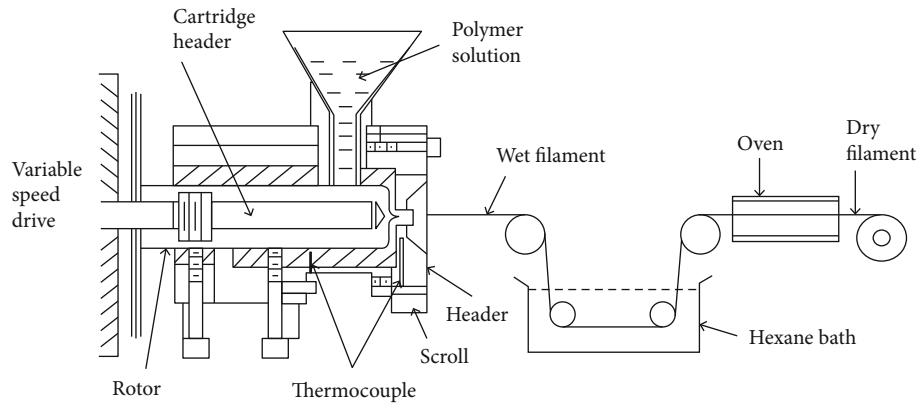


FIGURE 3: Schematic representation of filament extruder [44].



FIGURE 4: Filaments used in 3D printers.



FIGURE 5: Composite copper filament.

(i) Plastic and metal additives in different ratios are used in metal/polymer composite filament manufacturing. The optimum contribution rates were tried to be determined in the experimental studies conducted in the literature.

- (ii) In determining the mechanical properties of the parts produced using composite filament, besides the characteristic properties of the commercial filament, the type of additive and additive ratios have important changes to the mechanical properties of the products. Considering that a commercial PLA filament has an average tensile strength of 60 MPa, it is expected that the tensile strength of any piece to be produced in the same cross-sections from the pure PLA filament is also close to that value. Various additives and additive ratios are subject to experimental studies in order to increase this value.
- (iii) Significant increases in the tensile strength of the parts produced from the composite filament, which are formed by adding additives such as carbon, carbon fiber, aramid, and glass fiber to a commercial filament without additives, decreased the strength of the material in the addition of materials with low strength such as cardboard powder.
- (iv) In addition to the type of additive, additive ratios are very important in determining the mechanical properties of the material. Adding the same type of

additive to the same filament in different proportions can also lead to significant changes in the mechanical properties of the material, and increasing the proportion of the additive does not always mean that it will increase the strength of the material.

- (v) As can be understood from the experimental data, besides the optimal test parameters, the filament used as a matrix material and the type of additives and the additive ratios are extremely effective on the mechanical properties of the produced parts.
- (vi) Finally, as production with the FDM method is an increasingly widespread and promising technology, the studies in this area have been increasing rapidly in recent years.
- (vii) The FDM method and composite material technology have a wide range of applications and composite filaments that have widespread use and are close to the desired mechanical properties which can be produced with different filaments and different additives and additive ratios in academic studies.

Conflicts of Interest

All the authors declare no conflict of interest.

References

- [1] M. Günay, S. Gündüz, H. Yılmaz, N. Yaşar, and R. Kaçar, “PLA esaslı numunelerde çekme dayanımı için 3D baskı işlem parametrelerinin optimizasyonu,” *Journal of Polytechnic*, vol. 23, no. 1, pp. 73–79, 2020.
- [2] E. Çantı, “Production and characterization of polymer nanocomposite filaments for 3D printers,” *Master Thesis. [Production and characterization of polymer nanocomposite filaments for 3d printers] [thesis in Turkish]*, Dumlupınar University, Kütahya, 2016.
- [3] D. Ding, Z. Pan, D. Cuiuri, H. Li, N. Larkin, and S. van Duin, “Automatic multi-direction slicing algorithms for wire based additive manufacturing,” *Robotics and Computer-Integrated Manufacturing*, vol. 37, pp. 139–150, 2016.
- [4] C. Klahn, B. Leutenecker, and M. Meboldt, “Design strategies for the process of additive manufacturing,” *Procedia CIRP*, vol. 36, pp. 230–235, 2015.
- [5] Z. Patan, “Karbon fiber takviyeli ABS kompozitlerin FDM 3B yazıcı ile üretimi ve “ansys ile modellenmesi”,” *Yüksek Lisans Tezi. [Production of carbon fiber reinforced ABS composites with FDM 3D printer and modelling with ANSYS] [thesis in Turkish]*, Onsekizmart Üniversitesi, Çanakkale, 2019.
- [6] D. Hodzic and A. Pandzic, “Influence of carbon fibers on mechanical properties of materials in FDM technology,” in *Proceedings of the 30th DAAAM International Symposium*, pp. 1726–1729, Vienna, 2019.
- [7] K. I. Mori, T. Maeno, and Y. Nakagawa, “Dieless forming of carbon fibre reinforced plastic parts using 3D printer,” *Procedia engineering*, vol. 81, pp. 1595–1600, 2014.
- [8] F. Van Der Klift, Y. Koga, A. Todoroki, M. Ueda, Y. Hirano, and R. Matsuzaki, “3D printing of continuous carbon fibre reinforced thermo-plastic (CFRTP) tensile test specimens,” *Open Journal of Composite Materials*, vol. 6, no. 1, pp. 18–27, 2016.
- [9] R. Matsuzaki, M. Ueda, M. Namiki et al., “Three-dimensional printing of continuous-fiber composites by in-nozzle impregnation,” *Scientific reports*, vol. 6, no. 1, 2016.
- [10] N. Li, Y. Li, and S. Liu, “Rapid prototyping of continuous carbon fiber reinforced polylactic acid composites by 3D printing,” *Journal of Materials Processing Technology*, vol. 238, pp. 218–225, 2016.
- [11] C. Yang, X. Tian, T. Liu, Y. Cao, and D. Li, “3D printing for continuous fiber reinforced thermoplastic composites: mechanism and performance,” *Rapid Prototyping Journal*, vol. 23, no. 1, pp. 209–215, 2017.
- [12] P. Bettini, G. Alitta, G. Sala, and L. di Landro, “Fused deposition technique for continuous fiber reinforced thermoplastic,” *Journal of Materials Engineering and Performance*, vol. 26, no. 2, pp. 843–848, 2017.
- [13] B. Akhouni, A. H. Behraves, and A. Bagheri Saed, “An innovative design approach in three-dimensional printing of continuous fiber-reinforced thermoplastic composites via fused deposition modeling process: in-melt simultaneous impregnation,” *Proceedings of the Institution of Mechanical Engineers, Part B: Journal of Engineering Manufacture*, vol. 234, no. 1-2, pp. 243–259, 2020.
- [14] M. Saini, “Optimization the process parameter of FDM 3D printer using Taguchi method for improving the tensile strength,” *International Journal of All Research Education and Scientific Methods*, vol. 7, no. 4, 2019.
- [15] J. Nagendra and M. G. Prasad, “FDM process parameter optimization by Taguchi technique for augmenting the mechanical properties of nylon-aramid composite used as filament material,” *Journal of The Institution of Engineers (India): Series C*, vol. 10, no. 2, pp. 313–322, 2020.
- [16] F. Ning, W. Cong, J. Qiu, J. Wei, and S. Wang, “Additive manufacturing of carbon fiber reinforced thermoplastic composites using fused deposition modeling,” *Composites Part B: Engineering*, vol. 80, pp. 369–378, 2015.
- [17] V. Tambrallimath, R. Keshavamurthy, S. D. P. G. Koppad, and G. S. P. Kumar, “Thermal behavior of PC-ABS based graphene filled polymer nanocomposite synthesized by FDM process,” *Composites Communications*, vol. 15, pp. 129–134, 2019.
- [18] Z. Liu, Q. Lei, and S. Xing, “Mechanical characteristics of wood, ceramic, metal and carbon fiber-based PLA composites fabricated by FDM,” *Journal of Materials Research and Technology*, vol. 8, no. 5, pp. 3741–3751, 2019.
- [19] X. Tian, T. Liu, C. Yang, Q. Wang, and D. Li, “Interface and performance of 3D printed continuous carbon fiber reinforced PLA composites,” *Composites Part A: Applied Science and Manufacturing*, vol. 88, pp. 198–205, 2016.
- [20] S. Hwang, E. I. Reyes, K. S. Moon, R. C. Rumpf, and N. S. Kim, “Thermo-mechanical characterization of Metal/Polymer composite filaments and printing parameter study for fused deposition modeling in the 3D printing process,” *Journal of Electronic Materials*, vol. 44, no. 3, pp. 771–777, 2015.
- [21] S. R. Rajpurohit and H. K. Dave, “Fused deposition modeling using graphene/pla nano-composite filament,” *International Journal of Modern Manufacturing Technologies*, vol. 6, no. 2, pp. 2067–2074, 2019.
- [22] W. Zhong, F. Li, Z. Zhang, L. Song, and Z. Li, “Short fiber reinforced composites for fused deposition modeling,” *Materials Science and Engineering: A*, vol. 301, no. 2, pp. 125–130, 2001.

- [23] H. L. Tekinalp, V. Kunc, G. M. Velez-Garcia et al., "Highly oriented carbon fiber-polymer composites via additive manufacturing," *Composites Science and Technology*, vol. 105, pp. 144-150, 2014.
- [24] L. J. Love, V. Kunc, O. Rios et al., "The importance of carbon fiber to polymer additive manufacturing," *Journal of Materials Research*, vol. 2, no. 17, pp. 1893-1898, 2014.
- [25] C. Hill, K. Rowe, R. Bedsole, J. Earle, and V. Kunc, "Materials and process development for direct digital manufacturing of vehicles," in *SAMPE Long Beach 2016 Conference and Exhibition*, 2016.
- [26] C. E. Duty, T. Drye, and A. Franc, "Material development for tooling applications using big area additive manufacturing," in *(BAAM) (No. ORNL/TM-2015/78). Oak Ridge National Lab.(ORNL), Oak Ridge, TN (United States)*, Manufacturing Demonstration Facility (MDF), 2015.
- [27] V. Kunc, "Advances and challenges in large scale polymer additive manufacturing," in *Proceedings of the 15th SPE Automotive Composites Conference*, vol. 9, Novi, MI, USA, 2015.
- [28] J. M. Gardner, G. Sauti, J. W. Kim et al., *Additive manufacturing of multifunctional components using high density carbon nanotube yarn filaments*, Hampton, 2016.
- [29] N. M. DeNardo, "Additive manufacturing of carbon fiber-reinforced thermoplastic composites," *A Thesis*, Purdue University, Indiana, 2016.
- [30] A. R. Torrado Perez, D. A. Roberson, and R. B. Wicker, "Fracture surface analysis of 3D-printed tensile specimens of novel ABS-based materials," *Journal of Failure Analysis and Prevention*, vol. 14, no. 3, pp. 343-353, 2014.
- [31] C. Mahajan and D. Cormier, "3D printing of carbon fiber composites with preferentially aligned fibers," in *IIE annual conference. Proceedings*, Institute of Industrial and Systems Engineers (IISE), p. 2953, 2015.
- [32] R. T. L. Ferreira, I. C. Amatte, T. A. Dutra, and D. Bürger, "Experimental characterization and micrography of 3D printed PLA and PLA reinforced with short carbon fibers," *Composites Part B: Engineering*, vol. 124, pp. 88-100, 2017.
- [33] B. G. Compton and J. A. Lewis, "3D-printing of lightweight cellular composites," *Advanced Materials*, vol. 26, no. 34, pp. 5930-5935, 2014.
- [34] A. N. Dickson, J. N. Barry, K. A. McDonnell, and D. P. Dowling, "Fabrication of continuous carbon, glass and Kevlar fibre reinforced polymer composites using additive manufacturing," *Additive Manufacturing*, vol. 16, pp. 146-152, 2017.
- [35] M. L. Shofner, K. Lozano, F. J. Rodríguez-Macías, and E. V. Barrera, "Nanofiber-reinforced polymers prepared by fused deposition modeling," *Journal of Applied Polymer Science*, vol. 89, no. 11, pp. 3081-3090, 2003.
- [36] G. W. Melenka, B. K. O. Cheung, J. S. Schofield, M. R. Dawson, and J. P. Carey, "Evaluation and prediction of the tensile properties of continuous fiber-reinforced 3D printed structures," *Composite Structures*, vol. 153, pp. 866-875, 2016.
- [37] X. Gao, D. Zhang, S. Qi, X. Wen, and Y. Su, "Mechanical properties of 3D parts fabricated by fused deposition modeling: effect of various fillers in polylactide," *Journal of Applied Polymer Science*, vol. 136, no. 31, p. 47824, 2019.
- [38] M. Nabipour, B. Akhoundi, and A. Bagheri Saed, "Manufacturing of polymer/metal composites by fused deposition modeling process with polyethylene," *Journal of Applied Polymer Science*, vol. 137, no. 21, 2020.
- [39] F. Wang, Z. Zhang, F. Ning, G. Wang, and C. Dong, "A mechanistic model for tensile property of continuous carbon fiber reinforced plastic composites built by fused filament fabrication," *Additive Manufacturing*, vol. 32, 2020.
- [40] D. Gregor-Sveteč, M. Leskovšek, U. Vrabič Brodnjak, U. Stankovič Elesini, D. Muck, and R. Urbas, "Characteristics of HDPE/cardboard dust 3D printable composite filaments," *Journal of Materials Processing Technology*, vol. 276, p. 116379, 2020.
- [41] Q. He, H. Wang, K. Fu, and L. Ye, "3D printed continuous CF/PA6 composites: effect of microscopic voids on mechanical performance," *Composites Science and Technology*, vol. 191, p. 108077, 2020.
- [42] E. Karaman and O. Çolak, "The effects of process parameters on mechanical properties and microstructures of parts in fused deposition modeling," *Duzce University Journal of Science & Technology*, vol. 8, no. 1, pp. 617-630, 2020.
- [43] J.-P. Kruth, M. C. Leu, and T. Nakagawa, "Progress in additive manufacturing and rapid prototyping," *Keynote Papers*, vol. 47, no. 2, pp. 525-540, 1998.
- [44] H. Mahfuz, M. R. Khan, T. Leventouri, and E. Liarokapis, "Investigation of MWCNT reinforcement on the strain hardening behavior of ultrahigh molecular weight polyethylene," *Journal of Nanotechnology*, p. 9, 2011.
- [45] A. İpekçi, M. Kam, and H. Saruhan, "Investigation of 3D printing occupancy rates effect on mechanical properties and surface roughness of PET - G material products," *Journal of New Results in Science*, vol. 7, no. 2, pp. 1-8, 2018.
- [46] M. Kam, A. İpekçi, and H. Saruhan, "Investigation of 3D printing filling structures effect on mechanical properties and surface roughness of PET-G material products," *Gaziosmanpasa Journal of Scientific Research*, vol. 6, pp. 114-121, 2017.
- [47] M. Kam, H. Saruhan, and A. İpekçi, "The effect of filling structures on strength of printed products by 3D printers," *Duzce University Journal of Science & Technology*, vol. 7, no. 3, pp. 951-960, 2019.
- [48] M. Kam, H. Saruhan, and A. İpekçi, "Investigation the effects of 3D printer system vibrations on mechanical properties of the printed products," *Sigma Journal of Engineering and Natural Sciences*, vol. 36, no. 3, pp. 655-666, 2018.
- [49] M. Kam, H. Saruhan, and A. İpekçi, *Investigation of surface treatment effect on mechanical properties of printed products by fused deposition modelling method*, IV. International Academic Research Congress, Antalya, 2018, Volume: ISBN: 978-605-196-226-9.
- [50] M. Kam, H. Saruhan, and A. İpekçi, *Surface treatments effect on surface roughness of printed products by fused deposition modelling method*, IV. International Academic Research Congress, 2018.
- [51] M. Kam, H. Saruhan, and A. İpekçi, *Determination of optimum printing parameters of printed products by open and closed type of 3d printer systems with different filament materials*, IV. International Academic Research Congress, Antalya, 2018.
- [52] M. Kam and A. İpekçi, *Experimental and simulation comparison of the effect of filling structures on strenght in fdm products*, IV. International Academic Research Congress, Antalya, 2018.
- [53] M. Kam, A. İpekçi, and Ö. Şengül, "Effect of FDM process parameters on the mechanical properties and production costs of 3D printed PowerABS samples," *International Journal of Analytical, Experimental and Finite Element Analysis*, RAME Publishers, vol. 7, no. 3, pp. 77-90, 2020.

- [54] M. Kam, H. Saruhan, and A. İpekci, "Investigation the effect of 3D printer system vibrations on surface roughness of the printed products," *Duzce University Journal of Science & Technology*, 2019.
- [55] M. Kam, H. Saruhan, and A. İpekci, "Experimental analysis of vibration damping capabilities of sleeve bearings printed using FDM method," *Journal of Polytechnic*, 2021.

Research Article

A Novel Label-Free Biosensor for Detection of HE4 in Urine Based on Localized Surface Plasmon Resonance and Protein G Directional Fixed

Ruiqi Duan^{1,2} and Mingrong Xi^{1,2} 

¹Department of Obstetrics and Gynecology, West China Second University Hospital, Sichuan University, Chengdu, China

²Key Laboratory of Birth Defects and Related Diseases of Women and Children (Sichuan University), Ministry of Education, Chengdu, China

Correspondence should be addressed to Mingrong Xi; mingrongxi2008@163.com

Received 8 June 2020; Revised 17 September 2020; Accepted 8 October 2020; Published 23 October 2020

Academic Editor: Pooyan makvandi

Copyright © 2020 Ruiqi Duan and Mingrong Xi. This is an open access article distributed under the Creative Commons Attribution License, which permits unrestricted use, distribution, and reproduction in any medium, provided the original work is properly cited.

A non-invasive and more sensitive method for detection of HE4 is very important for the early screening and detection of ovarian carcinoma. In this study, we improved our previous localized surface plasmon resonance (LSPR) biosensor for detection of HE4 in urine to overcome disadvantages of conventional methods. Protein G directional fixed method was firstly used for LSPR biosensor to improved sensitivity, and standard HE4 and clinical samples were detected separately using this new biosensor. Compared to our previous LSPR biosensor, this new sensor was more sensitive, with other advantages as before. Under optimum conditions, this new biosensor could display a detection limit of 1 pM and wide dynamic range of 1 pM to 10,000 pM. This new biosensor was effective for detection of HE4 in urine of early ovarian cancer patients, without label and purification. To the best of our knowledge, this is first work to investigate LSPR biosensor for detection of tumor marker in urine, with great advantages and clinical application potentials.

1. Introduction

Ovarian cancer is one of the most common malignant diseases and represents the primary mortality for gynecological cancers, despite adopting more sophisticated diagnostic methods and novel methods of treatment [1–4]. This is caused by the fact that most cases are not discovered until an advanced stage [2–4]. Therefore, it is crucial to find a non-invasive, sensitive and specific assay for early screening and detection of ovarian carcinoma. The human epididymis secretory protein 4 (HE4), has been widely studied and considered as a promising tumor marker for early diagnosis of ovarian cancer [4–10]. Reportedly, HE4 is highly sensitive to early ovarian cancer and can be used as a better method for diagnosis in ovarian cancer [4–6, 9].

Current methods available for detection of HE4 such as enzyme-linked immunosorbent assay (ELISA) and chemiluminescent immunoassay (CLIA), still have obvious

shortcomings [10–12]. To overcome disadvantages of conventional tools, our previous study developed a localized surface plasmon resonance (LSPR) biosensor for detection HE4 in patients' blood serum, with advantages as convenient, low-cost, and label-free, and sensitivity [10]. But, for extensive general women, serological detection is invasive and difficult to accept. Therefore, it is important to develop an alternative method for clinical screening and early diagnosis of ovarian cancer. Recently, some study indicated that HE4 protein can be detected in urine since it has a molecular weight around 25kD [9]. Compared to serological detection, measuring HE4 in urine can provide a non-invasive and more convenient approach to aid early detection of ovarian cancer.

Previously, we have once achieved the detection of albumin in urine samples from mild preeclampsia patients by this LSPR biosensor [13]. However, HE4, as a tumor marker, is smaller than albumin, with concentration in urine

inferior to serum and unstable. Therefore, it is very challenging for measuring HE4 of urine in clinical patients. Up to date, LSPR biosensors have not been studied for detection of HE4 and other tumor marker in urine. To explore clinical application of LSPR biosensor, we firstly attempted to improve the sensitivity of this biosensor by introducing protein G directional fixed method, and successfully used this new build biosensor to detect HE4 in urine of early ovarian cancer patients. Compared to our previous LSPR biosensor [10, 12, 13], this new sensor was more sensitive. To the best of our knowledge, this was the first work to investigate the LSPR biosensor for the detection of tumor marker in urine. This novel LSPR biosensor provided a more sensitive and label-free method for detection HE4 in patients' urine using simple and convenient instrumentation, with great potential for applications in clinical screening of ovarian cancer and other tumors.

2. Materials and Methods

2.1. Materials. 11-Mercaptoundecanoic acid (MUA), 1-Ethyl-3-(3-dimethylaminopropyl) carbodiimide hydrochloride (EDC) and N-hydroxysuccinimide (NHS) were acquired from Sigma-Aldrich (Missouri, the United States of America). Protein G was obtained from BioVision (California, the United States of America). Mouse monoclonal anti-HE4 antibody and standard HE4 were purchased from Abnova (Taiwan, China). Quartz glass substrates from Juke (Chengdu, China) and Ag wire from Jubo (Beijing, China). Ultrapure water (18.3 MV/cm) used for the preparation of all solutions was from Millipore (Massachusetts, the United States of America). All reagents used were of analytical reagent grade.

2.2. Build of LSPR Biosensor. The integrated LSPR biosensor was built on-site, as our previous study reported in detail [10, 12]. Briefly, the sensor chip of silver nanoparticles was fabricated as triangular-shaped array by using nanosphere lithography (NSL) technology was used. The peak wavelength of LSPR absorption spectrum (λ_{max}) excited by the silver nanoparticles was detected and recorded by a Ultraviolet Rays-visible spectrometer (Model 9055; Sciencetech, Ottawa, Canada). The incident light was provided by white light emerging from the optical fiber bundle. Coupled with the optical detection probe, the noble LSPR absorption spectra could be excited and directly obtained by the spectroscopy at room temperature, ranging from 400 nm to 800 nm, and timely displayed on the computer screen.

All the absorption spectra were recorded and analyzed through Spectra Suite software (Ocean Optics, Florida, the United States of America). The relative LSPR wavelength shift ($\Delta\lambda_{max}$) was used to monitor the binding of target analytes. A shift towards the longer LSPR wavelength region was referred to as a red-shift and denoted as (+); whereas, a shift towards the shorter LSPR wavelength region was defined as a blue-shift and indicated as (-). The resolution of our system archived 3 nm and indicated that our biosensor could analyze the analyte on the nanoparticles-solution interface when $\Delta\lambda_{max}$ was over +3 nm.

2.3. Further Functionalization of the LSPR Biosensor. A multistep process was made to prepare the sensor chip for biodection events (Figure 1). During every experimental process, peak wavelength of LSPR absorption spectrums were excited, observed and used to improve the experimental conditions. The experimental conditions of each step were obtained after repeated explorations and attempts. Finally, optimal conditions were achieved as followed. First, the silver nanochip was incubated in 1 mM 11-MUA solution (in ethanol) for 10 hours at room temperature to form a self-assembled monolayer on the slice surface more effectively, then washed thoroughly with pure ethanol to remove nonspecific binding and dried at room temperature. Next, the nanochip was incubated in 75 mM EDC-HCl/15 mM NHS (volume/volume=1) solution for another hour at room temperature to preferably activate the carboxyl group of 11-MUA, which would effectively react with amino groups of protein G to form amides. Subsequently, the sensor chip was incubated with 100ug/ml protein G solution (in PBS, pH 5.5) for thirty minutes at room temperature to betterly couple the amine groups of protein G to the carboxyl groups on MUA. Next, in order to immobilization the antibody onto the chip by coupling with protein G, 50 μ L of anti-HE4 solution (10 μ g/mL) was spotted onto nanochip surface and overnight incubation at 4°C followed. After above steps, functional nanochip was immersed in ethanalamine solution (pH 8.5) for 30 minutes to deactivate coupled esters, then the surface was washed by phosphate-buffered solution (PBS) (pH 7.4) to remove nonspecific binding. At last, a new functionalization of HE4 LSPR biosensor was finished, as demonstrated in Figure 1. Meanwhile, the silver nanoparticles characterization using SEM (scanning electron microscope) were, respectively, observed before and after modification, as shown in Figure 2.

2.4. Clinical Samples. All detection samples in this study were from leftover urine samples in routine clinical urine tests collected from West China Second University Hospital (Chengdu, China), with no use and no harm to patients and institution. Urines of healthy women, benign ovarian cyst patients and early (I/II) ovarian cancer patients were, respectively, obtained. The disease diagnosis and staging involved were acquired from surgical and pathological results of gynecological oncologist and gynecological pathology experts. No personal privacy and no ethical harm to patients were involved in this study, owing to other medical records such as name, age, and registration number, etc were not needed. So, Research Ethics Approval from Ethics Institutional Board and written informed consents from patients were not needed in this study.

2.5. Detection of HE4 in Urine. In detection stage, at first, the different concentrations of commercial HE4 were, respectively, incubated on new functionalized LSPR chips at room temperature for 30 minutes. The biosensor chips were then dried after thorough rinsing with PBS (0.05% Tween-20) and subsequently by ultrapure water to dissociate the nonspecific binding. At last, the change in LSPR wavelength caused by antibody-antigen combination was observed and recorded. As above method, all urine samples were detected,

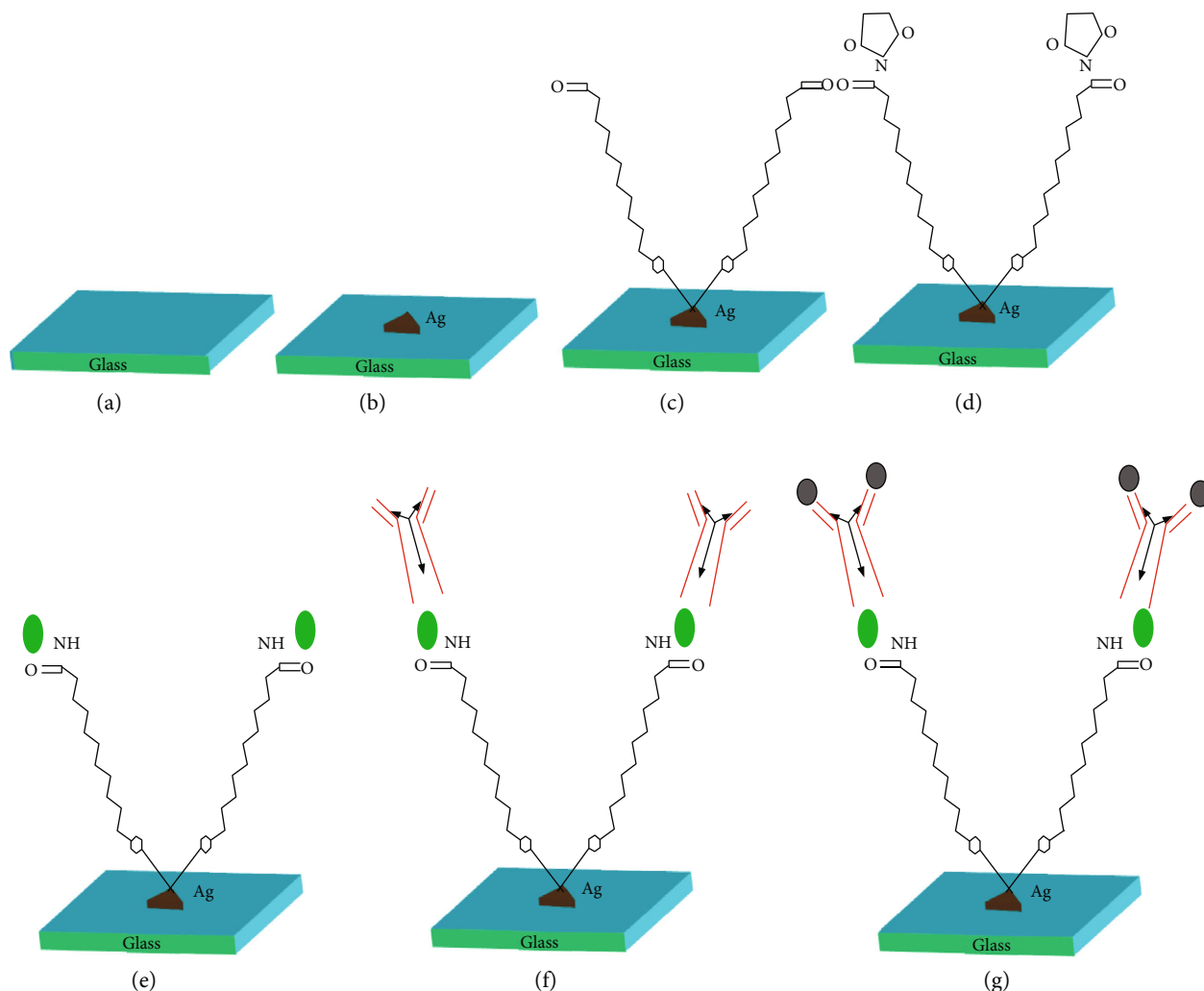


FIGURE 1: Design of the novel LSPR biosensor for detection of HE4. (a). Glass substrate. (b). Triangle-shaped silver nanoparticles array synthesized on glass substrate. (c). Incubation of 1 mM MUA. (d). Incubated in 75 mM EDC-HCl/15 mM NHS. (e). Incubated with 100ug/ml protein G. (f). Immobilization of anti-HE4 monoclonal antibodies (10 μ g/mL). (g). Immunoassay of HE4 in buffer or urine samples.

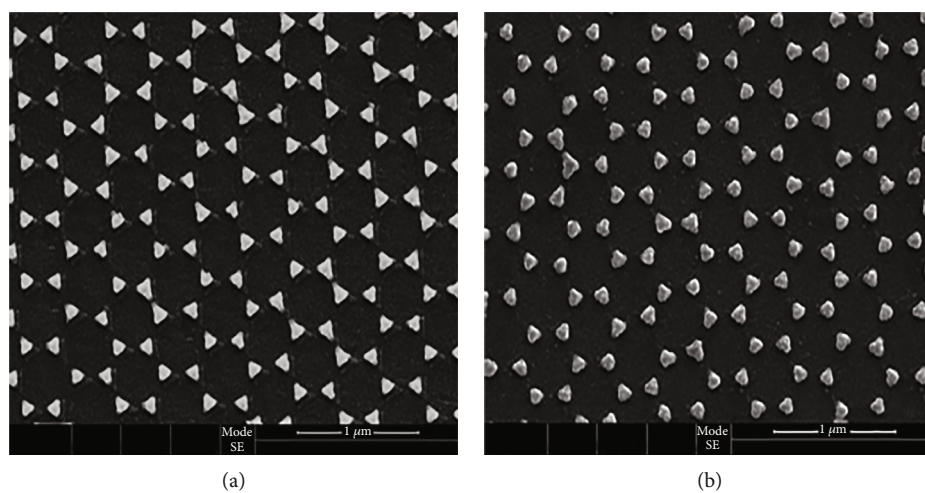


FIGURE 2: the silver nanoparticles characterization with SEM before and after modification. (a) characterization with SEM before modification. (b) characterization with SEM after modification (triangular silver nanosurfaces became obviously blunt with material binding).

respectively, using previous and new LSPR biosensors. Meanwhile, same clinical samples were confirmed using the CLIA (Chemiluminescence Immunoassay) method according to the manufacturer's instructions [14]. The detection results were collected and analyzed.

2.6. Statistical Analyses. Descriptive statistics were made by means with standard deviations and medians. Different study groups were compared using non-parametric tests. All p-values were two-sided, and the $P < 0.05$ was considered statistically significantly. Statistical analyses were performed using SPSS version 19.0 (IBM, Armonk, NY, USA).

3. Results and Discussion

3.1. Spectroscopy Observation of Each Process. The LSPR responses to the new functionalization process and detection of HE4 were shown such as Figure 3. It is well known that an increase in the local refractive index around nanoparticles could be induced by the molecular binding to the nanochip surface, and result in LSPR spectrum peak red-shift indicated as the $\Delta\lambda_{\max}$ [10, 12, 15, 16]. Thus, $\Delta\lambda_{\max}$ could be a reliable indicator of the analytes bound to nanoparticles. The LSPR wavelength (λ_{\max}) of bare silver nanochip before modification was 606.16 nm as measured in Figure 3(a). When MUA bound onto the nanochip, the LSPR λ_{\max} shifted to 619.12 nm (Figure 3(b)). After modification of 100ug/ml protein G onto the silver surface, the LSPR λ_{\max} shifted to 624.79 nm with a corresponding $\Delta\lambda_{\max}$ of +5.67 nm (Figure 3(c)). At last, an additional red-shift (+8.69 nm) of LSPR λ_{\max} was observed when immobilization of 10 $\mu\text{g}/\text{mL}$ anti-HE4 monoclonal antibodies onto the nanochip (Figure 3(d)). Importantly, the LSPR λ_{\max} shifted to +5.87 nm as showing a λ_{\max} of 639.35 nm (Figure 3(e)) when incubation in 1pM HE4, and indicated that new biosensor could successfully detect the target analyte on the nanoparticles-solution interface.

3.2. Detection of Different Concentrations of Standard HE4 with New LSPR Biosensor. The new biosensors were incubated with different concentrations of standard HE4 solution ranging from 0.1 pM to 100,000 pM under optimal conditions, and LSPR absorption spectra were measured with peak shifts recorded. Each concentration measurement was repeated three times, and mean $\Delta\lambda_{\max}$ were calculated, as shown in Table 1. It can be seen from the results that the LSPR $\Delta\lambda_{\max}$ value increased gradually with increasing HE4 concentrations, and indicated that the biosensor had a broader detection range. However, No significant changes or peak shift were observed in the spectra, when the concentration of standard HE4 solution was decreased to 1 pM or increased to 10,000 pM. Compared to previous sensor, this study showed that the new biosensor was more sensitive. The detection limit of HE4 only could accomplish 4 pM by using our previous LSPR biosensor [10]. This work was the first explore of LSPR biosensor by using Protein G directional fixed method to increase sensitivity, which could display a detection limit of 1 pM, with wide dynamic range of 1 pM to 10,000 pM. Due to the limited number of new chips, the

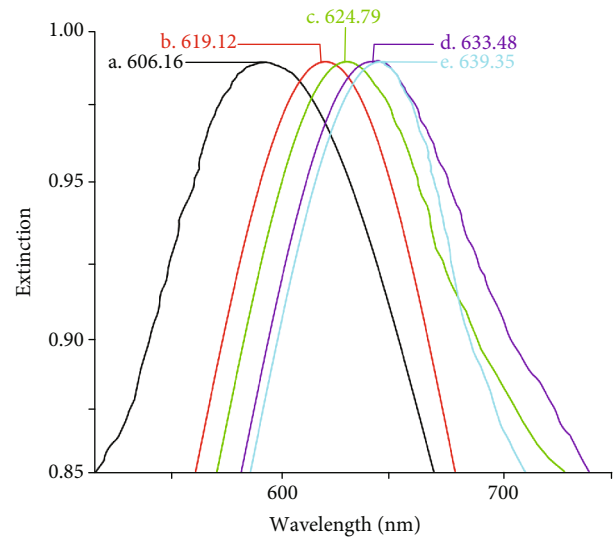


FIGURE 3: LSPR spectra for biosensor design and detection of 1 pM HE4. (a) Bare silver nanochip, $\lambda_{\max} = 606.16$ nm. (b) Modification of 1 mM MUA, $\lambda_{\max} = 619.12$ nm. (c) Incubation with 100ug/ml protein G, $\lambda_{\max} = 624.79$ nm. (d) Immobilization of 10 $\mu\text{g}/\text{mL}$ anti-HE4 monoclonal antibodies, $\lambda_{\max} = 633.48$ nm. (e) Detection of 1 pM HE4, $\lambda_{\max} = 639.35$ nm. Note: All spectra were collected at room temperature in air.

TABLE 1: Mean $\Delta\lambda_{\max}$ of different concentrations of standard HE4 detection with new LSPR biosensor (based on localized surface plasmon resonance and protein G directional fixed [10, 17]).

HE4 concentrations	0.1 pM	1 pM	10 pM	100 pM	1000 pM	10000 pM	100000 pM
Mean $\Delta\lambda_{\max}$	0.71	5.43	6.85	8.42	8.83	9.17	0.35

relation between HE4 concentrations and wavelength shift ($\Delta\lambda_{\max}$), limit of quantification, and inter/intraday variation would only be done in further study, which need more detections using a lot of new LSPR biosensors.

3.3. Selectivity Test with New LSPR Biosensor. To the biosensor, selectivity is very important and should acquire. In this study, control experiments were designed to ensure that the results were not interfered by nonspecific bindings. To achieve specific detection, PBS and ultrapure water were used as surface washing agents after sufficient immobilization of antibodies. As another tumor marker, squamous cell carcinoma (SCC) and albumin, one protein component often present in urine were implemented as interferences. During the experiment, 10 pM SCC or albumin was, respectively, incubated onto the functionalized biosensor for same time at room temperature, and all control experiments were executed in triplicate. Results indicated that there was hardly any shift about the LSPR peak after PBS rinsing. But, under the same condition, 10 pM HE4 was introduced and LSPR peak was found shift to +6.85 nm. Above experiment confirmed superior selectivity of the detection property based on the new biological-sensitive layer.

TABLE 2: $\Delta\lambda_{\max}$ of HE4 detection in urine of different study groups with previous LSPR biosensor (based on localized surface plasmon resonance [10]).

Study groups	LSPR wavelength shift ($\Delta\lambda_{\max}$)					$\bar{X} \pm SD$ (n=5, nm)
	Case 1	Case 2	Case 3	Case 4	Cases 5	
Healthy women	0.32	0.16	0.25	0.14	0.39	0.25 ± 0.11
Benign ovarian cyst patients	0.33	0.41	0.27	0.23	0.40	0.33 ± 0.08
Early ovarian cancer patients	0.42	0.12	0.58	0.29	0.33	0.35 ± 0.17

TABLE 3: $\Delta\lambda_{\max}$ of HE4 detection in urine of different study groups with new LSPR biosensor (based on localized surface plasmon resonance and protein G directional fixed [10, 17]).

Study groups	LSPR wavelength shift ($\Delta\lambda_{\max}$)					$\bar{X} \pm SD$ (n=5, nm)
	Case 1	Case 2	Case 3	Case 4	Cases 5	
Healthy women	0.49	0.05	0.85	0.43	0.06	0.38 ± 0.33
Benign ovarian cyst patients	0.91	0.38	0.50	0.12	0.63	0.51 ± 0.29
Early ovarian cancer patients	4.31	5.39	8.66	4.19	7.24	5.96 ± 1.94

TABLE 4: HE4 detection in urine of different study groups with CLIA method (based on Chemiluminescence Immunoassay method [14]).

Study groups	Testing HE4 in urine (concentration)					$\bar{X} \pm SD$ (n=5, pmol/L)
	Case 1	Case 2	Case 3	Case 4	Cases 5	
Healthy women	0.38	0.45	0.33	0.41	0.36	0.39 ± 0.05
Benign ovarian cyst patients	0.59	0.48	0.62	0.47	0.51	0.53 ± 0.07
Early ovarian cancer patients	2.01	2.79	1.96	2.82	2.33	2.38 ± 0.41

3.4. Urine Sample Detection with Previous and New LSPR Biosensor. Under optimal conditions, the clinical urine samples from healthy women, benign ovarian cyst patients, and early (I/II) ovarian cancer patients were, respectively, detected by previous and new LSPR biosensors. LSPR absorption spectra were accordingly measured with peak shifts recorded, with each sample measurement repeated three times. The results were shown as in Table 2 and Table 3. There were no significant LSPR spectra peak shift and difference among all study groups when using our previous LSPR biosensor. But, significant LSPR spectra peak red shifts were observed in early ovarian cancer patients by using new LSPR biosensor, without obvious LSPR $\Delta\lambda_{\max}$ found in healthy women or benign ovarian cyst patients. Based on statistical analyses, differences in response of HE4 detection between early ovarian cancer groups and the control groups (healthy women and benign ovarian cyst patients) were statistically significant by using new LSPR biosensor ($P < 0.05$). Meanwhile, in order to verify our experimental results, same clinical urine samples were also calculated using CLIA method, according to the manufacturer's instructions. The consistent results were confirmed as showed in Table 4. There were also significant differences in HE4 testing concentration between early ovarian cancer groups and the control groups (healthy women and benign ovarian cyst patients) by using CLIA. In this study, although the CLIA was also sensitive, it needed to be marked and the operation steps were tedious.

Thus it could be seen that the new LSPR biosensor was able to specifically distinguish between early ovarian cancer

and the negative controls without need for labeling and purification of the clinical samples, and just by the HE4 detection of women urine. Moreover, this new LSPR biosensor had good specificity that could not be interfered by other proteins or components in urine. Contrast to previous LSPR biosensor, this work firstly explored to enhance the detection sensitivity by using protein G directional fixed method. As a cell wall protein isolated from group G Streptococcus, protein G could combine directionally with Fc crystallizable segments of most mammalian immunoglobulin G and make the antibody antigen binding fragment pointing to the outer surface of nanostructure uniformly [17, 18]. Therefore, the antigen binding end of the immunoglobulin antibody could be more advantageous to the binding of target antigen and provided with high sensitivity detection for the LSPR biosensor.

The LSPR spectra of this new biosensor was measured during every processing and the results confirmed that the new fabrication procedures for biological-sensitive layer construction could be feasible and effective, as shown in Figures 1 and 3. After modification, the characterization with SEM also indicated triangular silver nanosurfaces became obviously blunt, owing to material binding on surface of nanoparticles, as shown in Figure 2. This improvement was very important for the LSPR biosensor to identify precisely low concentrations of biological substances in urine and could be potentially used in cancer screening and early diagnosis. Using this detection method, urine HE4 could be measured in real time within 40 minutes, without label or purification of sample, which was an important issue in wide clinical application for tumor screening.

4. Conclusion

To the best of our knowledge, this was the first use of LSPR method for detection of tumor marker in urine of cancer patients. As an important tumor marker of ovarian cancer, HE4 was reported that can be measured in urine, and perform similar sensitivity and specificity to that by assaying serum [9, 19–22]. Compared with traditional immunoassay approaches, our previous-built LSPR detection system had outstanding advantages, such as label-free, miniaturization, portability, rapid test time and low cost [10, 12, 13]. In this study, we firstly improved the sensitivity of LSPR biosensor by using protein G directional fixed method, and successfully used this new build biosensor to detect HE4 in urine. The new built biosensor in this study demonstrated that: 1) the self-assembled protein G onto silver nanochips via amino coupling could make anti-HE4 pointing to the outer surface uniformly, which improved the efficiency of antibody and sensitivity of detection system. 2) the new functionalized LSPR sensor was simple to prepare, could provide better sensitivity, had a lower detection limit, and had good selectivity for testing HE4 in urine, which could provide a non-invasive and more convenient approach in clinical ovarian cancer screening and early diagnosis. 3) the new-built LSPR system could be available for analysis of HE4 in human urine with advantages such as rapid test time, label-free, and purification-free process. Moreover, a HE4 urine calibration curve would be done in further study, which need a large, randomized, case-controlled clinical study to further evaluate applicability of this new biosensor in clinical tumor screening and medical diagnosis. In conclusion, the new biosensor was anticipated to be a promising platform for cancer biomarker detection in urine and expand clinical application of LSPR sensor.

Data Availability

Answer: Yes. Comment: The dataset supporting the conclusions of this article is included within the article.

Ethical Approval

This study was approved by the Institutional Review Board of West China Second University Hospital. Research Ethics Approval from Ethics Institutional Board and written informed consents from patients were not needed in this study.

Conflicts of Interest

The authors declare that they have no conflicts of interest.

Acknowledgments

This work was supported by the National Natural Science Fund of China (No. 61505126). We are grateful to the doctors and staff who have been involved in this work.

References

- [1] H. S. Salehi, P. D. Kumavor, H. Li et al., “Design of optimal light delivery system for co-registered transvaginal ultrasound and photoacoustic imaging of ovarian tissue,” *Photoacoustics*, vol. 3, no. 3, pp. 114–122, 2015.
- [2] C. Kreuzinger, M. Gamperl, A. Wolf et al., “Molecular characterization of 7 new established cell lines from high grade serous ovarian cancer,” *Cancer Letters*, vol. 362, no. 2, pp. 218–228, 2015.
- [3] L. Salman, G. Sabah, A. Jakobson-Setton, O. Raban, E. Yeoshoua, and R. Eitan, “Neutrophil-to-lymphocyte ratio as a prognostic factor in advanced stage ovarian carcinoma treated with neoadjuvant chemotherapy,” *International Journal of Gynecology & Obstetrics*, vol. 148, no. 1, pp. 102–106, 2020.
- [4] S. Capriglione, D. Luvero, F. Plotti et al., “Ovarian cancer recurrence and early detection: may HE4 play a key role in this open challenge? A systematic review of literature,” *Medical Oncology*, vol. 34, no. 9, article 164, 2017.
- [5] G. Scaletta, F. Plotti, D. Luvero et al., “The role of novel biomarker HE4 in the diagnosis, prognosis and follow-up of ovarian cancer: a systematic review,” *Expert Review of Anticancer Therapy*, vol. 17, no. 9, pp. 827–839, 2017.
- [6] K. H. Han, N. H. Park, J. J. Kim et al., “The power of the risk of ovarian malignancy algorithm considering menopausal status: a comparison with CA 125 and HE4,” *Journal of Gynecologic Oncology*, vol. 30, no. 6, article e83, 2019.
- [7] W. L. Yang, Z. Lu, J. Guo et al., “Human epididymis protein 4 antigen-autoantibody complexes complement cancer antigen 125 for detecting early-stage ovarian cancer,” *Cancer*, vol. 126, pp. 725–736, 2019.
- [8] K. Huhtinen, P. Suvitie, J. Hiisa et al., “Serum HE4 concentration differentiates malignant ovarian tumours from ovarian endometriotic cysts,” *British Journal of Cancer*, vol. 100, no. 8, pp. 1315–1319, 2009.
- [9] I. Hellstrom, P. J. Heagerty, E. M. Swisher et al., “Detection of the HE4 protein in urine as a biomarker for ovarian neoplasms,” *Cancer Letters*, vol. 296, no. 1, pp. 43–48, 2010.
- [10] J. L. Yuan, R. Q. Duan, H. Yang, X. G. Luo, and M. R. Xi, “Detection of serum human epididymis secretory protein 4 in patients with ovarian cancer using a label-free biosensor based on localized surface plasmon resonance,” *International Journal of Nanomedicine*, vol. 7, pp. 2921–2928, 2012.
- [11] H. Vaisocherova, V. M. Faca, A. D. Taylor, S. Hanash, and S. Y. Jiang, “Comparative study of SPR and ELISA methods based on analysis of CD166/ALCM levels in cancer and control human sera,” *Biosensors & Bioelectronics*, vol. 24, pp. 2143–2148, 2009.
- [12] Q. Y. Zhao, R. Q. Duan, J. L. Yuan, Y. Quan, H. Yang, and M. R. Xi, “A reusable localized surface plasmon resonance biosensor for quantitative detection of serum squamous cell carcinoma antigen in cervical cancer patients based on silver nanoparticles array,” *International Journal of Nanomedicine*, vol. 9, pp. 1097–1104, 2014.
- [13] T. Lai, Q. N. Hou, H. Yang, X. G. Luo, and M. R. Xi, “Clinical application of a novel silver nanoparticles biosensor based on localized surface plasmon resonance for detecting the microalbuminuria,” *Acta Biochimica et Biophysica Sinica*, vol. 42, no. 11, pp. 787–792, 2010.
- [14] X. L. Fu, Y. Y. Liu, R. Y. Qiu et al., “The fabrication of magnetic particle-based chemiluminescence immunoassay for human

- epididymis protein-4 detection in ovarian cancer,” *Biochemistry and Biophysics Reports*, vol. 13, pp. 73–77, 2018.
- [15] E. Petryayeva and U. J. Krull, “Localized surface plasmon resonance: nanostructures, bioassays and biosensing—a review,” *Analytica Chimica Acta*, vol. 706, no. 1, pp. 8–24, 2011.
- [16] R. Q. Duan, J. L. Yuan, H. Yang, X. G. Luo, and M. R. Xi, “Detection of p 53 gene mutation by using a novel biosensor based on localized surface plasmon resonance,” *Neoplasma*, vol. 59, no. 3, pp. 348–353, 2012.
- [17] H. H. Chiu, I. L. Tsai, Y. S. Lu, C. H. Lin, and C. H. Kuo, “Development of an LC-MS/MS method with protein G purification strategy for quantifying bevacizumab in human plasma,” *Analytical and Bioanalytical Chemistry*, vol. 409, no. 28, pp. 6583–6593, 2017.
- [18] A. Sinibaldi, C. Sampaoli, N. Danz et al., “Bloch surface waves biosensors for high sensitivity detection of soluble ERBB2 in a complex biological environment,” *Biosensors*, vol. 7, pp. 1–13, 2017.
- [19] C. A. Shah, K. A. Lowe, P. J. Paley et al., “Influence of ovarian cancer risk status on the diagnostic performance of the serum biomarkers mesothelin, HE4, and CA125,” *Cancer Epidemiology, Biomarkers & Prevention*, vol. 18, no. 5, pp. 1365–1372, 2009.
- [20] I. Hellstrom, J. Raycraft, M. Hayden-Ledbetter et al., “The HE4 (WFDC2) protein is a biomarker for ovarian carcinoma,” *Cancer Research*, vol. 63, pp. 3695–3700, 2003.
- [21] R. G. Moore, A. K. Brown, M. C. Miller et al., “The use of multiple novel tumor biomarkers for the detection of ovarian carcinoma in patients with a pelvic mass,” *Gynecologic oncology*, vol. 108, no. 2, pp. 402–408, 2008.
- [22] R. G. Moore, D. S. McMeekin, A. K. Brown et al., “A novel multiple marker bioassay utilizing HE4 and CA125 for the prediction of ovarian cancer in patients with a pelvic mass,” *Gynecologic Oncology*, vol. 112, no. 1, pp. 40–46, 2009.